UNIVERSIDADE DE SÃO PAULO
Instituto de Química de São Carlos

Synthesis of Bi- and Ln^{3+}-doped In- halide double perovskites ($A_2B'B''X_6$): from photocatalysis to optical thermometry applications

Luan do Nascimento Passini

Dissertation defense to obtain the Master's degree in Chemistry at São Carlos institute of chemistry, University of São Paulo – IQSC/USP

São Carlos

Janeiro, 2022

UNIVERSIDADE DE SÃO PAULO
Instituto de Química de São Carlos

Synthesis of Bi- and Ln^{3+}-doped In- halide double perovskite ($A_2B'B''X_6$): from photocatalysis to optical thermometry applications

Luan do Nascimento Passini

Advisor: Prof. Dr. Danilo Manzani

Dissertation defense to obtain the Master's degree in Chemistry at São Carlos institute of chemistry, University of São Paulo – IQSC/USP

São Carlos
April, 2022

Assinatura:
Data:

Ficha Catalográfica elaborada pela Seção de Referência e Atendimento ao Usuário do SBI/IQSC

Passini, Luan do Nascimento
Development of Bi- and Ln3+-doped In-halide double perovskite (A2B'B"X6): from photocatalysis to optical thermometry applications / Luan do Nascimento Passini. — São Carlos, 2022.
100 f.

Dissertação (Mestrado em Química Analítica e Inorgânica) — Instituto de Química de São Carlos / Universidade de São Paulo, 2022.
Edição revisada

Orientador: Prof. Dr. Danilo Manzani

1. Peovskitas. 2. Fotônica. 3. Fotocatálise. 4. Lantanídeos. 5. Termometria óptica. I. Título.

Sonia Alves - CRB: 4280/8

This work is dedicated to my parents Reginaldo and Marli, my relatives and close friends, for all the support, comprehension, motivation, entertainment and kindness through this period. All of them were responsible to keep my dreams alive.

Acknowledgements

The following acknowledgements are written in Portuguese, so my family and friends can read.

Agradeço primeiramente a minha família por todo o suporte e incentivo dado, principalmente aos meus pais Reginaldo e Marli, meu tio José Francisco, minha avó Dona Neguita e meu avô Lima. Toda confiança, carinho e apoio dado foi crucial para eu nunca desistir, e sempre continuar buscando realizar meus sonhos.

Ao meu orientador, Prof. Dr. Danilo Manzani, por ter me aceitado em seu grupo de pesquisa, por todos os ensinamentos impagáveis, pela paciência, carinho, incentivo, ajuda, conselhos profissionais e pessoais, e pelas risadas durante todo esse caminho. Com certeza ele foi uma pessoa essencial para eu continuar sonhando, um amigo para uma vida toda.

Aos Colegas do LaMIV, Danielzinho, Giovana, Naiza, Luigi, Thiago, Renatinho, Marina, Kenan, Victor, Joacilia, Bruno, Leandro, Vinicius, Giulia, Guilherme, José Hermeson, e Ana, por toda a ajuda, conhecimento compartilhado, e pelas risadas. Foi muito prazeroso dividir essa experiencia com cada um.

Aos amigos do NanoLum, Robertop, Chico, Elô, Euzane, João, Douglas, Leticia, Izabela, Larissa, Pedro, André e Tatiana, pelas risadas, companheirismo, cervejas, churrascos e principalmente, por todo ensinamento e paciência durante esses anos.

Aos meus amigos e agregados do "Fogo de Paia" de cravinhos, Bertone, Bruna, Ernani, Gustavo, Fracon, Vercezi, Matheus, Paulo, Iago, Favati, Guto, João, Marcel, Rafael e Rod, por sempre me incentivarem, confiarem no meu potencial, por toda as brincadeiras e zoeiras, por todas as cervejas e risadas, e por toda força em momentos difíceis.

Aos meus amigos André e Debora, por sempre dividirem e compartilharem os melhores momentos comigo, por todos os karaokês, smashzadas, risadas, conselhos e incentivos durante toda nossa amizade. Ambos são extremamente especiais para mim.

Ao meu amigo Gabriel (Jão), que mesmo distante a amizade nunca mudou, e o carinho, o respeito e a admiração continuam crescendo de forma mútua. Toda breja, risada, companheirismo e os conselhos de vida são impagáveis.

À minha amiga Isadora, cujo sempre me apoiou, me ouviu e incentivou por todo esse período. Uma ótima e verdadeira amiga para todos os momentos.

Aos meus amigos da USP-RP, Bruce, Smile, XV, Besta, Capivara, Cunhado, Stoppa, Toledim, Alho, Pacu, Kinha, Truta, Whey, Frozen, Vô, Xileno, Fabiano, Tranquilo, Favorável, Zequinha, Miguel, Fátima, Soneca, Harley, Dear, Loma, Carol e Ingrid, pela amizade construída desde 2016, por toda risada, apoio, cerveja, festas, estudos varando a noite e conselhos. Verdadeiros amigos para uma vida toda.

Ao Prof. Dr. José M. A. Caiut, por toda ajuda, conselhos e ideias durante todo o projeto. Um ex-orientador que se tornou um grande amigo, obrigado pelas cervejas, risadas e ensinamentos.

Ao Dr. Elias e Prof. Dr. Ubirajara, pelos ensinamentos e ajuda no desenvolvimento na área de fotocatálise.

A todos funcionários e técnicos do IQSC, principalmente ao Carlos e ao Marcelo, por toda a gentileza e contribuição para o projeto de pesquisa.

A todos os professores que contribuíram para a minha formação.

Ao programa de pós-graduação em Química do IQSC.

Ao CNPq pela bolsa concedida.

Here's to the ones who dream
Foolish as they may seem
Here's to the hearts that ache
Here's to the mess we make

She told me
"A bit of madness is key
To give us new colors to see
Who knows where it will lead us?
And that's why they need us"

So, bring on the rebels
The ripples from pebbles
The painters, and poets, and plays

And here's to the fools who dream
Crazy as they may seem
Here's to the hearts that break
Here's to the mess we make

La La Land

Abstract

The research developed in this project seeks to synthesize lead-free undoped, Bi- and Ln^{3+}-doped In-based halide double perovskites, in order to understand and investigate their optoelectronic properties searching for the development of new materials for the photonics field. Both these perovskites, Bi- and In-based, exhibit different optical properties being suitable for distinct applications. Bi-based perovskites show a very promising photocatalytic activity desirable for photocatalysis while In-based perovskites are more appropriate for photoluminescent purposes, such as light-emission-diodes (LEDs), optical thermometry and photovoltaics. Furthermore, this present work intends to incorporate lanthanide ions into In-based double perovskite matrix, scoping the enhancement of In-perovskite optical properties. Lanthanide ions are well-known for their unique spectroscopic properties being able to expand In-based perovskite applications. Ln^{3+} ions are capable of emitting photons in UV-Vis-IR range as well as participate in some energy conversion processes like upconversion, downshifting and downconversion mechanism, broadening and improving its application. To synthesize both perovskites, a wet chemical route was adopted, resulting in perovskite microcrystals. After the synthesis was completed, these obtained microcrystals were washed with isopropyl alcohol then centrifugated at 8000 rpm for 10 minutes, posteriorly they were dried in an oven at 110 ºC for 24h. Both lead-free double halide perovskites were analyzed using several characterization techniques in order to fully understand its structure, chemical and optical characteristics. Beyond that, was evaluated the photocatalysis performance and the photoluminescence properties of Bi- and In-based perovskite, respectively. For Bi-based perovskite, the influence of silver and halides (Cl and Br) on its photocatalysis was investigated leading to some interesting insights correlating these elements and perovskite photocatalytic performance. Besides, an investigation of undoped and Ln^{3+}-doped In-based perovskite showed new photoluminescent properties for the doped samples being able to expand even more their application. In that sense, this work had centralized efforts in photocatalysis and optical thermometry fields contributing with insights about its optoelectronic properties as well as extending its application.

Keywords: Perovskites; Bi- and In-based perovskites; photonics; photocatalysis; solid-state chemistry; lanthanides; optical thermometry.

Resumo

A pesquisa desenvolvida neste projeto, procura sintetizar haletos de perovskitas duplas sem chumbo, tanto a base de bismuto quanto de índio dopadas com íons lantanídeos, procurando entender e investigar suas propriedades optoeletrônicas, almejando o desenvolvimento de novos materiais para o campo da fotônica. Ambas as perovskitas, tanto a base de índio quanto de bismuto, apresentam propriedades óticas distintas sendo adequadas para diferentes aplicações. As perovskitas de bismuto possuem uma atividade fotocatalítica promissora sendo interessantes no campo da fotocatálise, enquanto as perovskitas de índio são mais apropriadas para fins fotoluminescentes, como para diodos emissores de luz (LEDs), termometria ótica e fotovoltaicos. Além do mais, neste trabalho foram incorporados íons lantanídeos na matriz das perovskitas de índio, visando o melhoramento das propriedades óticas da perovskita de In. Os íons lantanídeos são reconhecidos por suas propriedades espectroscópicas únicas, tornando possível expandir as aplicações das perovskitas de índio. Os íons Ln^{3+} são capazes de emitir fótons nas regiões do UV-Vis-IV, bem como participar de processos de transferência de energia como os mecanismos de conversão ascendente, conversão descendente e *downshifting*, ampliando a aplicação do material. Para sintetizar as perovskitas propostas, foi adotado uma síntese em um meio aquoso, gerando micro cristais das perovskitas. Após o término da síntese, os micro cristais obtidos foram então lavados com álcool isopropílico, centrifugado à 8000 rpm por 10 minutos e por fim, foram levados à uma estufa aquecida à 110 ºC por 24h. Ambas perovskitas duplas sem chumbo foram submetidas à várias técnicas de caracterização, almejando entender por completo sua estrutura, química e propriedades óticas. Além das caracterizações, foram avaliados sua atividade fotocatalítica e suas propriedades fotoluminescentes, para as perovskitas de bismuto e índio, respectivamente. Para a perovskita de bismuto, foram investigadas as influências dos haletos (Cl e Br) e da prata em sua fotocatálise, resultando em dados interessantes relacionando esses elementos e a atividade fotocatalítica da perovskita. Por fim, foram investigadas as propriedades óticas para as perovskitas de In não dopadas e as dopadas, e os resultados de luminescência mostraram a possibilidade de expandir ainda mais a aplicabilidade desse material. Nesse sentido, este trabalho está focando no campo da fotocatálise e da termometria ótica, contribuindo com os dados obtidos sobre suas propriedades optoeletrônicas bem como ampliando a aplicação desses materiais.

Palavras-chave: Perovskitas; perovskitas a base de bismuto e índio; fotônica; fotocatálise; química do estado sólido; lantanídeos; termometria ótica.

List of figures

List of tables

List of abbreviation and acronyms

CBM	Conduction band minimum
CV	Crystal violet
DC	Downconversion
DRS	Diffuse reflectance spectroscopy
DS	Downshifting
EDS	Energy dispersive X-ray spectroscopy
E_g	Energy gap
E_p	Phonon energy
ESA	Excited state absorption
ETU	Energy transfer upconversion
IC	Internal conversion
ISC	Intersystem crossing
FE	Free exciton
FIR	Fluorescence intensity ratio
FTIR	Fourier-transform infrared spectroscopy
GSA	Ground state absorption
LED	Light-emitting diodes
LFDP	Lead-free double perovskite
LHP	Lead halide perovskite
LIR	Luminescence intensity ratio
Ln	Lanthanide
MHP	Metal halide perovskite
MOF	Metal-organic framework
NC	Nanocrystal
NIR	Near infrared
NP	Nanoparticle
PA	Photon avalanche
PCE	Photovoltaic cell efficiency
PLQE	Photon luminescence quantum efficiency
PLQY	Photon luminescence quantum yield
PSC	Perovskite solar cell
PV	Photovoltaic

QD	Quantum dot
SEM	Scanning electron microscopy
S_n	Singlet state n
S_r	Relative thermal sensitivity
STE	Self-trapped exciton
T_n	Triplet state n
UP	Upconversion
UV	Ultraviolet
VBM	Valance band maximum
Vis	Visible
XRD	X-ray diffractometry
δT	Uncertainty in temperature
Δ	Thermometric parameter

Summary

Perovskites in photonics: State-of-the-art

Perovskites refers to a mineral generally composed by calcium, titanium and oxygen as calcium titanate, $CaTiO_3$. Nonetheless, the term perovskite also describes materials which presents ABX_3 stoichiometry as $CsPbX_3$ ($X = Cl^-$, Br^- or I^-).[1] In particular, lead-halide perovskites (LHPs) have attracted attention owing to their great optoelectronic properties such as high absorption coefficient, low exciton binding energy, tunable bandgap, high charge-carrier mobility, and low trap densities.[1–3] These properties make LHPs great materials for LEDs,[4,5] lasers,[6,7] photodetectors,[8,9] photocatalysts[10] and especially for photovoltaic (PV) applications.[11,12]

Despite the outstanding properties of LHPs for optoelectronic applications, Pb element present in its composition limits LHPs usage in optoelectronic devices. Pb-based perovskite displays of poor stability under ambient conditions, and high toxicity.[3,13] Lead-free double perovskite ($A_2B'B''X_6$), in special Cs_2AgBiX_6 ($X = Cl^-$ and Br^-) have attracted attention due to its high stability under ambient conditions, because they are environment friendly, and the capacity of absorbing light all over the visible range.[14] However, Bi-based perovskite exhibits an intrinsic indirect bandgap which is not suitable for LEDs, lasers and photovoltaics applications, but is an interesting characteristic for photocatalysis.[15,16] $Cs_2AgBiBr_6$ perovskite has shown a promising photocatalytic behavior, in hydrogen evolution[15] and photocatalytic reduction of CO_2,[17] for example.

Fortunately, replacing Bi^{3+} for In^{3+} it is possible to achieve direct bandgap[18] leading to a suitable perovskite for photoluminescent applications. There are some works which incorporates lanthanide ions into $Cs_2AgIn_xBi_{1-x}Cl_6$ lattice broadening its application.[19–21] As far as we known, there are no Ln^{3+}-doped In-based perovskite material scoping optical thermometry applications. The development of luminescent ratiometric thermometers is significantly important task since conventional thermometers do not satisfy every need.[22]

In this sense, the main motivation of this master's dissertation was to study and synthesize Bi-based perovskite for photocatalytic applications since this field is still incipient explored by using such type of material. Furthermore, the work aims to produce RE-doped In-based perovskite for optical thermometry applications, contributing with the development of a novel Ln^{3+}-based luminescent thermometer.

1. Lead-free Halide Double Perovskites

1.1. Perovskites: An introduction

Calcium titanium oxide mineral or just calcium titanate ($CaTiO_3$) was discovered by Gustav Rose in the Ural Mounts of Russia (1839) and named after Lev A. Perovski (1792-1856).[23,24] The name perovskite does not only describes calcium titanate mineral, although it describes all compounds that exhibit the same crystal structure as $CaTiO_3$ i.e., ABX_3 chemical formula.[24] Perovskite materials are abundant in nature and it is believed that $MgSiO_3$ composes the largest amount in the mantle of the earth than any other mineral.[25] In general, ABX_3 structures are composed by three sites, in which A and B are cations, being A-cations larger than B-cations, and X being an anion, where X is octahedrally coordinated to B, resulting in BX_6 octahedra.[1,26] The [BX_6] octahedra shapes in an extended 3D network by sharing its corners with A cations situated in its cavity.[1,26] The perovskite crystallographic structure is presented in Figure 1.

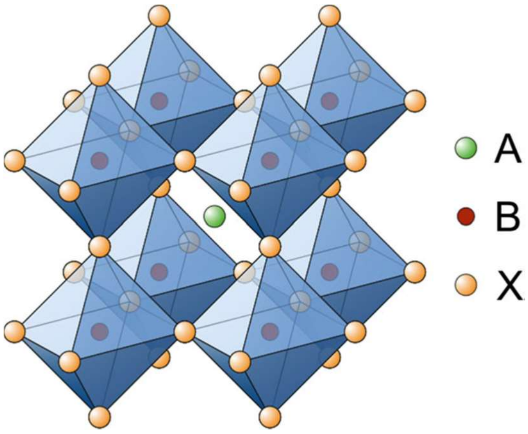

Figure 1. Representation of perovskite crystal structure.[27]

An ideal crystalline perovskite shows a cubic structure phase having Pm3m as its space group. Moreover, the ions in your network are considered to be perfectly packed and their ionic radii follow a geometrical ratio.[1,26] To predict the stability of perovskite structure is widely used two parameters proposed by GOLDSCHMIDT, 1926.[28] The tolerance factor (t) which indicates the state of distortion and the octahedral factor (μ), the ratio of atomic radii B to X for the BX_6 octahedron. These parameters are presented in equation (1) and equation (2), respectively.[29–31]

$t = \frac{r_A + r_X}{\sqrt{2}\,(r_B + r_X)}$; where r_A, r_B and r_X are ionic radii of A, B and X. **(1)**

$\mu = \frac{r_B}{r_X}$; where r_B and r_X are ionic radii of B and X. **(2)**

The range of t for perovskites materials is generally $0.81 < t < 1.11$, whereas the range of μ aiming a stable perovskite is usually $0.44 < \mu < 0.90$.[30]

These parameters show some predictions for perovskites stability according to their composition. However, its inefficient accuracy has been shown in recent studies[31] and a new tolerance factor have been proposed. The new tolerance factor proposed by BARTEL *et al.*, 2019 exhibits an overall better accuracy,[29] which is presented in equation (3). So, stable perovskites are found when $\tau < 4.18$.[29]

$\tau = \frac{r_X}{r_B} - n_A\left(n_A - \frac{\frac{r_A}{r_B}}{\ln\frac{r_A}{r_B}}\right)$; where n_A is the oxidation state of A, r_i indicates the ionic radius of ion i. **(3)**

Another essential parameter dictates the perovskite properties, the structural distortion. Distortions can affect perovskite properties such as ferroelectricity and play an essential role in structural transformation. Therefore, partial or full cation/anion replacement needs to be carefully planned in order to be a key tool to tune the physical properties, while undesired phase transformations are avoided.[1] Various perovskite compounds show some intriguing properties, ferroelectricity, magnetoresistance, and superconductivity are some of these properties.[1] Beyond that, a particular perovskite-type material is being broadly studied aiming at optical applications due to its incredible optoelectronic properties, the metal halide perovskites (MHPs). They present several characteristics very suitable for photovoltaics,[32,33] light-emitting diodes,[34,35] lasing,[6,34] photodetectors[36] and etc. that will be discussed on the next topics.

1.2. Metal halide perovskites

In general, perovskite presents ABX_3 structure, however, for MHP the A-site in MHPs is a monovalent cation, usually Cs^+, $CH_3NH_3^+$ or $CH(NH_2)_2^+$, in the B-site a divalent cation e.g.,

Pb^{2+}, Ni^{2+}, Cu^{2+}, Sn^{2+} etc. and halide as Cl^-, Br^- and I^- occupies the X-site.[1,37] MHPs are very promising materials in photonics owing to their outstanding intrinsic characteristics such as high absorption efficiency in the range of UV-Vis light, low exciton-binding energy, bright photoluminescence, and tunable bandgap by changing the elements present in A,B and/or X-site.[1,2,37] Despite the several options for the B-site, Pb^{2+} is the most chosen ion because of its better optoelectronic properties than any other possible metal.[1] Lead halide perovskites (LHPs) can be categorized as hybrid (organic-inorganic) or all-inorganic perovskite, just depending on if A is an organic molecule as methylammonium (MA, $CH_3NH_3^+$) or inorganic cation as Cs^+.[38] LHPs bright luminescence over the visible range are represented in Figure 2, noticed by Protesescu, L *et al.*[39] These luminescence tunability property will be discussed in detail on the next topic.

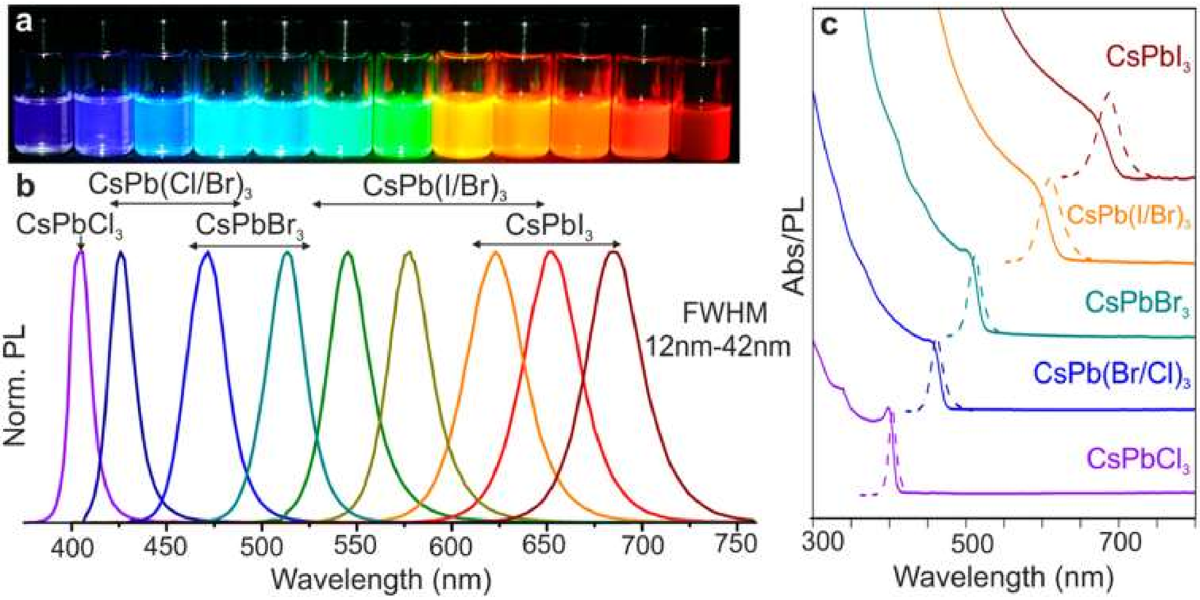

Figure 2. $CsPbX_3$ (X = Cl, Br or I) nanocrystals colloidal solution under UV light (a); representative photoluminescence spectra (b) and absorption and photoluminescence spectra.[39]

1.2.1. *Electronic structure of perovskite materials*

Luminescence property is established by the electronic structure of the material which is highly dependent on the chemical composition and crystal structure, including perovskite ones.[40]. For instance, in hybrid perovskites the inorganic layer dominates its luminescence property.[40] $[BX_6]$ octahedra have more influence in perovskite electronic structure than the monovalent cation A. In $MAPbI_3$ structures, p-electrons of lead are the electrons that mostly affect conduction band minimum (CBM) while the s orbital of Pb and p orbital of I compose the valence band maximum (VBM).[40] In Figure 2 is possible to observe the influence of B metal (Pb) and the halide X (x = Cl, Br and I) on the luminescent properties. As an example, $MAPbX_3$ and $CsPbX_3$ perovskites present the same electronic structure, furthermore, $MASnI_3$ and $FASnI_3$ exhibit a bandgap similar to the hypothetical $CsSnI_3$, considering the same particle dimension.[41] Nevertheless, A cations are able to tune the band structure by modifying the stretching and bending of Pb-X linkage in the octahedra.[41,42]

The perovskite luminescence properties becomes from the radiative processes, containing band-to-band transitions, transitions between sub-band levels, and electron-hole pair recombination.[40] The typical radiative transitions in semiconductor materials are illustrated in Figure 3.

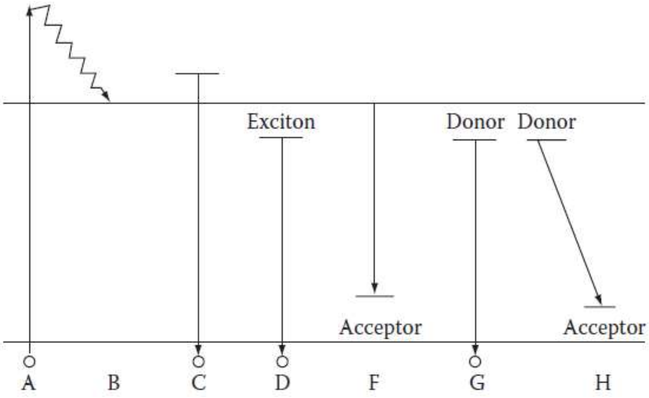

Figure 3. Radiative processes of a semiconductor solids.[43]

Processes A and B refer to a thermalization of an excited electron from the CB to the bottom of the CB (CBM). This thermalization occurs by a phonon emission, sometimes by nonradiative-assisted photon emission.[43] These photons can be reabsorbed leading other electron to CB if they display energy higher than the bandgap.[43] Process C is assigned to the electron-hole recombination generating the emission of a photon, it happens only in high purity single crystals.[43] Process D is the decay of a free exciton (FE) or the decay of a self-trapped exciton (STE). This process occurs in pure crystals at low temperature, and the decay of a free exciton can produce a sharp emission.[43] F and G processes are related to transitions between VBM and CBM with acceptors and donors. Transitions from the CB to a neutral acceptor (F) and neutral donor to the VB are represented by F and G, respectively.[43] In process H the donor and the acceptor are ionized due to the migration of an electron from the neutral donor to the neutral acceptor.[43]

Octahedral tilting distortion plays the main role in crystal structure, thus decreasing the size of the monovalent cation will lead to a decrease in the CBM width, providing distance increase between CBM and VBM, raising the bandgap energy.[44] In addition, despite chemical composition also being the cause of a structure distortion they will contribute as much as the crystal structure does. Changing the halide ratio in $CsPbX_3$ could allow the achievement of a broad luminescence spectrum from 400 to 700 nm,[39,40] as presented in Figure 2. Besides the crystal structure and composition factor, dimension is another important factor. As reported by D'INNOCENZO, Valerio et al., tuning the average size of $MAPbX_3$ as thin films from nanometers to micrometers, larger crystals exhibit a smaller bandgap and a longer lifetime.[45] It is possible to observe the quantum-size effects in perovskites absorption and emission spectra (Figure 4), as $CsPbBr_3$ crystallite size increases both absorption and emission band shifts for longer wavelengths.[39]

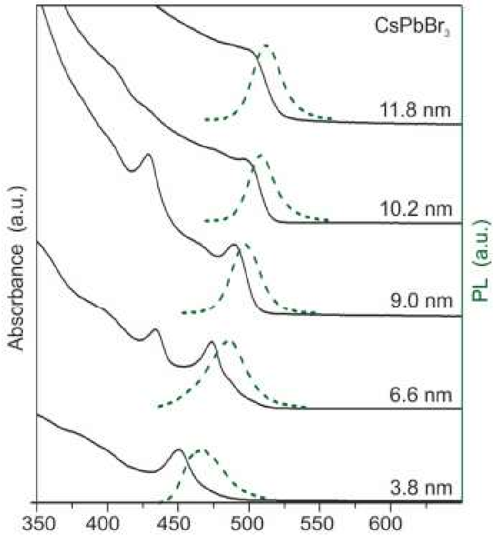

Figure 4. Absorption and PL spectra of different $CsPbBr_3$ perovskite size (4 – 12 nm).[39]

Luminescence in perovskite materials could be comprehended by studying the inductive effect and charge transfer. When one electron is excited from VBM to CBM upon the bandgap energy it could be understood as a charge transfer from the orbital which composes the valence band to that which composes the conduction band[40]. Charge transfer is often attributed to the transfer of charge from a ligand anion (halide or oxygen) into B cation (Pb^{2+}, Ti^{4+}) in the $[BX_6]$ octahedra. Thereby, the electron-hole pair produced by the absorption of a photon, induce an electron migration from VBM to CBM leaving a hole in the valence band. Thus, the charge transfer process can be analyzed considering the inductive effect.[46] For instance, in ABO_3-type perovskite the metal B needs a small amount of energy to transfer an electron from the ligand since the O-ligand is less attracted by the metal A. Taking $CsPbX_3$ as an example, by decreasing the electronegativity changing from Cl^- to I^- blue to red excitonic emission could be acquired.[40]

Defects and impurities also can generate luminescence. Despite those defects and impurities that might act as a quenching center for the light emission process, they also can act as a luminescent nucleus. They will provide the formation of a sub-bandgap state in the forbidden gap inducing radiative transitions.[40] Transition metals as Cr or Mn and lanthanide as Er, Nd, or Yb, are broadly used as luminescent centers. The luminescence from lanthanide ions can involve two types of transitions: intra-$4f^n$ transition well known as f-f transition and $4f^n$-$4f^{n-1}5d$ transitions or just f-d transition.[40] However, lanthanide luminescence properties and processes are discussed further, in the topic 3.3.

1.2.2. Main concerns of lead-based perovskites

There is a need of finding new elements that can replace Pb in the B-site of perovskite crystal owing to its degradation and toxicity, limiting its large-scale commercial application. Lead-based perovskites present a low concentration of lead which is soluble in water causing environmental hazards and are harmful to human health as potential carcinogens.[47–49] In the future, it might be the decommissioning of lead-based perovskites for electronic devices because of Pb element, some protective actions as European Union already restricted the use of toxic and heavy metals, more countries probably will adopt the same rules.[3,50] Beyond that, LHPs are unstable even under an inert atmosphere due to their intrinsic degradation.[51] In addition, even higher temperatures, moisture, and/or light accelerate perovskite decomposition.[40] For instance, $MAPbX_3$ compounds present some issues about structural phase transition at 55 ºC[52]. $FAPbI_3$ suffers structural instability at room temperature, crystallizing into a photoactive perovskite α-phase. well known as black phase or into photoinactive, non-perovskite hexagonal δ-phase also known as a yellow phase.[2] Moreover, $CsPbI_3$ also lacks structural stability crystallizing into orthorhombic δ-phase at room temperature, known as a yellow phase, which is photoinactive and perovskite black phase which is photoactive but only stable at a temperature above 300 ºC. [2] Under these circumstances, it is of utmost importance to look for different strategies and elements for the replacement of lead in metal halide perovskite formula to reach more stability under heat and moisture. Likewise, it is needed an environment-friendly option allowing its large-scale commercial manufacturing.

1.3. Lead-free perovskites

The replacement of lead for a non-toxic metal can be accomplished in general by two pathways, homovalent and heterovalent substitutions.[27] Homovalent substitution consists in replacing Pb for an isovalent cation such as elements from group14, transition metals, alkaline-earth, and lanthanide ions.[27] Heterovalent substitution use elements with different oxidation states (aliovalent) such as the elements Te, Sb, Bi, and Tl, transition metals, and lanthanides.[27] Heterovalent substitution does not result in ABX_3 structure owing to the impossibility to acquire charge neutrality. In order to obtain charge neutrality, mixing an identical portion of mono- and trivalent metal cations may give an utter divalent state, leading to a double perovskite structure ($A_2B^{+}B^{3+}X_6$) and the successful replacement of lead.[53,54] Figure 5 illustrate some candidates for Pb substitution.

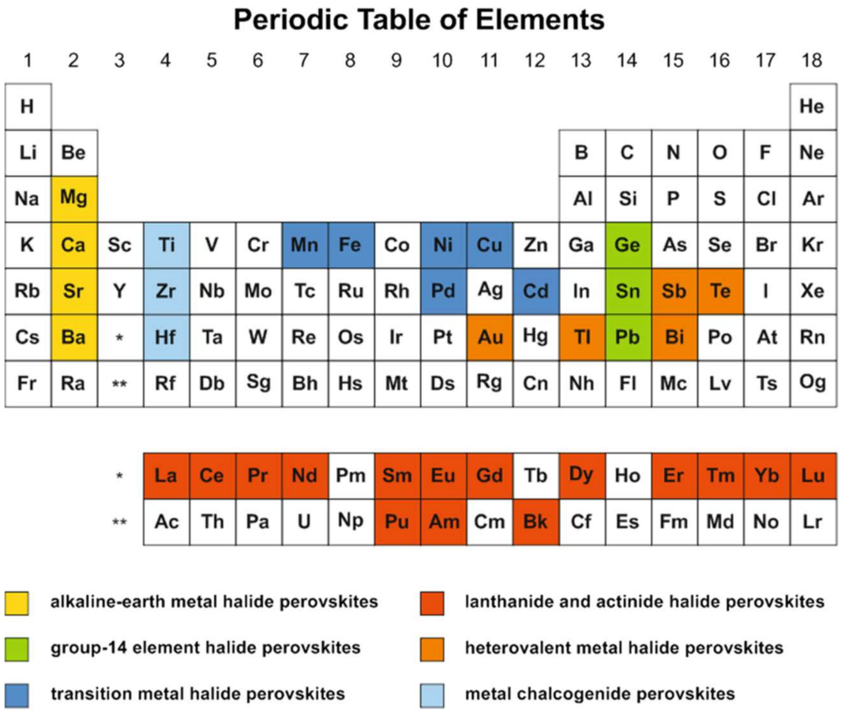

Figure 5. Periodic table containing the candidate cations for lead-free perovskite type compounds.[27]

The elements extensively used for Pb homovalent replacement are those belonging to the group 14, such as Sn^{2+} and Ge^{2+} cations, which show similar electronic configuration of Pb^{2+} ($6s^2\ 6p^0$).[50] Sn-based perovskite was the first explored candidate for LHPs replacement, because of both similar electronic configuration and similar ionic radii, avoiding lattice perturbation.[50] Sn-based perovskites usually present a $ASnX_3$ structure, exhibiting more narrow bandgaps and higher charge mobilities than Pb-based perovskites.[52] The 3D orthorhombic $CsSnI_3$ perovskite, presents a high optical absorption coefficient,[55] high charge-carrier mobility,[56] a favorable bandgap of 1.3 eV[56], and low exciton binding energy,[57] for instance. Although, Sn- and Ge-based perovskite presents an air sensitivity disadvantage compared to LHPs. Both Sn^{2+} and Ge^{2+} tend to oxidate into its higher oxidation states Sn^{4+} and Ge^{4+}, respectively, resulting in faster degradation of their perovskites.[27,50] Despite being other divalent possible candidates for lead replacement, theoretical calculations reported that divalent cations outside group-14 would negatively impact perovskite optoelectronic properties.[58]

1.3.1. Lead-free Double Halide Perovskites

A second possible pathway is to consider heterovalent substitution aiming to the development of lead-free perovskites. Heterovalent replacement will lead to the formation of a double perovskite structure with general chemical formula $A_2B^{'}B^{''}X_6$.[58] There are a plenty of double perovskite compositions and they are well-known for their ferromagnetic, ferroelectric, and multiferroic properties.[59] For halide double perovskites, A-site is commonly a monovalent cation as Cs^+, MA or FA; B' is a Cu^+, Ag^+ or Au^+; B" is a trivalent cation, usually Bi^{3+}, Sb^{3+} or In^{3+} and finally, X-site, halide elements as Cl^-, Br^- or I^-.[60] Bi-based double perovskites are promising candidates due to some similarities with Pb^{2+}. Bismuth trivalent ion is isoelectronic compared to Pb with $[Xe]6s^26p^0$ electronic configuration, they display almost the same electronegativity and Bi^{3+} has an ionic radius similar to Pb^{2+} and Sb^{2+} of 103 pm.[61–63] Cs_2AgBiX_6 materials exhibits an elpasolite structure, consisting of corner-sharing $B'X_6$ and $B''X_6$ octahedra alternatively along with the 3D network, presenting a highly symmetric *Fm3m* double perovskite structure as shown in Figure 6. Furthermore, they present incredible stability under ambient conditions (i.e.) stability under light, humidity and heat; and absorbs light all over the visible range.[64]

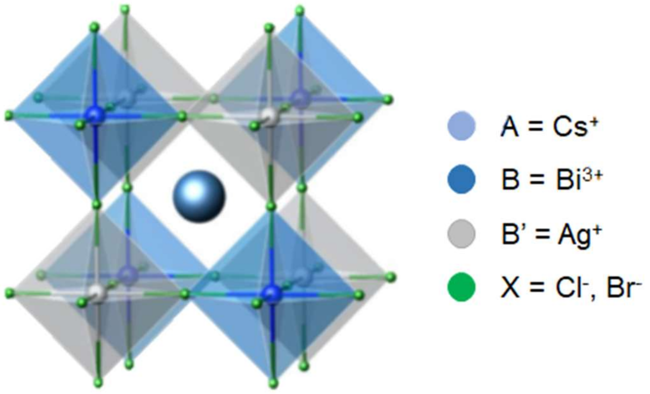

Figure 6. Lead-free halide double perovskite unit cell.[60]

Moreover, there are some works reporting the photocatalytic activity of Cs_2AgBiX_6 (X = Cl and Br) perovskite, turning these compounds interesting for photocatalysis applications.[16,17] Although, Bi-based perovskites present an indirect bandgap that limits their application for photovoltaics and light emission materials.[1,18]

The direct bandgap possesses a coincident wave-vector for the valence band maximum (VBM) and conduction band minimum (CBM), allowing a direct electronic transition by absorption/emission of photons.[65] There are cases in which the VBM and CBM do not present the same momentum, needing an electron-phonon interaction on the photoexcitation process.[65] This electron-phonon interaction will provide a transfer of momentum making the electronic transition possible, but with less energy compared with the direct bandgap transition due to this electron-phonon interaction.[65] The electronic transition process from CBM to VBM is illustrated in Figure 7 and the photon energy (hν) of both direct and indirect bandgaps are presented in the following equations: direct bandgap (4) and indirect bandgap (5).

$$h\nu = E_g \tag{4}$$

$$h\nu = E_g - E_p \tag{5}$$

Where h is the Planck's constant, ν is the frequency of the electromagnetic radiation, E_g is the gap energy and E_p is energy of the phonon.

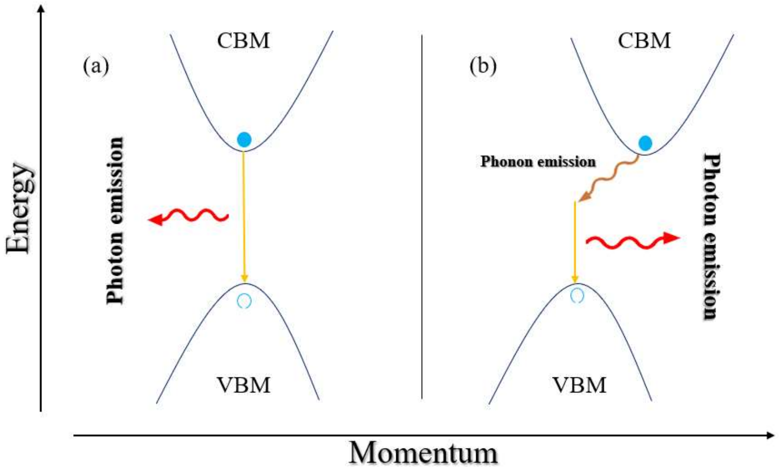

Figure 7. Illustration of light emission process for (a) direct, and (b) indirect bandgaps.

As shown in Figure 7, even with the same bandgap energy in the indirect bandgap semiconductor, it will involve the emission and/or absorption of a phonon. As a result, radiative recombination will have less probability to happen and when it occurs will present less photon energy than when direct bandgap is the case, with a reduced quantum yield.[65] For instance, YANG Bin *et al.*, showed $Cs_2AgIn_xBi_{1-x}Cl_6$ nanocrystals with indirect bandgap displaying photoluminescence quantum efficiency (PLQE) around 10%, and direct bandgap reaching 36.6%.[66]

The replacement of Bi^{3+} by In^{3+} in the perovskite lattice allow direct bandgap, being more suitable for photovoltaics and light emission applications.[18] $Cs_2AgInCl_6$ perovskites exhibit a cubic crystal structure with *Fm3m* space group and a direct bandgap between the visible and ultraviolet spectral range.[18,67] Despite the direct bandgap, In-based halide double perovskites exhibit a parity-forbidden transition, leading to a low photoluminescence quantum yield (PLQY) less than 0.1%.[67] The light emission of Cs_2AgInX_6 comes from self-trapped excitons (STEs) which arise from a strong Jahn-Teller distortion of $[AgCl_6]$ octahedron.[68] In order to enhance PLQY, it is necessary to break the parity-forbidden transition. A strategy is to partially replace Ag atoms by a suitable element that presents different electronic configuration, such as alkali metal. Partially replacing Ag by Na, it will manipulate the symmetry of STEs wavefunction, breaking the parity-forbidden transition improving the PLQY. [68] Luo J. *et al* reported $Cs_2Ag_{0.6}Na_{0.4}InCl_6$ doped with 0.04% of Bi and achieved a warm-white light emission with PLQY of 86% for over 1,000 h.[68] Moreover, stoichiometrically mixing Bi and In in perovskite will also break the parity-forbidden transitions. $Cs_2AgIn_xBi_{1-x}Cl_6$ (x = 0.75 to 0.9) will present allowed transitions improving the PLQY as shown by Yang and co-workers, reaching 36.6% using 90% of In and 10% of Bi.[66]

Therefore, this work aimed on the development of Bi- and Ln^{3+}-doped In-based perovskites materials for photocatalysis and optical thermometry applications, respectively.

2. Photocatalysis and perovskites

Textile dyes, insecticides, surfactants, pesticides, and heavy metals are hazardous compounds to the environment and with the development of new industries and the increase of population, these organic pollutants and heavy metals become a serious problem all over the world.[69,70] There are some conventional treatment methods to remove these compounds from water sources, although, highly toxic anthropogenic organic pollutants, especially those in very low concentration, demands novel techniques to be degraded.[70] This desired technique ideally should be inexpensive, green, and efficient to remove organic pollutants without generating toxic byproducts. Photocatalysis is one of the most promising solution against this environmental issue owing to its capacity to use naturally available and renewable solar energy to degrade organic pollutants, classifying the photocatalysis process as green and sustainable.[69,71] A lot of effort is being doing in photocatalysis, such as self-cleaning surfaces and water or air decontamination applications.[71] However, the scientific community is doing a lot of efforts to improve the photocatalysis capacity to satisfy the global demands by developing new techniques and advanced materials.[69]

Semiconductor photocatalysis, different from photo-Fenton process (homogeneous photocatalysis), is interesting due to its heterogeneous nature. It allows reusing the catalyst and due to the possibility of acting in a wide pH range, differently for the photo-Fenton process.[71] Heterogeneous photocatalysis reaction happens at the semiconductor surface and the process initiates when the photocatalyst is exposed to light.[71] The light source could be either from artificial source, as UV lamps, or solar light. When the photocatalyst material is illuminated with photons exhibiting equal or greater energy than their bandgap energy (E_g), it will excite electrons from VB to CB hence leaving a hole in the valence band.[69] These photoexcited electron-hole pairs can release their energy as heat if they recombine or they can move to the semiconductor surface. Once on the semiconductor surface, without any recombination they can induce redox reactions with the electrons (e^-) at the CB and the positive holes (h^+) in the VB.[72] A scheme of a common photocatalysis process is presented in

Figure 8, where A and D are the acceptor and donor species, respectively. The knowledge of the conduction band minimum energy and valence band maximum positions are very important since they define the reduction and oxidation ability caused by the photoexcited e^- and h^+.[73] Thereby, the photocatalysis reaction will occur when the redox potential of the substrate to be reduced is lower than the CBM, while the redox potential of the substrate to be oxidized is higher than de VBM.[73]

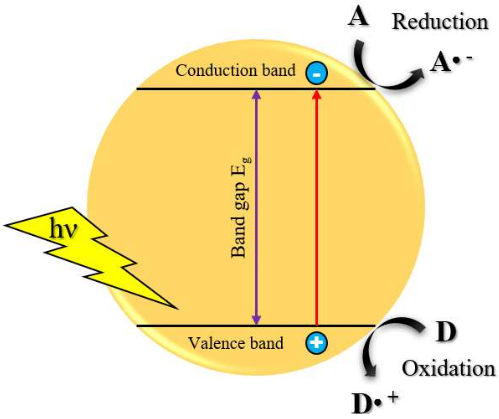

Figure 8. Scheme of a semiconductor photocatalysis process.

An ideal photocatalyst must show some characteristics as high carrier mobility, high surface area, correct bandgap edge position, suitable bandgap, and high visible light absorption.[69] There are numerous semiconductors photocatalysts that can be used in the organic pollutant degradation i.e. ZnO, CdS, MoS_2, WO_3, etc., but the most efficient one is TiO_2.[69] TiO_2 photocatalyst property was related approximately at 1920s and titania has been the most studied material for photocatalysis applications owing to its characteristics as chemically stable, environment-friendly, regeneration ability, cost-effectiveness and great photocatalytic efficiency.[69,71] TiO_2 presents three principal phases, anatase, brookite, and rutile, in which anatase phase is the most photocatalytic active phase because of its bandgap energy.[71] When TiO_2 are bombarded with photons (equal or greater than its bandgap energy) it will excite an electron to CB (e^-_{CB}) leaving a hole in VB (h^+_{VB}), as presented in equation 6. These electrons in the CB will react with O_2 producing superoxide radicals (O_2^-) or hydroperoxide radicals (HO_2). On the other hand, the positive hole in VB will oxidate the water, resulting on the generation of hydroxyl radicals (OH^-) and hydrogen ions (H^+).[71] All these radicals produced will react with the pollutants forming H_2O and CO_2 and, the production of $O_2^{\bullet-}$ and OH^- plus H^+ are presented in equations 7 and 8, respectively.[71]

$$TiO_2 + h\nu \rightarrow e^-_{CB} + h^+_{VB} \quad \textbf{(6)}$$

$$e^-_{CB} + O_2 \rightarrow O_2^{\bullet -} \quad \textbf{(7)}$$

$$h^+_{VB} + H_2O \rightarrow OH^{\bullet} + H^+ \quad \textbf{(8)}$$

However, even though TiO_2 being the most interesting material in photocatalysis application, there is still a problem: it only uses UV light from solar light due to its high energy bandgap (3.2 eV, anatase).[74] UV light composes only 4% of the solar spectrum, although visible light contributes nearly with 42% of the solar light,[75] being a much more interesting option using photocatalysts which utilize the visible light portion. There are a few possibilities to solve this problem, e.g. using another semiconductor as ZnO, which in certain experiments proved to be a better option than TiO_2.[69] WO_3 presents higher visible light absorption than TiO_2 and ZnO but, unfortunately, WO_3 exhibits a low potential reduction leading to a smaller light conversion compared to TiO_2.[69] The modification of bandgap structure and its surface area is required to enhance the semiconductor solar sensitivity and photolysis potential. Therefore, using dye sensitization, semiconductor coupling, quantum dot sensitization, semiconductor doping, plasmonic enhanced photocatalysis and etc.,[69] to provide these desired modifications is a good way to improve semiconductor photocatalytic potential. $Cs_2AgBiBr_6$ perovskite has shown a promising photocatalytic behavior, in hydrogen evolution[15] and photocatalytic reduction of CO_2,[17] for example. Wang T. *et al.,* synthesized $Cs_2AgBiBr_6$ perovskite mixed with reduced graphene oxide (RGO) displaying high stability for 120 h of continuous H_2 evolution under visible light.[15] Zhang Z. *et al*., showed a alcohol-based photocatalysis for metal deposited (Au and Pt) $Cs_2AgBiBr_6$ perovskite comparable with CdS photocatalytic activity.[16] Furthermore, photocatalytic reduction of CO_2 was recorded for $Cs_2AgBiBr_6$ NCs by Zhou L. *et al.*[17]

In this sense, this work aims to produce lead-free halide double perovskites and evaluate its photocatalyst properties, mainly on the study of the elements influence on their photocatalytic activity.

3. The light emission process and lanthanide ions

3.1. Luminescence

In 1888, the German physicist Eilhard Wiedemann defined luminescence as *all light phenomena that are not conditioned by a temperature increase only*, this definition provides good knowledge in relation to luminescence.[76] At the present time, IUPAC has determined that luminescence is *spontaneous emission of radiation from an electronically or vibrationally excited species not in thermal equilibrium with its environment*.[77] Luminescence process depends on the nature of excitation energy,[76] thus there are several types of luminescence. However, this project focuses on the photoluminescence processes. The emission of light originated from an excited electronic state by the radiative decay of an electron, is classified as photoluminescence.[78,79] In other words, following the IUPAC's definition[77], photoluminescence is *luminescence from direct photoexcitation of the emitting species*. Fluorescence, delayed fluorescence and phosphorescence are different processes of photoluminescence which will be detailed further in this topic.[79]

Luminescent materials have an essential role in humankind life and, this importance increased and are increasing over the years. Since the middle ages in Europe and around the tenth century in China and Japan, luminescent materials were known by humankind.[80] In 1603 was reported the first artificial phosphor. An Italian alchemist, Vincenzo Cascariolo, trying to produce gold utilized the natural mineral barite, $BaSO_4$. Beyond the obtention of gold by heating the mineral, he generated a persistent luminescent material, which emits a yellow to orange light.[81] This Bolognian stone had attracted even the interest of Galilei due to its intriguing property. Although was in 1671 that was revealed the origin of its luminescence. Kirchner showed that the impurity BaS is the reason for this light emission and not $BaSO_4$, by heating the barite among carbon black, intensifying its luminescence.[80] Back then, luminescent materials were just used for decoration purposes, although, the development of gas discharges and electron beams and the acknowledgment of X-rays, was a milestone at the end of 19th century.[80] A few years later, the cathode-rays tube, X-ray intensifying screens, and fluorescent lamps development had marked the first luminescent materials manufactured. Moreover, the extensive usage of X-rays for medical applications likewise the usage of fluorescent lamps for illumination purposes induced a greater effort in the exploration of novel luminescent devices in the half of the 20th century.[80] Since then, many great inventions have been achieved like the remarkable invention of white LED, which in 2014 could be built after the development of blue LED, an invention that awarded the physics Nobel prize to three Japanese researchers.[82] Combining blue LED with YAG:Ce^{3+} phosphor results in the creation of w-LED. Luminescent materials are essential for human being lives, thus understanding light emission processes are necessary needed scoping the fabrication of new luminescent products.

3.2. Jablonski diagram: Photoluminescence mechanisms

To understand the photoluminescence process, as fluorescence, delayed fluorescence, and phosphorescence which were previously mentioned, it is fundamentally important studying the well-known Jablonski diagram, presented in Figure 9. The Jablonski diagram describes the organic molecules photochemistry and may also use for inorganic compounds. This diagram is a graphical representation of the molecule electronic states along with the transitions that occur among these states.[83] The energy increases along the vertical axis, where the ground state or S_0 goes from the bottom to the excited states, singlet (S_n) or triplets (T_n), at the top of the graph. Between these states, it is possible to occur some characteristic transition, such as fluorescence, phosphorescence, internal conversion (IC), intersystem crossing (ISC), absorption, etc., which is represented by arrows. As a general rule, radiative transitions are pictured by straight arrows and non-radiative transitions by wavy ones.[83]

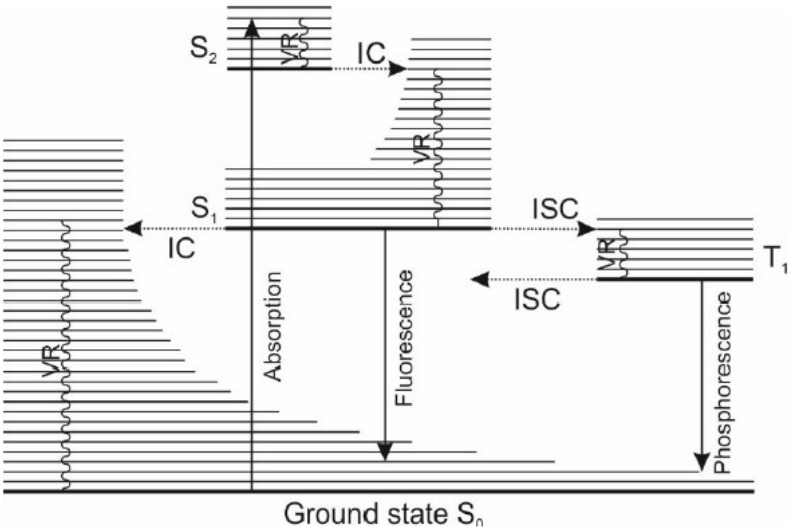

Figure 9. Generic Jablonski diagram along with the possible depiction transitions.[83]

Where VR means vibrational relaxation, IC means internal conversion and ISC implies an intersystem crossing. So, what is the difference between fluorescence and phosphorescence? The difference between those two emission processes is basically the spin multiplicity. In the case of fluorescence, the energy absorption leads the molecule into an excited electronic state without any spin change. When excited, the molecule suffers collisions with the neighboring molecules hence losing energy in a non-radiative manner until reaching the lowest vibrational level of the molecule excited electronic state. After that, the compound is able to experience a spontaneous emission by emitting the remaining energy as radiation.[84] Since the involved transitions do not need to change the spin multiplicity, like the transition $S_0 \leftarrow S_1$ presented in Figure 9, this process is denominated fluorescence. For the phosphorescence, the initial steps are the same, however, the presence of an excited state with different spin multiplicity, as singlets and triplets showed in the example in Figure 9, provides a different pathway. The molecule may do an intersystem crossing, a non-radiative transition involving electron spin change that converts ↑↓ to ↑↑ between different multiplicity states, going from a singlet state to a triplet, as an example.[84] Singlet-triplet transition, despite being forbidden could happen in the presence of spin-orbit coupling. After the ISC, the excited triplet state loses vibrational energy until its lowest level. The same spin-orbit coupling breaks the selection rule, making possible the radiative transition between $S_0 \leftarrow T_1$ (for example).[84] Because of the fact that phosphorescence must change the spin multiplicity to happen, this process generally possesses a higher lifetime than fluorescence. In other words, basically, fluorescence is a spin-allowed transition ($\Delta S = 0$) that displays low lifetimes ($<10^{-8}$ s). Meanwhile, phosphorescence exhibits spin-forbidden transitions ($\Delta S \neq 0$) showing a long lifetime ($>10^{-6}$ s), owing to the low probability of decay.[76]

3.3. Photoluminescence in phosphors: The case of perovskites

There are many different phosphors in literature commonly composed by a host material embedded with activator (dopant) ions.[85] Lanthanide ion and transition metals are usually chosen as activator ions, ZnS-type semiconductors and electron-hole centers are also activator candidates.[85] These impurities are responsible to provide an efficient fluorescence for many materials.[86] At low dopant content, these luminescent centers are considered to be isolated.[86]. The influence on phosphor's absorption and emission can be described utilizing a configurational coordinate diagram,[85] presented in Figure 10. This scheme is simplistic, the parabolic shape of the potential energy curves is not parabolic. This potential energy curve represents the function of a configuration coordinate. Beyond that, this model displays many characteristics from Jablonski diagram (Figure 9), being able to illustrate many physical phenoms even Stokes shift.[85] Therefore, horizontal lines represents energy potentials and vibrational energy levels, correspondingly, vertical lines describes absorption an emission transitions.[85]

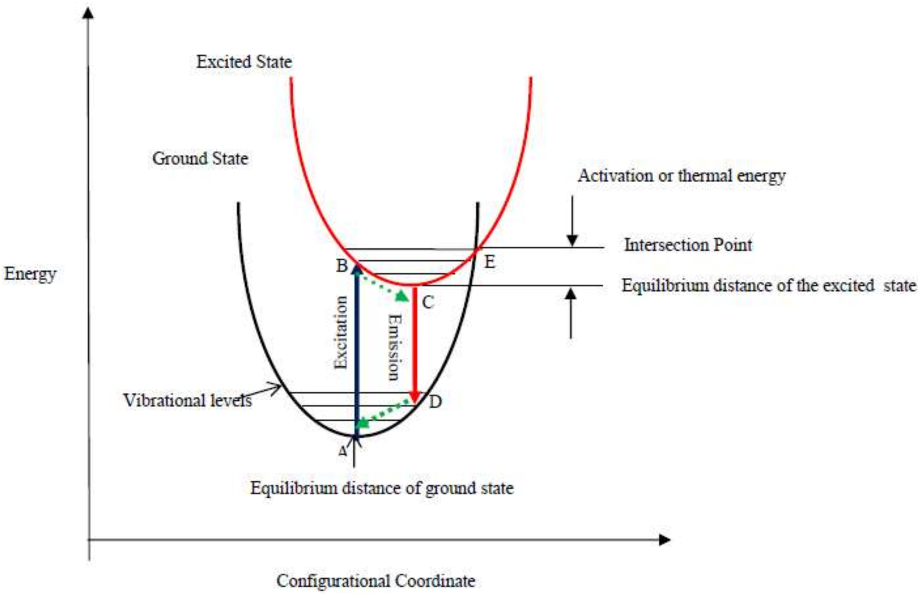

Figure 10. Scheme of coordinate diagram.[85]

The excited electrons from the ground state equilibrium (A) will populate an upper vibrational level of an excited state (B).[85] By emission of phonon, these excited electrons release its energy hence relaxing to the ground vibrational level of the excited state (C). Finally, they reach the highest vibrational level of the ground state (D) by a radiative emission, in sequence they return to their initial point (A) via phonon emission.[85] Electronic transition are much faster than vibrational relaxation, hence electronic transitions occur vertically.[85]

Luminescence is not a particular property of a certain compound, element, molecule, etc., this phenomenon can be present in different materials. In this work, beyond studying the intrinsic perovskite luminescence, studies about the photoluminescence of lanthanide ions using lead-free double halide perovskite as a host material were made and the optical thermometry application exploited.

3.3. Lanthanide ions

The term rare earth (RE) refers to a group of elements containing scandium (Sc), yttrium (Y), and the lanthanide ions (Ln). The lanthanide ions are exhibited at the sixth period of the periodic table and, display a total of 15 elements going from lanthanum (La) to lutetium (Lu).[87] The lanthanide ions and RE elements are illustrated in Figure 11. These RE elements, Ln ions accompanied by Sc and Y, exhibits a very similar chemical properties, as oxidation state 3+ in the most cases, and similar ionic radii, resulting in a simultaneous occurrence in nature with various RE elements in the same mineral.[87]

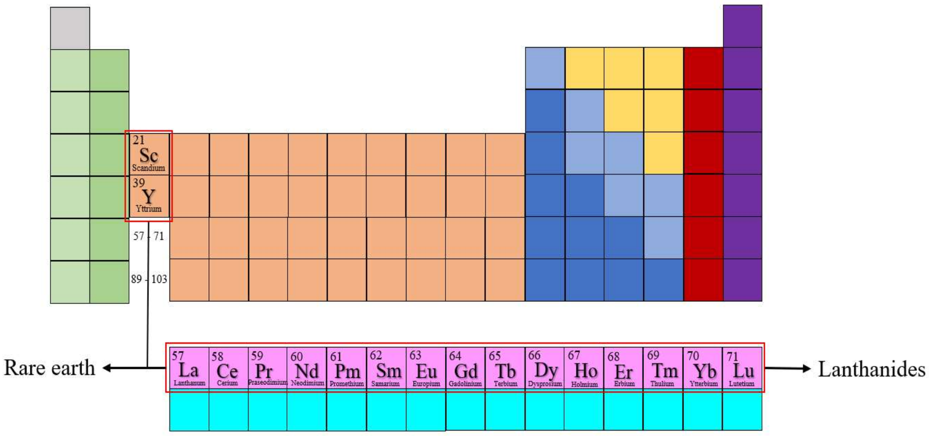

Figure 11. Periodic table highlighting lanthanide ion and rare earth elements.

Rare earth elements were first reported in 1751 when Axel F. Cronstedt discovered the mineral cerite, although, the beginning of RE's chemistry studies is attributed to the Swedish Carl Axel Arrhenius, which in 1787 discovered the mineral known as gadolinite. However, was in 1794 when the Finnish Johan Gadolin had separated the yttrium oxide from the gadolinite, recognizing yttrium as a new element and hence J. Gadolin was named after "Father of Rare Earths".[87] The separation of lanthanide ions from the mineral found in nature is not a simple task to do due to lanthanides high chemical similarity, in other words, they exhibit similar physical-chemistry properties among lanthanide ions and scandium and yttrium i.e. rare earth. Thus, their occurrence in nature usually happens in form of trivalent cations presenting very close ionic radii allowing a free replacement between them and consequently emerging mineral containing several rare earth elements in its composition.[87]

These resembling properties comes from their electronic distribution, in which for the neutral fundamental state they exhibit [Xe] $4f^n$, $6s^2$, $5d^x$ as their electronic distribution, with n increasing from 0 to 14 and, x = 1 for La, Ce, Gd, and Lu and x = 0 for the rest. The predominant trivalent state for the elements La, Ce, Gd and Lu which presents electronic configuration of [Xe] $4f^n$, $5d^{\mathbf{1}}$, $6s^2$ is clear and logically. Although, for the rest elements the trivalent state occurs by losing two electrons from $6s^2$ and one electron from 4f.[87] This preference for losing the 4f electron instead of losing a 5s or 5p is easy to understand looking at their radial distribution function, illustrated in Figure 12. Even though 5s and 5p being a more external shells, they possess a higher penetrability than 4f, turning the 4f electrons more available to contribute for the trivalent cation state.[87]

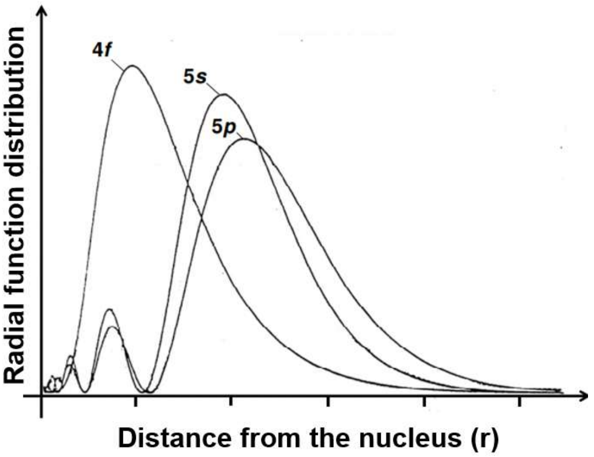

Figure 12. Representation of RE radial distribution function for the 4f, 5s and 5p orbitals of Nd^{3+} free ion.[88]

Another consequence of the radial distribution function and the electronic distribution is the well-known lanthanide contraction. Lanthanide contraction consists of a progressive decrease of the atomic and ionic radii with the increase of atomic number. The 4f orbitals exhibit less shielding capacity than any other orbital so, because of that, filling in the 4f orbitals, the external electrons (5s and 5p) will suffer a higher attraction due to the high effective nuclear charge leading to a contraction of the atomic/ionic radii, the lanthanide contraction. In addition, they are classified as hard acids by Pearson showing a preference to bond with hard bases, because of their elevated charge/radius ratio.[89]

This 4f internal position compared to 5s and 5p orbitals result into an external environment protection for 4f orbitals, thus 4f electrons are poorly affected by the ligand field. Therefore, the effects of ligand field over the lanthanide electronic properties are much less significant than in the case of transition metals (d orbitals), for instance. In light of this, lanthanide ions will present a narrow absorption and emission bands from f-f transitions with a really minor influence from the ligands.[87] Besides, they show electronic transitions with high lifetimes, about microseconds and milliseconds, owing to the forbidden aspect of f-f transitions.[89]

The $4f^n$ degeneracy can be broken with several disturbs at Ln^{3+} ion and can be described by three quantum numbers, total orbital angular momentum (L), total spin angular momentum (S) and total angular momentum (J).[76] The energy level for lanthanide free ions are described by a Hamiltonian (H_{FI}) and, this Hamiltonian is constituted by the interaction with the central field (H_0), interelectronic repulsion ($H_{e\text{-}e}$) and affected by spin-orbit interaction (H_{SO}).[90] First, free ions are affected by the central field, which separates the electronic configuration of each element in 10^5 cm^{-1} in energy. Besides, since H_0 possesses a spherical symmetry, the central field will not remove 4f configuration degeneracy.[76] On the other hand, the degeneracy of 4f configuration will be lost by the interelectronic repulsion. Higher energies are separated from lower energy levels by 10^4 cm^{-1}, in which low multiplicity $^{(2S+1)}L$ levels present lower energies and, all these levels will be disturbed by the spin-orbit interaction term.[76] H_{SO} removes the degeneracy of $^{(2S+1)}L$ levels in relation to 2S+1 components, resulting in a $^{(2S+1)}L_J$ levels, where they are separated by 10^3 cm^{-1} in energy. The equation describing the Hamiltonian free ion is presented in equation 9.[90]

$$H_{FI} = H_0 + H_{e\text{-}e} + H_{SO} \qquad \textbf{(9)}$$

The loss of symmetry from the spherical field (free ion) to a non-spherical crystal field (H_{CF}) will lead to a loss of degeneracy of $^{(2S+1)}L_J$ levels, leading to 2J + 1 Stark components, depending on the crystal field symmetry, and energetically separated by 10^2 cm^{-1}.[76] The total Hamiltonian is presented at equation 10,[90] and the effects of intra-atomic and crystal field interactions are schematized in Figure 13.

$$H = H_{FI} + H_{CF} \qquad \textbf{(10)}$$

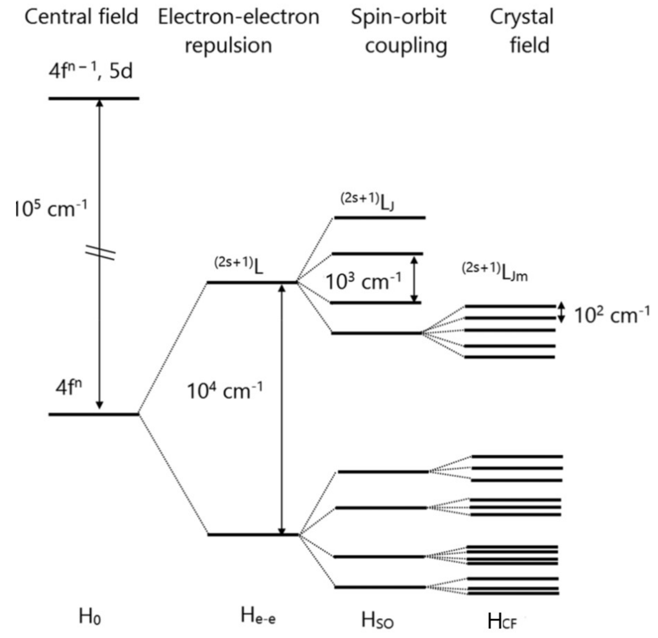

Figure 13. Scheme of intra-atomic and crystal field effects which leads into a loss of 4f configuration degeneracy.[76]

Since the nature of the crystal field exerts a weak effect on $^{(2S+1)}L_J$ energy levels, f-f transitions will slightly vary in relation to the crystal field in which they are inserted. Therefore, any trivalent lanthanide ion can be described in a universal scheme appropriate for any chemical environment.[76] This diagram is presented in Figure 14 and is well-known as Dieke diagram.

Lanthanum and lutecium elements are not presented in the Dieke diagram, in their electronic configuration either the orbital f is empty (La) or orbital f is full (Lu), hence not exhibiting any f-f transition.[76] Beyond the f-f intraconfigurational transitions, 4f^n ↔ 4f^{n}5d, and charge transfers transitions can be noticed.

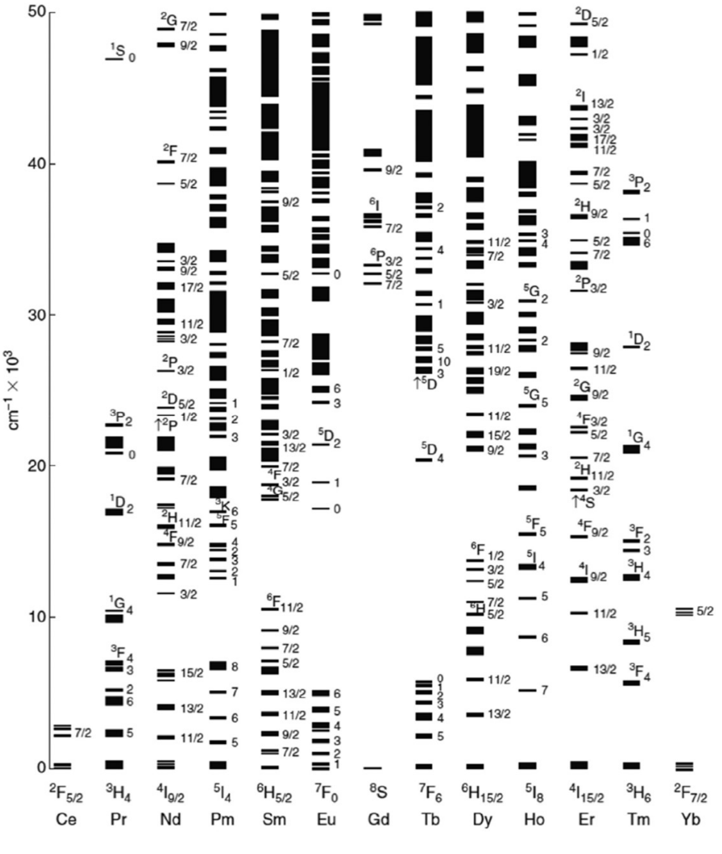

Figure 14. Diagram of the energy levels for trivalent lanthanide ions in LaCl$_3$ host with C$_{3v}$ symmetry .[91]

Thereby, this present work has aimed the researching and development of In/Bi-based perovskites doped with lanthanide ions, searching for some optimum Ln^{3+} doping that contributes and enhances perovskite photoluminescent properties. Beyond the characteristic emission of lanthanide ions, it is desired the visualization of energy transfer between the lanthanide ion and the perovskite, and energy transfer process such as upconversion. Through upconversion mechanism it was aimed the study and development of a lanthanide-based thermometer

3.3.1. Energy transfer in lanthanides: Upconversion

When absorption and emission of light do not occur in the same system, an energy transfer happens.[92] Usually, this energy transfer takes place when the active ions concentration is increased, and happens before any variation in radiative transition probability.[92] There are three energy transfer processes: downshifting (DS), downconversion (DC), and upconversion (UP). Downshifting or photoluminescence process, consists in the absorption of one photon followed by the emission of a lower energy photon. Generally, in this process, a higher energy photon is absorbed, resulting in a lower energy photon emitted.[93] An example of this process is the absorption of UV light followed by the emission at visible range. For Eu^{3+}, a UV photon is absorbed, and then a photon in the red region is emitted (~590 nm) by $^7F_1 \rightarrow {}^5D_0$ transition.[93] Downconversion, also known as *quantum cutting*, comprehended by the energy transfer of a high energy photon from an excited ion (sensitizer) to two adjacent ions (acceptors), both of them receiving half the energy of the absorbed photon and emitting 2 low energy photons.[93] The quantum efficiency of DC is above 100%, owing to the capacity of one photon turn into two lower energy photons.[94] Downconversion materials has been proven to be promising for the increase of solar cells efficiency since 2002,[95] and the most Ln^{3+} ions studied for this purpose are Pr^{3+}, Tb^{3+}, Er^{3+}, Yb^{3+}, Ce^{3+} and Eu^{2+}.[93] Finally, upconversion is a nonlinear process that consists in a sequential absorption of two or more photons resulting into a emission of one shorter wavelength photon.[92,93,96] UC was discovered and proposed in the mid-sixties by Auzel,[97] and Ovsyankin and Feofilov.[98] Since then, a great variety works studying theoretical and practically applications have been done. Several distinct UC mechanism are well-stablished, and they were summarized by Auzel.[92,99] Fundamentally, there are three distinct UC processes for lanthanide-doped materials: excited state absorption (ESA), energy transfer upconversion (ETU) and photon avalanche (PA).[93,96] Every pointed mechanism assume the successive absorption of two or more photons.[96]

In the first case, occurs a ground state absorption (GSA) followed by ESA in a single ion, this is the simplest UC process.[93,96] GSA step happens when the ion is excited from the ground state (G) to an intermediate excited state (E1). Once E1 state is populated, ESA step takes place promoting the electron to a higher excited state (E2), followed by emission by decay from E2 to G.[93,96] The commonly energy diagram to illustrate ESA mechanism is presented in Figure 15(a). APTE (*addition de photon par transferts d'energie*) or ETU, is considered to be the most efficient UC process.[93] In its GSA step, two neighboring ions are excited to their intermediate excited state (E1) by the consecutive absorption of two photons. One of the ions is promoted to the upper excited state (E2) by a non-radiative energy transfer process, while the other relaxes to the ground state (G).[93,96] The general energy diagram illustrating ETU process is exhibited in Figure 15(b). ESA and ETU are similar processes, both processes require a consecutive absorption of two photon to populate a higher energy level, although, ETU excitation occurs among two neighboring ions, in which one ion transfers energy to another one.[93,96] Energy transfer upconversion is strongly influenced by the dopant concentration, since it stablish the average distance between the two neighboring ions.[96]

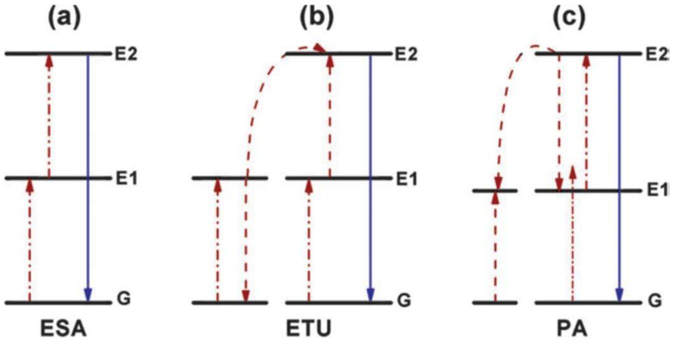

Figure 15. The three main upconversion (UC) processes for lanthanide materials. Excited state absorption (a), energy transfer upconversion (b), and photon avalanche (c). The full, dashed/dotted, and dashed arrow perform light emission, photon excitation and energy transfer.[96]

Photon avalanche (PA) presents an unusual pump mechanism, needing a pump amount higher than a specifically threshold value.[96] PA initiates with a non-resonant weak GSA populating the energy level E1. In sequence, the upper emitting state E2 is populated by a resonant ESA.[96] Posteriorly, ion pair relaxation (energy transfer) occurs among the ground state ion and the neighboring excited ion, leading to the occupation of E1 level by both. These two ions promptly occupies E2 level to induce cross-relaxation and exponentially increase of E2 level by ESA mechanism, resulting in a powerful UC emission.[96] Figure 15(c) shows the PA process scheme. The upconversion efficiency is considerably different between these processes. ESA exhibits the least efficiency UC, while ETU is the most efficient displaying approximately two orders of magnitude higher than ESA, 10^{-3} for ETU and 10^{-5} cm^2W^{-1} for ESA.[92,93,96] PA process can also present an efficient UC, yet it suffers from several drawbacks limiting its efficiency.[96]

Choosing the host, dopant/activators and sensitizers is a fundamental task. Ideally, the host presents low lattice phonon energies to minimize non-radiative losses and maximize the radiative emissions.[96] Generally, matrixes as heavy halides (chlorides, bromides and iodides) exhibits low phonon energies (< 300 cm^{-1}).[96] Lanthanide ions act as good activators, because of the shielding of 4f electrons, they also presents a weak electron-phonon coupling.[96] Not only, Ln^{3+} exhibits more than one excited 4f energy level, hence upconversion light emission can theoretically happen in almost every Ln^{3+}. Although, the energy difference between each excited state and its ground state should be adjacent to easily allow photon absorption and energy transfer of UC processes, resulting in a functional UC emission.[96] Er^{3+}, Tm^{3+} and Ho^{3+} are often used as activators. Low concentration of activator ions are desirable to avoid cross-relaxation, hence to prevent quenching of the excitation energy.[96] The sensitizer is used to enhance UC luminescence efficiency. Sensitizer with a large absorption cross-section, and a resonant excited state with several f-f transitions of other Ln^{3+} are essential. Yb^{3+} is well-known sensitizer for Er^{3+},[100] Pr^{3+},[101] Nd^{3+}[102] and Tm^{3+}.[103]

Upconverting materials can improve and enhance several existing materials for many applications, such as solar cells,[93] lasers,[104] photocatalysis,[105] bio-applications,[106,107] thermometry,[108–110] etc. In this present master's project, it will be focused upconversion process for optical thermometry application.

3.4. Luminescence thermometry: The case of Er^{3+}

Temperature, a thermodynamic state variant, measures the thermal energy of a certain body,[111,112] and its variation is crucial for innumerable natural and artificial processes[108] such as biomedicine and nanomedicine, climate, metrology, electronics, devices temperature management, food storage, etc.[85,86,113–118] It's vital the knowledge and measurement of a precise and accurate temperature. Time-response thermometers are limited by its size, thus measuring temperature at the microscopic scale is a tricky task for conventional thermometers.[108] The development of thermometers capable of real-time measurement at submicron scale is essential[110] for several applications, e.g. in photonics, micro/nano-electronics and nanomedicine.[110,119]

Thermometers can be categorized in respect to their physical interaction. The interaction between the thermometer and the target is sorted as contact (evasive), e.g., thermistors, and as noncontact (minimally evasive), e.g., pyrometers.[109] Semi-evasive thermometers presents physical interaction between the thermal probe and the measurand.[109] Not only, thermometric systems are sorted as primary and secondary. Primary thermometers measure the temperature by using well-established equations, in other words, utilizing thermodynamic laws and quantities without any calibration. Meanwhile, secondary thermometers needs a reference thermal probe and by comparison, hence requiring a calibration process, it is possible the temperature measurement.[109,110] Primary thermometers are more complex than secondary, however secondary thermometers requires regular calibration, especially when the medium in which this thermometer was calibrated changes.[109] Moreover, this uninteresting and time-consuming job cannot be accomplished in many cases. Thermometer's efficiency can be estimated by some parameters, as (relative) thermal sensitivity (S_r) which is the rate of the thermometric parameter (Δ) in response to temperature oscilation.[109] S_r can be expressed by equation 11.

$$S_r = \frac{1}{\Delta} \left| \frac{\partial \Delta}{\partial T} \right| \tag{11}$$

Uncertainty in temperature (δT), refers to the smallest temperature detectable by the thermometer, and it depends on both material and experimental setup.[109] Temperature uncertainty follows equation 12.

$$\delta T = \frac{1}{S_r} \frac{\partial \Delta}{\Delta} \tag{12}$$

Repeatability is the ability to generate the same result, under same conditions, repeatedly. Resolution evaluates temporal (∂t) and spatial (∂x) resolutions assigned as the minimal time interval and distance between measurements, respectively. Finally, reproducibility of the thermometer is the change of the same measurement executed under different situation.[109] There are some non-contact thermometry techniques being developed with high spatial resolution for micro- and nanometric scale, as Raman spectroscopy,[120] optical interferometry,[121] infrared thermography,[122] thermoreflectance[123] and luminescence.[22,124] In this work, it will be focused on lanthanides luminescent thermometry.

Luminescence thermometry is a noninvasive technique which exploits the thermal dependence of a luminescent material. Differences in excited states lifetimes, peak energy and intensity, and bandshape are observed for different temperatures making possible temperature measurement.[22,110,119] Temperature possible effects on luminescence are illustrated in Figure 16. This technique presents a remote high relative thermal sensitivity (>1% K^{-1}) and spatial resolution (<10 μm) in short acquisition times (<1 ms),[109,125] being suitable for applications as fast-moving objects, biological fluids, and strong electromagnetic fields.[22,119,126] The most used method to determine temperature by luminescence is the fluorescence intensity ratio (FIR) between two independent emission lines or bands (thermally coupled energy levels, Boltzmann statistics).[109,112] These emission lines can arise from a single-center thermometer, where there is a single luminescent center. When there are two different emitting centers, it is denominated dual-center thermometers.[109] Single-center thermometers of two thermally couples levels are naturally also primary thermometers.[100] Measuring temperature by analyzing the intensity ratio of two energy-close levels in thermal equilibrium is an interesting choice, since it can be explained by the Boltzmann thermal equilibrium between these states.[22] The less and the most energetic emission state is commonly represented as |1 > and |2 >, respectively. The population of |1 > and |2 > states are denoted as N_1 and N_2, and they can be associated by equation 14.

$$N_2 = N_1 \left({}^{g_2}/_{g_1} \right) exp \left({}^{-\Delta E}/_{k_B T} \right) \tag{14}$$

Where g_1 and g_2 represents the degeneracies of its respective level, ΔE being the energy difference among these states and k_B Boltzmann constant.[22] The intensity ratio (Δ), in other words, the thermometric parameter of 2 → 0 (I_2) and 1 → 0 (I_1) transitions is exhibited in equation 15.

$$\Delta = {}^{I_2}/_{I_1} = B\ exp \left({}^{-\Delta E}/_{k_B T} \right) \tag{15}$$

Unfortunately, these emission states cannot be too much separated from each other. To be considered as two thermally coupled levels, they must present an energy difference (ΔE) between the barycenters ranging from 200 to 2000 cm^{-1}.[22] Therefore, using equation 15 it is possible to dictate absolute temperature.

Ratiometric thermometers are very reliable temperature sensors, simple instrumentation is enough, and are not influenced by local intensity variation (e.g., emitting centers concentration and/or excitation source oscillation).[125] Every luminescent thermometer based on FIR of two thermally coupled energy level, do not need any calibration process to determine temperature.[100] However, working lower or higher than the range of Boltzmann equilibrium validity and sensitivity can imply in some erroneous temperature readout.[125]

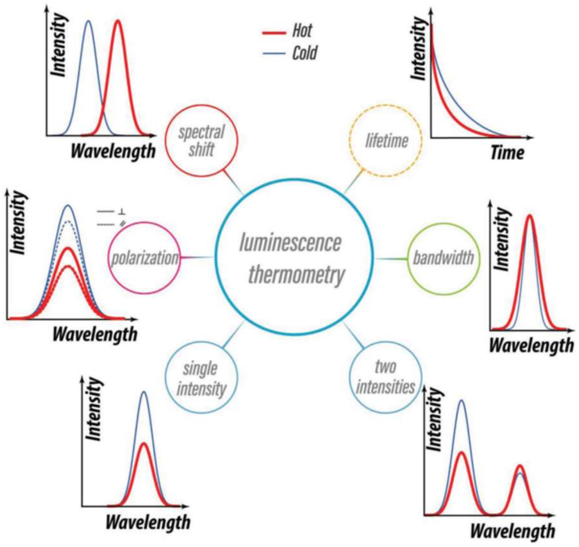

Figure 16. Scheme of possible effects in a phosphor's luminescence proportioned by temperature change.[109]

Among several different thermal probes, such as organic dyes,[127] proteins,[128] polymers,[129] Cr^{3+}-based materials,[130] and semiconductor quantum dots (QDs),[131] is the interest of this work to develop and study lanthanides-doped perovskites luminescent thermometry.[22] Ln^{3+} luminescent materials are versatile, stable and presents narrow emission bands (<10 nm) covering UV-Vis-NIR spectrum, with quantum yields superior than 50% in the visible range.[109,125] Not only, owing to the capacity of excitation and emitting radiation on the biological window (absorption and scattering of light in biological tissues is reduced),[109,119] their usage on in vivo thermal images,[132] and early tumor detection[133,134] are increasing. Various Ln^{3+}-based materials as metal organic frameworks (MOFs),[135] organic-inorganic hybrids,[136] chelate complexes,[137] polymers,[138] downshifting,[139] downconverting[140] and upconverting[141] nanoparticles, showed to cover an extensive temperature range from cryogenic (<100 K) to physiological (298 – 323 K). Some Ln^{3+} ions utilized for luminescent thermometry purpose are Pr^{3+},[142] Nd^{3+},[143] Eu^{3+},[144] Ho^{3+},[145] Tm^{3+},[146] and Er^{3+},[100,147,148] which this last one is the scope of this present work.

Upconversion systems are commonly made of a sensitizer, as Yb^{3+}, which will transfer energy to an activator ion, as Er^{3+}. Yb^{3+} is a great sensitizer due to its large absorption cross-section at NIR at 980 nm. Besides, trivalent ytterbium ions exhibits a resonant excited state energy level with Er^{3+}, Ho^{3+} and Tm^{3+} excited states, resulting in an efficient energy transfer.[109] Er^{3+} is one of the most utilized activators owing to its green emission assigned to $^2H_{11/2} \rightarrow {}^4I_{15/2}$ (around 520 nm) and $^4S_{3/2} \rightarrow {}^4I_{15/2}$ (around 540 nm) transitions, two thermally coupled energy levels.[109] Yb^{3+} and Er^{3+} are a well know lanthanide ion couple because of their upconversion, energy transfer process interesting for application such as in vivo imaging,[149] solar cells,[150] etc. Yb^{3+} and Er^{3+} upconversion process is illustrated in Figure 17. Suta *et. al.,* suggested that Er^{3+} single-center luminescent Boltzmann thermometer is one of the best thermometer in room temperature range.[112]

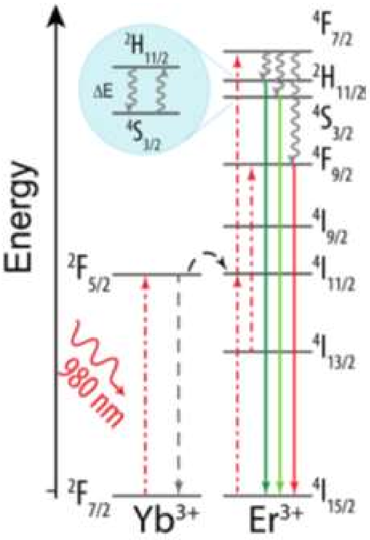

Figure 17. Schematic of Yb^{3+}/Er^{3+} energy transfer upconversion (ETU) mechanism with excitation at 980 nm, highlighting the ΔE between the two thermally coupled levels.

Considering this, the present work intends to synthesize Ln^{3+}-doped (Ln = Yb^{3+} and Er^{3+}) In-based perovskite to study the upconversion process as well as its spectroscopic properties to be applied as luminescent thermometer.

4. Objectives

This Master's project aimed to the development of Bi- and Ln3+-doped In-based lead-free double halide perovskites for applications in photocatalysis and photoluminescence thermometry. In the photocatalysis field, the studies were focused on the evaluation of the perovskite's compositions regarding their photocatalytic activity. For photoluminescence, the objectives were to doping Bi/In-based perovskite with lanthanide ions (Yb^{3+} and Er^{3+}) seeking for the enhancement of its optoelectronic properties aiming to explore optical thermometry application.

- Synthesis of Cs_2AgBiX_6 (X = Cl and Br) and $Cs_2Ag_xNa_{1-x}BiCl_6$ (x = 0.0; 0.2; 0.4; 0.5; 0.6; 0.8 and 1.0) via wet chemical route.
- Synthesis of $Cs_2AgIn_xBi_{1-x}Cl_6$ and $Cs_2AgIn_xBi_{1-x}Cl_6$: Ln^{3+} via wet chemical route.
- Structural, morphological, and optical characterization.
- Photocatalysis experiment for Bi-based perovskite samples.
- Spectroscopic studies of undoped and Ln^{3+}-doped Bi/In-based perovskites.
- Development of Ln^{3+}-doped In-based perovskites luminescent thermometers.

5. Experimental part: Materials and methods

5.1. Materials

The reagents were commercially purchased and used without pretreatment. HCl (Aldrich, 37%), HBr (Aldrich, 47%), CsCl (Vetec, P.A.), CsBr (Aldrich, 99.999%), AgCl (Aldrich, 99%) AgBr (Aldrich, 99%), $BiCl_3$ (Aldrich, ≥ 98%), $BiBr_3$ (Aldrich, ≥ 98%), NaCl (Synth, P.A.-A.C.S.), In_2O_3 (Merck, 99%), Nd_2O_3 (Lumitech, 99.99%), Er_2O_3 (Aldrich, 99.9%), Yb_2O_3 (Lumitech, 99.99%), isopropyl alcohol (Exodo, 99.5%).

5.1.1. Lead-free halide double perovskite synthesis

Perovskite samples were synthesized through aqueous solution method, as represented in Figure 18. $Cs_2AgBiCl_6$ (labelled as Ag1.0) was synthesized by adding stoichiometric amounts of AgCl (172 mg, 10 mM) and $BiCl_3$ (378 mg, 10 mM) (1:1 in mol:mol) in 120 mL of acid solution containing 100 mL of HCl (37 %) and 20 mL of H_2O (miliQ, 18.2 MΩ.cm), under vigorous stirring at 80 ºC for 15 min (solution 1). Afterward, stoichiometrically CsCl (404.1 mg, 20 mM) was added into solution 1 followed by rising the temperature to 110 °C under stirring for next 75 min. A yellowish solid was obtained, washed with isopropyl alcohol, centrifugated, and dried at 110 °C overnight. This synthesis procedure was taken and adapted from the work of Kumar Chini 2020 *et al.*[151] All samples were synthesized following the same method. The obtained perovskites are reported in Table 1.

.

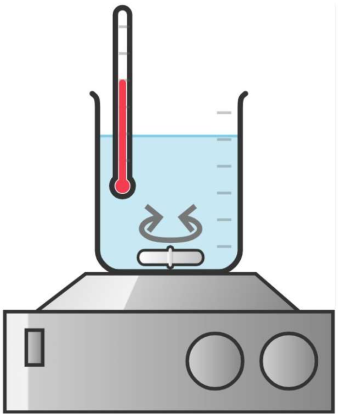

Figure 18. Schematic of the lead-free halide double perovskite experimental setup.

For chlorine Bi-based perovskite, the reagents with Ag and Na mixing were synthesized by stoichiometrically replacing Ag by Na according to $Cs_2Ag_xNa_{1-x}BiCl_6$ molar composition, in which x = 1.0; 0.8; 0.6; 0.5; 0.4; 0.2 and 0.0. In-based perovskite was synthesized following the same route but replacing $BiCl_3$ (10 mM) by In_2O_3 (5 mM, since In_2O_3 presents 2 mol of In^{3+}). For Bi/In-based perovskites, $BiCl_3$ (37.8 mg, 1 mM) and In_2O_3 (149.93 mg, 9 mM) were stoichiometrically mixed in order to achieve the desired composition for $Cs_2AgIn_xBi_{1-x}Cl_6$ perovskites.

Table 1. Perovskite compositions (Bi- and In-based) and their labels.

Bi-based perovskites		**In-based perovskites**	
Samples	**Label**	**Samples**	**Label**
$Cs_2AgBiCl_6$	pAg1.0	$Cs_2AgInCl_6$	pIn
$Cs_2Ag_{0.8}Na_{0.2}BiCl_6$	pAg0.8	$Cs_2AgIn_{0.9}Bi_{0.1}Cl_6$	pIn0.9
$Cs_2Ag_{0.6}Na_{0.4}BiCl_6$	pAg0.6	$Cs_2Ag_{0.6}Na_{0.4}InCl_6$	pAg0.6In
$Cs_2Ag_{0.5}Na_{0.5}BiCl_6$	pAg0.5	$Cs_2Ag_{0.6}Na_{0.4}In_{0.9}Bi_{0.1}Cl_6$	pAg0.6In0.9
$Cs_2Ag_{0.4}Na_{0.6}BiCl_6$	pAg0.4		

$Cs_2Ag_{0.2}Na_{0.8}BiCl_6$	pAg0.2	
$Cs_2NaBiCl_6$	pAg0.0	

Ln^{3+}-doped In-based perovskites were synthesized as listed in

Samples pIn0.9; pAg0.6In and pAg0.6In0.9 were doped with Er^{3+} and Yb^{3+} according to Table 2. The lanthanide ions were incorporated in perovskite host as chlorine precursor. Because of the same valence among Ln^{3+} and Bi^{3+} and In^{3+}, lanthanide ions tend to occupy Bi^{3+} or In^{3+} site to form [$LnCl_6$] octahedron. The incorporation of Yb^{3+} and Er^{3+} in In-based perovskite lattice is possible due to the similar ionic radii of Bi^{3+} (1.03 Å)[62] and In^{3+} (0.8 Å)[62] compared toYb^{3+} (0.87 Å)[62] and Er^{3+} (0.89 Å).[62] Owing to the higher proximity of In ionic radii in comparison with both Ln ionic radii, and because of its higher concentration in comparison with Bi^{3+} it is assumed that Ln^{3+} incorporation occurs replacing In^{3+}. Some previous work in literature already reported the successful synthesis of Ln^{3+}-doped In-based perovskites.[20,152,153]

Table 2. Composition and sample labels of Ln^{3+}-doped In-based perovskites.

Label	**Er^{3+} (mol %)**	**Yb^{3+} (mol%)**
pIn0.9:Er5	5	
pIn0.9:Er15	15	
pIn0.9:Yb-Er	(1, 2 and 5)	10
pAg0.6In:Er5	5	
pAg0.6In:Er15	15	
pAg0.6In:Yb-Er	(1; 2 and 5)	10
pAg0.6In0.9:Er5	5	
pAg0.6In0.9:Er15	15	
pAg0.6In0.9:Yb-Er	(1; 2 and 5)	10

5.1.2. Photocatalysis experiment

The perovskite photocatalytic activity was evaluated based on photodegradation of crystal violet (CV) dye in a solution of 70 mL containing 35 mg of the perovskite powder and 10 ppm of CV. First, 35 mg of pAg1.0 sample was dispersed in 35 mL of H_2O (miliQ) and sonicated for 30 min. Then, 35 mL of 20 ppm CV solution was added to the previous one.

The final 70 mL solution with a perovskite concentration of 0.5 g.L^{-1} and 10 ppm of CV, was stirred for 1 h in absence of light to reach the adsorption/desorption equilibrium. This step prevents any adsorption of the organic dye on the perovskite surface during the photocatalysis experiment, improving accuracy in the photodegradation experiment. After stabilization, aliquots of 2 mL were taken out from the solution at intervals of 5 or 10 min, centrifugated to remove precipitate particles and UV-Vis spectrum was recorded in order evaluate the photodegradation mechanism by monitoring the CV absorption at visible range. The organic dye is a model of an organic pollutant, and the photodegradation of it is a typical experiment to measure the photocatalytic activity of a given material. Photocatalysis setup is shown in Figure 19. Basically, of the perovskite/CV system was irradiated with a UV-Visible Xe arc lamp (300 – 600 nm) light. The perovskite/CV solution reactor was located 7 cm away from the Xe lamp, and it was made of borosilicate glass to avoid CV degradation resulted from glass-CV interaction. The samples whose photocatalytic activity was evaluated are pAg1.0, pAg0.8, pAg0.6, pAg0.5, pAg0.4, pAg0.2 and pAg0.0.

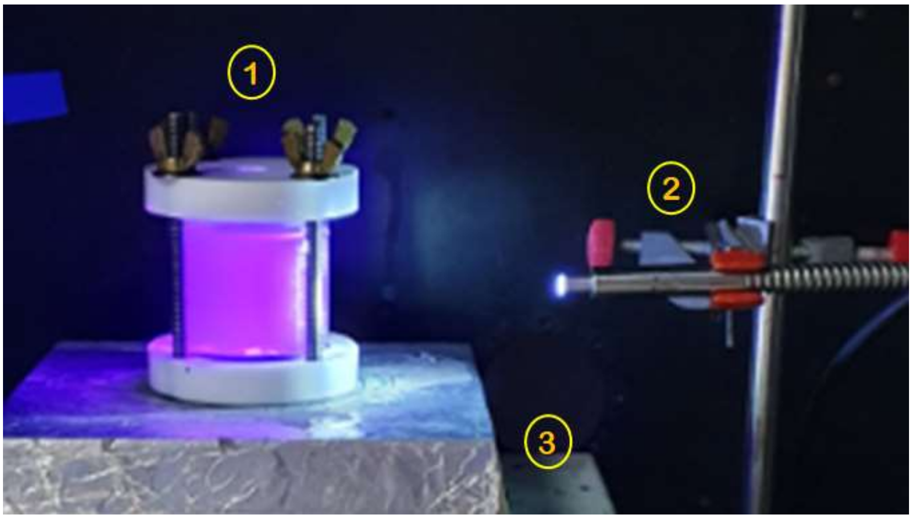

Figure 19. Photocatalysis experimental setup, in which (1) is the reactor containing the perovskite/CV solution, (2) is the Xe arc lamp, and (3) is the magnetic stirrer.

Characterization techniques

- *X-ray diffractometry (XRD)*

The X-ray diffraction measurements were performed at São Carlos Institute of Chemistry (IQSC), for the powder samples, utilizing a Bruker XRD, D8 advance model, with Cu (Kα = 1.518 Å) radiation source, at room temperature and PSD detector LynxEye model.

- *Raman scattering spectroscopy*

Raman Scattering spectroscopy analyses of the powder samples were done at São Carlos Institute of Chemistry (IQSC) using a LabRAM HR Evolution Raman spectrometer by Horiba, utilizing a HeNe laser (633nm), in the range of 10 to 400 cm^{-1}.

- *Scanning electron microscopy (SEM)*

Scanning electron microphotographs of the powder samples were taken also at São Carlos Institute of Chemistry (IQSC) utilizing ZEISS LEO 440 (Cambridge, England) with an OXFORD model 7060 detector, operating with an electron beam of 15kV, 2.82A current and 200 pA probe I.

- *Diffuse reflectance spectroscopy (DRS)*

Diffuse reflectance spectroscopy measurements were realized at São Carlos Institute of Chemistry (IQSC) utilizing a Shimadzu UV-Vis-NIR spectrophotometer model UV 3600, using $BaSO_4$ as standard, from 250 to 800 nm for samples as powders.

- *UV-Vis in photocatalysis*

Electronic absorption spectra were collected at São Carlos Institute of Chemistry (IQSC) after irradiation with a USB 4000 spectrometer (Ocean Optics, FL, U.S.A.) equipped with a P400-2 UV/Vis optical fiber and an LS1 tungsten halogen lamp.

- *Photoluminescence*

At the Chemistry Department of FFCLRP the photoluminescence analyses were performed using a Flurolog 3 Horiba Scientific (model FL3-22) equipment with dual excitation and emission monochromators, H10330-75 (NIR) and Hamamatsu R928 (Visible) photomultipliers. A pulsed Xe lamp of 450 W and a 980 nm laser was employed for the excitation and emission spectra.

- *Zeta potential*

The zeta potential analyses were measured in a Zetasizer Nano ZS by Malvern Panalytical situated at Chemistry Department of FFCLRP. The powder samples were dispersed in water to perform zeta potential analysis.

6. Results and discussion

6.1. Lead-free double perovskites for photocatalysis

6.1.1. Material characterization

Using the tolerance factor (τ) exhibited in equation 3, it was possible to predict the proposed perovskite structure stability, in this case, for $Cs_2Ag_xNa_{1-x}BiCl_6$ when x = 0 or 1, for example. Equation 3 measures the stability for ABX_3 perovskites, although, for $ABB'X_6$ double perovskites r_B can be the arithmetic mean of the two B-site radii.[29]

$$\tau = \frac{r_X}{r_B} - n_A \left(n_A - \frac{\frac{r_A}{r_B}}{\ln \frac{r_A}{r_B}} \right) \tag{3}$$

For $Cs_2AgBiCl_6$; $\tau = \frac{1.81}{1.09} - 1 \left(1 - \frac{\frac{1.78}{1.09}}{\ln \frac{1.78}{1.09}} \right) \therefore \tau = 3.99$

For $Cs_2NaBiCl_6$; $\tau = \frac{1.81}{1.025} - 1 \left(1 - \frac{\frac{1.78}{1.025}}{\ln \frac{1.78}{1.025}} \right) \therefore \tau = 3.92$

Therefore, since all perovskite presenting a $\tau < 4.18$ are stable,[29] both values for $Cs_2AgBiCl_6$ and $Cs_2NaBiCl_6$ perovskites are in agreement with the proposed value, it means that they exhibit a stable crystal structure, e.g., perovskite crystal structure can be achieved. Since the two extreme compositions were calculated and are stable, there is no need to calculate the intermediary compositions.

According to the crystallography database of lead-free double halide perovskite (LFDP), it exhibits cubic crystal system with *Fm3m* space group. LFDP presents lattice parameter of 10.78 (A) 10.78 (B) and 10.78 (C) Å, $\alpha = \beta = \gamma = 90^o$, and cell volume of 1251.65 $Å^3$.[154] A previous work showed the end members bond distances d(Cs-Cl) = 3.8102 Å, d(Ag-Cl) = 2.707 Å, and d(Bi-Cl) = 2.681 Å for $Cs_2AgBiCl_6$ perovskite.[154] All Bi-based samples synthesized showed high crystallinity and their diffractograms are presented in Figure 20.

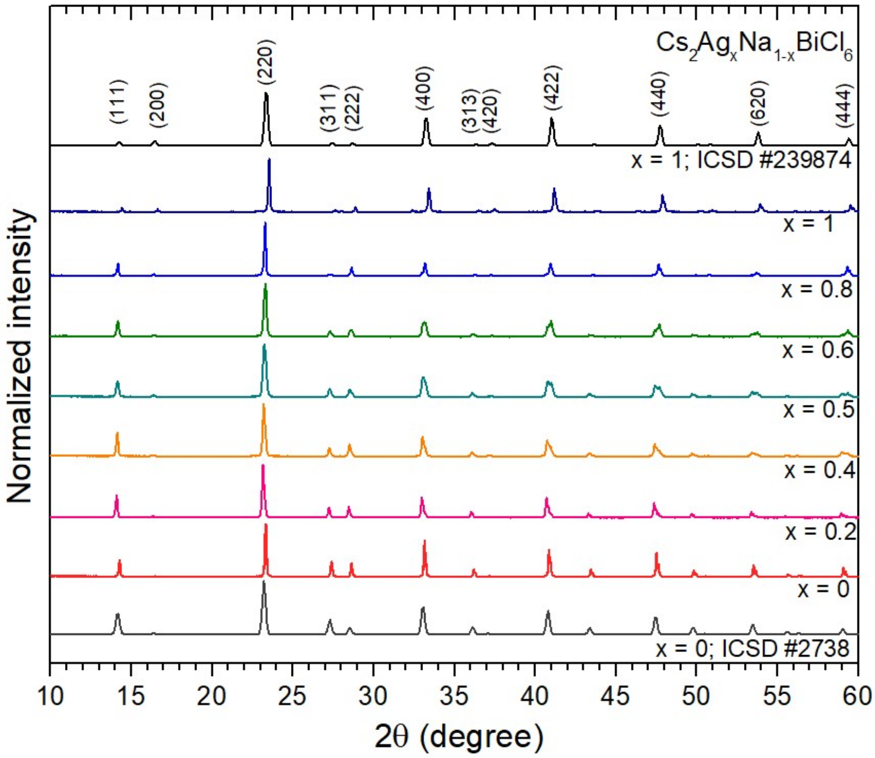

Figure 20. XRD diffractograms of $Cs_2Ag_xNa_{1-x}BiCl_6$ samples varying x from 0 to 1.

In Figure 20 it is possible to notice the formation of Bi-based perovskite in a cubic phase according to the $Cs_2AgBiCl_6$ patterns. The characteristic peaks assigned to the planes (111), (200), (220), (311), (222), (400), (313), (420), (422), (440), (620), and (440) are presented for all samples.[60,155] A slight shift in 2θ can be noticed for the synthesized samples, and it is evident for the most intense peak at 2θ = 23.4º (220). This shift might be attributed to an instrumental error became from the XRD equipment (sample's height), since there was no gradual shift from Ag1.0 to Ag0.0. Moreover, the gradual decrease of (200) peak intensity and the increase of (111) imply the increase of Na concentration towards $Cs_2NaBiCl_6$ composition.[155] Other two peaks which show this evolution are (311) and (222), which increase as the Ag content decrease, according to the XRD data presented in the literature.[155] In this sense, XRD of $Cs_2Ag_xNa_{1-x}BiCl_6$ samples gave a glimpse of the successful formation of Ag/Na mixed perovskite, which were used in photocatalysis experiments. Also, the colors of Ag/Na mixed perovskites gradually migrate from off-white to yellowish as the Ag content increases, as shown in Figure 21. This color change happens due to the shift of the band gap to higher E_g. Moreover, Bi-based perovskite crystallite sizes were calculated and are presented in the supplementary materials.

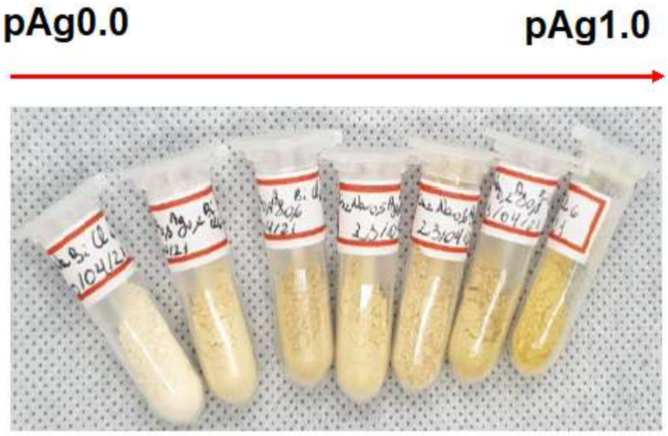

Figure 21. Photograph of $Cs_2Ag_xNa_{1-x}BiCl_6$ samples.

Raman spectroscopy was performed for perovskite structural characterization. As presented in Figure 22, Bi-based perovskite samples exhibited three vibrational modes below 400 cm^{-1}, attributed to the three vibrational modes of $AgCl_6$ and $BiCl_6$ octahedron[156,157]. The band centered at 115 cm^{-1} is assigned to the bending vibration of Ag–Cl and Bi–Cl bonds with T_{2g} symmetry. Bi-Cl bonds exhibits major influence on T_{2g} vibrational mode as with the decreasing of Ag content there were just a slight change in 115 cm^{-1} band. The band located at 213 cm^{-1} is assigned to E_g vibrational mode of $AgCl_6$ octahedron, and 282 cm^{-1} are related to the stretching vibrations of both $AgCl_6$ and $BiCl_6$ octahedra with A_{1g} symmetries. As showed in Figure 22, all bands exhibited a slight shift to lower wavenumber as the Ag content decreases. It is noticed that E_g and A_{1g} modes suffered the major influence by this lack of Ag, because of a significant tunning of these two bands with decrease of Ag content. There is a shift of each band decreasing Ag content. For the band centered at 115 cm^{-1} assigned to the T_{2g} vibrational mode, a shift from 115 (Ag1.0) to 112 cm^{-1} (Ag0.0) is observed. For A_{1g} vibrational mode the band shifted from 281 (Ag1.0) to 278 cm^{-1} (Ag0.0), also a shift of 2.5 cm^{-1}, implying a phonon energy lowering as Ag content decreases in the lattice.

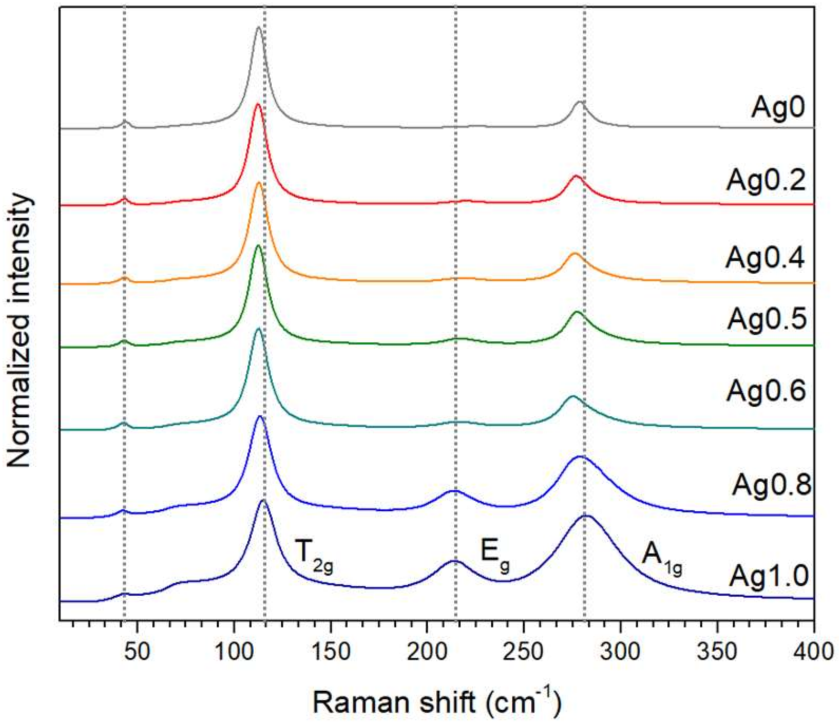

Figure 22. Raman spectra for $Cs_2Ag_xNa_{1-x}BiCl_6$ samples.

In order to obtain a better knowledge of the Bi-based perovskite morphology, scanning electron microscopy (SEM) was performed. It provided a general idea of the particle size and size distribution of perovskite powders. Figure 23 shows the SEM images for $Cs_2NaBiCl_6$ and $Cs_2AgBiCl_6$ samples, respectively.

From SEM images the powder sized at the micrometer range with a sorted size distribution. In both cases, there are bigger particles surrounded by minor ones, although, in the case of pAg0.0 it is possible to observe octahedral shapes particles. The sample Ag0.0 in Figure 23(a) and (b), exhibited an unexpected pattern resembling two different materials. Because of that, energy dispersive x-ray spectroscopy (EDS) was performed, and it assured the same composition of the smaller and the bigger particles, as shown from the EDS spectra in the supplementary materials.

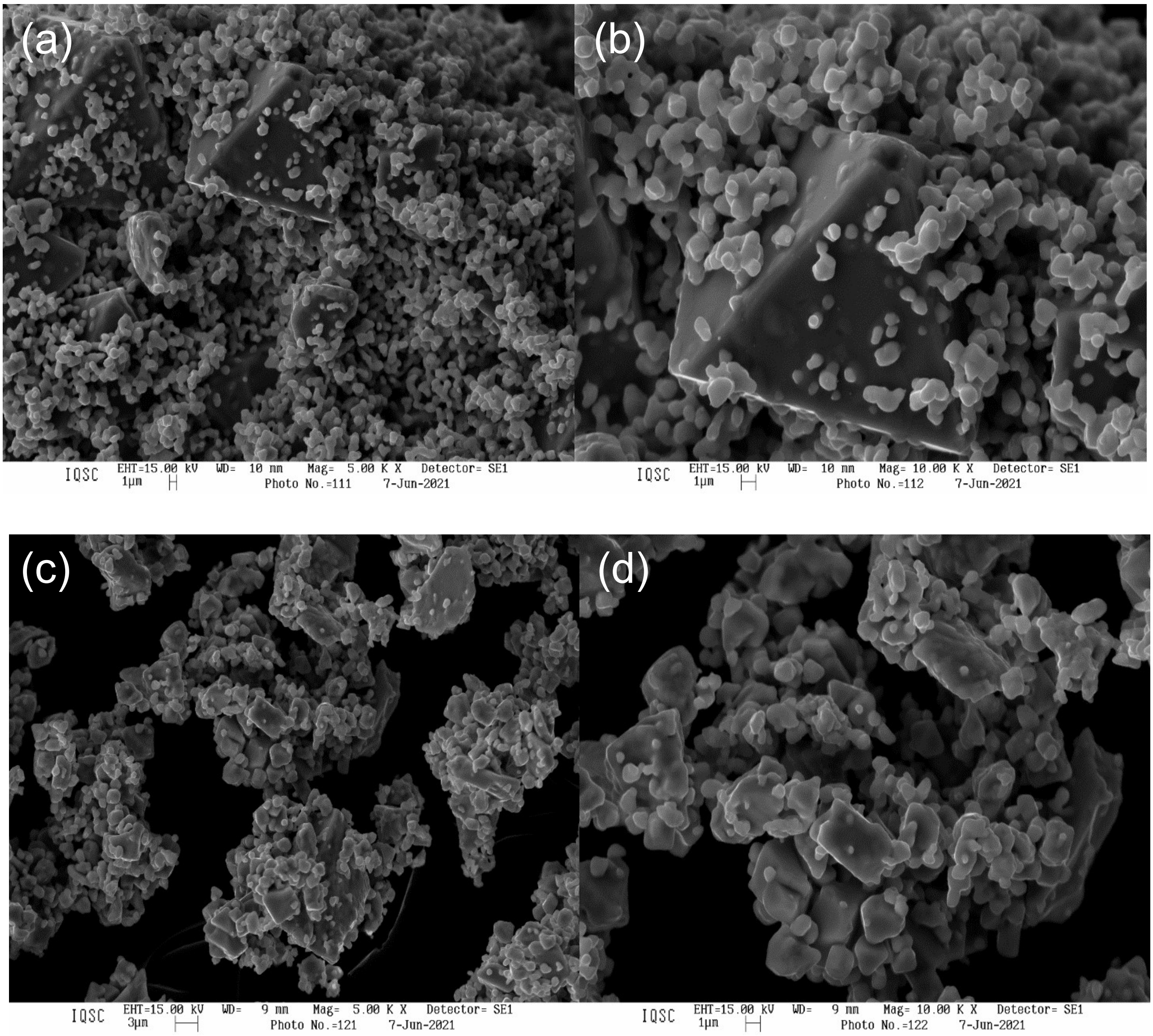

Figure 23.Scanning electron microscopy images for pAg0.0 (a and b) and pAg1.0 (c and d)

6.1.2. Photocatalytic activity experiment

Several experiments were performed to understand the photocatalytic activity of Bi-based perovskites. First, the experiment to evaluate the adsorption of crystal violet dye on the perovskite surface was performed by dispersing 35 mg of powder in 35 mL of pure water and 35 mL of CV solution (20 ppm), resulting in a 70 mL final solution with 0.5 g.L^{-1} of perovskite and 10 ppm of organic dye. The solution was covered and kept in dark under stirring to avoid undesirable photocatalysis events, for 120 min. Every 5 or 10 min an aliquot was taken from the solution and the absorption spectra recorded to monitor the CV absorption band at 582 nm until the solution reaches the equilibrium, i.e., no adsorption, as shown in Figure 24.

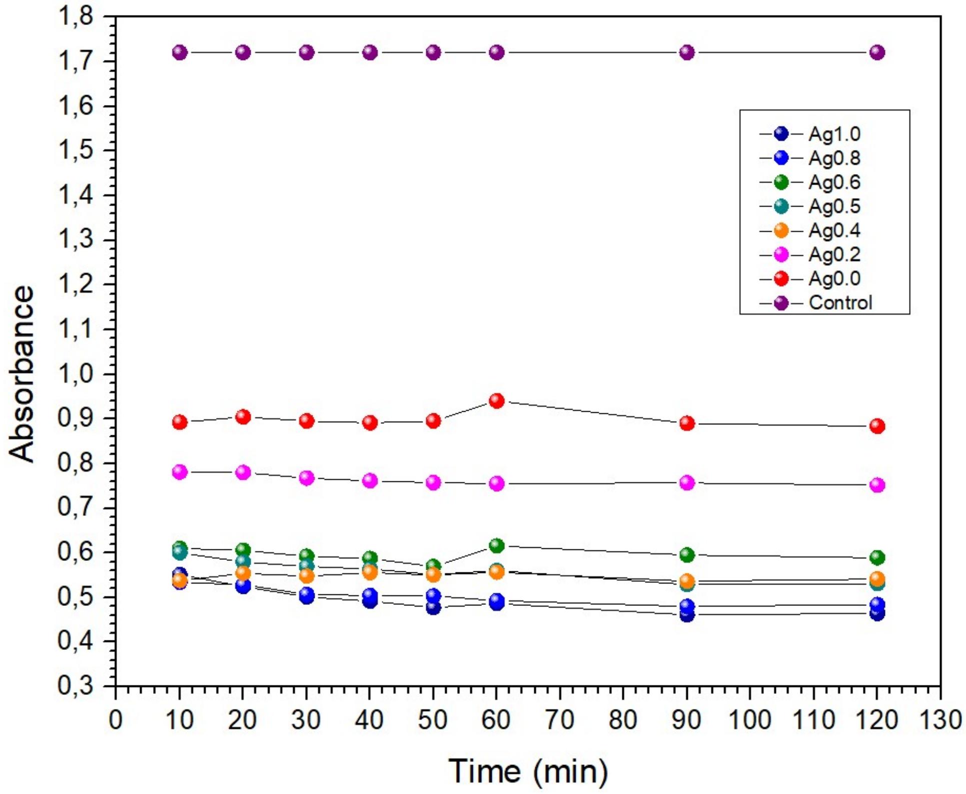

Figure 24. Evaluation of adsorption ability of $Cs_2Ag_xNa_{1-x}BiCl_6$ perovskites.

Figure 24 show the absorbance behavior as function of time. All samples behave similarly, and a small adsorption occurs from 10 to 120 min. Thus, 60 min of dark adsorption time was chosen to minimize adsorption effects on the photocatalysis results. This experiment also allowed us to conclude that the perovskite possesses a high adsorption strength since the pure CV dye presents an initial absorbance of 1.72 at concentration of 10 ppm. pAg1.0 and pAg0.8 samples were those that mostly adsorbed the organic dye. Since this adsorption can be related to the perovskites surfaces charges, zeta potential measurement was performed to understand this behavior for each sample. The zeta potential values for the perovskites are listed in Table 3.

Table 3. Zeta potential analysis for Ag/Na mixed perovskite samples.

Samples	Zeta potential (mV)
pAg1.0	-8.97
pAg0.8	-12.7
pAg0.6	-12.4
pAg0.5	-13.6
pAg0.4	-11.7
pAg0.2	-16.7
pAg0.0	-18.2

pAg1.0, pAg0.2, and pAg0.0 samples presented zeta potentials in accordance with adsorption test. Sample pAg0.0 exhibit the highest negative zeta potential value and presented the lowest adsorption, followed by pAg0.2 sample, the second highest negative zeta potential and second lowest CV adsorption. pAg1.0 perovskite showed highest CV adsorption and the lowest negative zeta potential. Zeta potential results were quite unusual since crystal violet dye is a cationic dye, it was expected Ag1.0; Ag0.8, i.e., samples with the lowest negative Z potential to exhibit less adsorption than the samples with the highest zeta potential. Zeta potential analysis gives surface charge, this test suggests that perovskite possess negative surface charge, probably due to Cl^- present in its crystal structure, like it is shown in Figure 6. This negative charge results in a higher adsorption of cationic dyes onto perovskite's surface area. Adsorption experiment and zeta potential analysis were not in agreement with each other, needing a deeper investigation of Bi-based perovskite stability. The Xe arc lamp spectra used to irradiate the solutions under stirring is present in the supplementary materials.

The total light irradiation period was 90 min, and aliquots were taken every 5 min for the first six turns and then every 10 min. Each aliquot was centrifugated and their absorption spectrum measured to follow the CV photodegradation, as shown in Figure 25 and Figure 26.

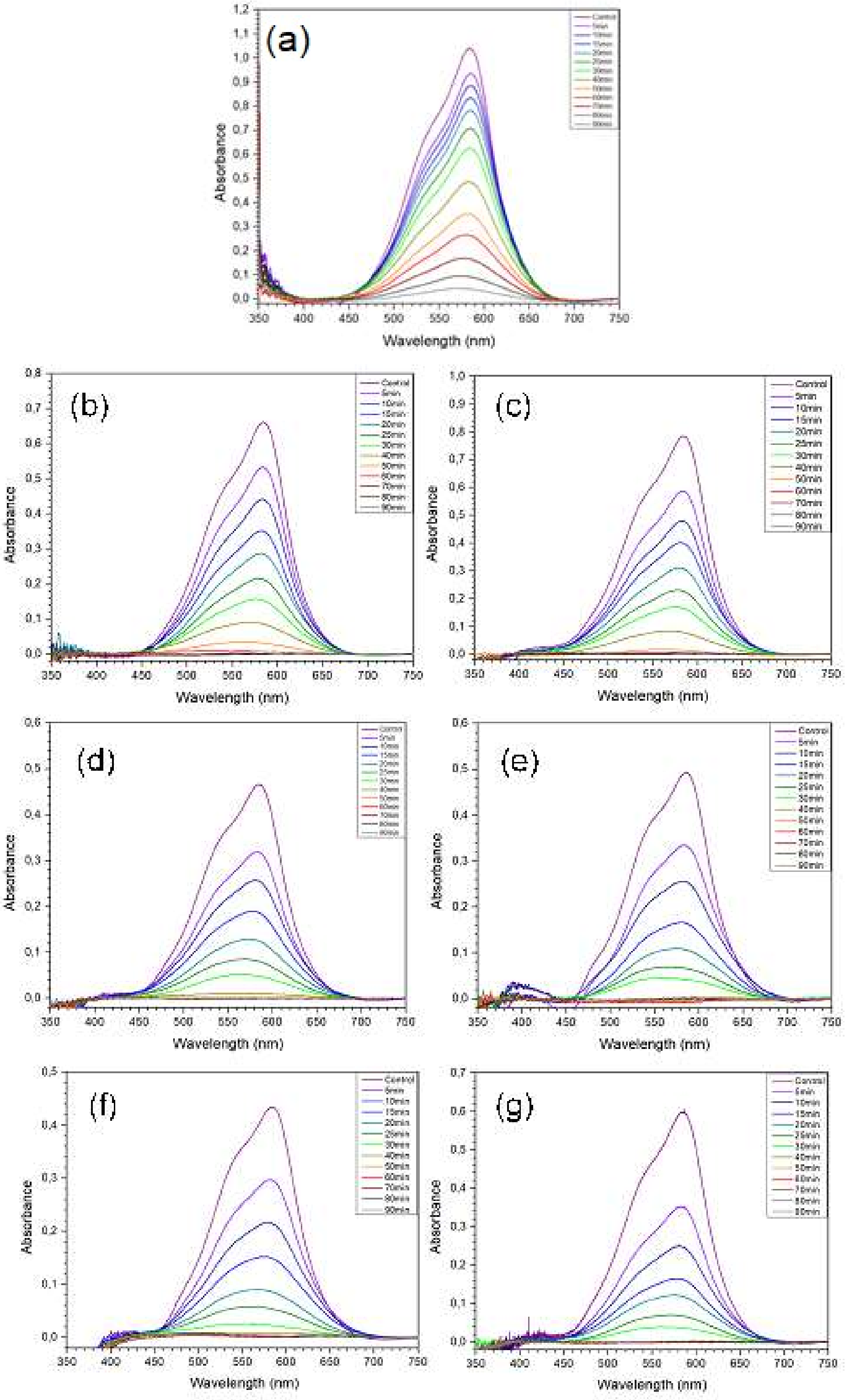

Figure 25. UV-Vis spectra of organic dye degradation by (a) pAg0.0, (b) pAg0.2, (c) pAg0.4, (d) pAg0.5, (e) pAg0.6, (f) pAg0.8 and (g) pAg1.0 photocatalysis.

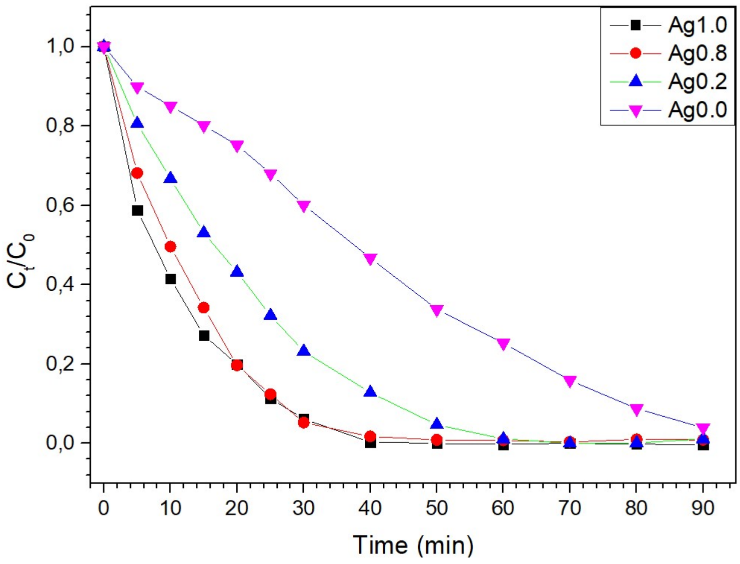

Figure 26. Photodegradation curve for Ag1.0, Ag0.8, Ag0.2 and Ag0.0 samples.

As shown in Figure 25 and Figure 26, all samples could fully photodegrade the CV dye, except the pAg0.0. The differences between the photodegradation kinetics among the samples can be seen by first analyzing the pAg1.0, pAg0.8, and pAg0.6, in which more than 30 min is needed to completely photodegrade the dye, while pAg0.5 sample required 40 min. On the other hand, pAg0.4 and pAg0.2 samples demanded more than 50 min to completely photodegrade the CV dye. In Figure 26 it become clearer, the difference between Ag1.0, Ag0.8, Ag0.2 and Ag0.0 CV photodegradation, in other words, the influence of Ag content in Bi-based perovskite kinetics. These results enable to recognize that Bi-based perovskites samples exhibited a promising photocatalytic activity, in which the Ag content exhibited a significant role in perovskite photocatalysis since its photocatalytic activity decreases with the decrease of Ag content. This might be related to Ag electronic properties, demanding a deep investigation to completely understand its photocatalytic role. Therefore, to measure the Ag role on the perovskites photocatalysis, the kinetics were calculated as function of silver concentration. It was assumed that a first-order reaction occurs according to equation 12.

$$ln[A]_t = ln[A]_0 - kt \tag{12}$$

where $[A]_0$ and $[A]_t$ is the initial and the concentration at time t, respectively; k is the reaction rate constant and t the time of reaction. Using equation 12 to know the k value, both side of equation 12 were raised to the exponent e, leading to equation 13.

$$[A] = [A]_0 e^{-kt} \tag{13}$$

Using equation 13 it was possible to obtain the reaction rate constant for each photocatalytic test by doing an exponential fit.

Sample pAg1.0 presented a reaction rate constant k of 0.0898. Figure 28 show the k values as function of Ag content.

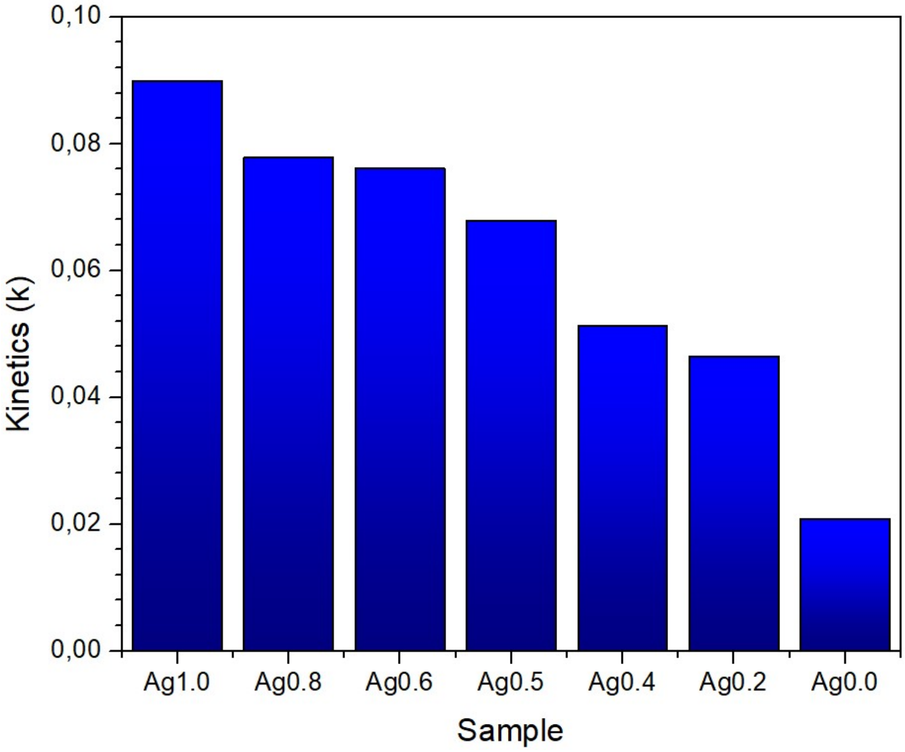

Figure 27. Bar graph of $Cs_2Ag_xNa_{1-x}BiCl_6$ reaction rate coefficient.

Figure 27 shown that from pAg0.2 to pAg1.0 sample, the k constant increased almost 2 times. However, from pAg0.0 sample to pAg1.0 Ag, the k constant increased more than 4.5 times. This result implies and highlights the crucial role of Ag in the photocatalysis process, because comparing the minimal Ag content to the highest the kinetic increased 2 times and when there is no Ag to only Ag content in perovskite composition, its kinetics increased 4.5 times. However, this analysis needs external information to be reliable, precisely, it needs the information of the given bandgap absorption, because it also can impact on the perovskite photocatalytic properties, since the process involves electronic transition. In this sense, diffuse reflectance spectroscopy was performed for all samples, followed by the Tauc plot of the optical bandgap, and shown in Figure 28.

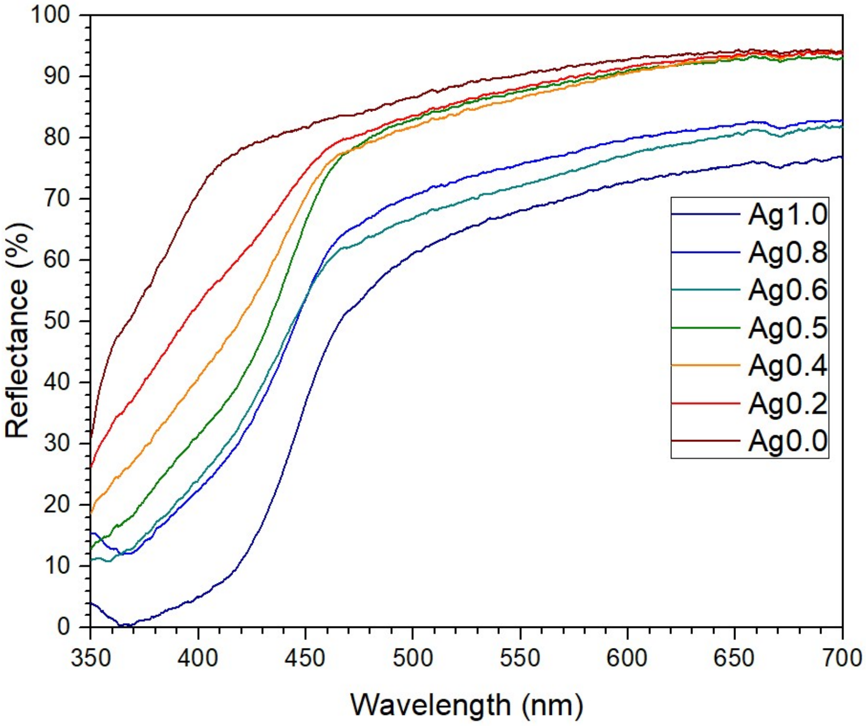

Figure 28. Diffuse reflectance spectra of $Cs_2Ag_xNa_{1-x}BiCl_6$ samples.

Using the DRS data, the bandgap was calculated from Tauc plot. Tauc plot method was followed based on Makula work and using the equation 14.[159]

$$(F(R_\infty)h\nu)^{1/\gamma} = B(h\nu - E_g) \tag{14}$$

Where $(F(R_\infty)$ is the Kubelka-Munk function, h is the Planck constant, ν is the photon's frequency, E_g is the bandgap energy, B is a constant and γ is a factor dependent of the bandgap nature, i.e., direct, or indirect bandgap. When the electron transition is direct γ factor is ½ and when its nature is indirect γ is 2. Using γ as 2, due to the intrinsic indirect bandgap of these type of perovskites and utilizing equation 16, was possible to plot and calculate the optical indirect bandgap.

The optical bandgap calculation was estimated by extrapolating the linear portion of the pAg1.0 Tauc plot, for instance. For Ag1.0 sample, the indirect bandgap was 2.70 eV, similar with that found in the literature, 2.84 eV.[157] All optical bandgaps are listed in Table 4.

Table 4. List of the measured bandgaps along with the correspondent kinetic constants for $Cs_2Ag_xNa_{1-x}BiCl_6$ by Tauc method.

Samples	**Bandgap ±0.03 (eV)**	**Kinetic constants**
pAg1.0	2.70	0.0898
pAg0.8	2.50	0.0778
pAg0.6	2.51	0.0760
pAg0.5	2.52	0.0678
pAg0.4	2.49	0.0512
pAg0.2	2.49	0.0464
pAg0.0	3.33	0.02081

As for the pAg1.0 sample, pAg0.0 sample also presented a similar bandgap value compared to other previous work of about 3.49 eV.[156] Both values are a little lower than those presented, although it might be related to the synthesis pathway adopted and/or pH of the synthesis route, once it is known that these factors can influence in its bandgap energy.[60] Beyond that, all intermediate Ag concentration perovskites exhibited almost identical bandgap values as listed in Table 4. The kinetics and bandgap calculation highlights the influence of Ag in perovskite photocatalysis. Ag content prevents a high energy bandgap for Bi-based perovskites. Preventing this high energy bandgap will ensure that perovskites bandgap will not shift to lower wavelengths, such as UV, keeping the bandgap in the visible range, which is desired for photocatalytic application using sunlight. Furthermore, high bandgap energy as exhibited by Ag0.0 sample interfere on the perovskite photocatalytic performance as showed by its low kinetics compared with the remaining samples. In addition, even though the intermediary Ag content perovskites exhibit almost the same bandgap energy, the higher concentration of Ag in perovskites composition implies in better and more efficient photocatalysis since the kinetics increase with higher Ag concentrations.

The covalent character of each sample must be carefully analyzed to have a more consistent and chemical conclusion about the Ag content influence on perovskite's photocatalysis. For instance, Ag-Cl bond exhibits a much higher covalent character than Na-Cl bond (an ionic chemical bond), and it will strongly affect perovskite's optical properties. The perovskite's bandgap energy suffered a huge increase of approximately 0.8 eV going from the samples containing Ag content (2.5 and 2.7 eV) to the no Ag sample (3.33 eV), as prof of the Ag impact on perovskite's optical property. Moreover, Ag shows a high polarizing character which can exert a high influence on the electronic distribution of the perovskite, being able to modify the perovskite photocatalysis performance as observed.

Bi-based perovskites stability after photocatalysis experiment

Because of the unusual disagreement between zeta potential and adsorption analysis, and to investigate Bi-based perovskites crystallinity after photocatalysis experiment, x-ray diffractometry analysis was performed again for all samples after this experiment. Figure 29 exhibited the x-ray diffractograms of Bi-based samples after photodegradation test.

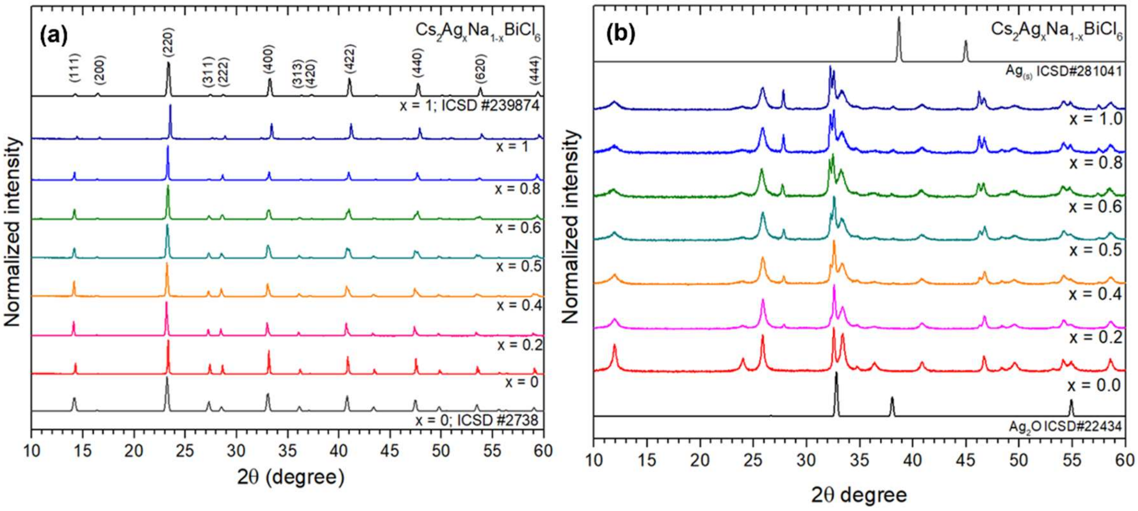

Figure 29. XRD diffractograms for $Cs_2Ag_xNa_{1-x}BiCl_6$ (x varying from 0 to 1) samples before (a) and after (b) the photocatalytic activity test.

Comparing the diffractograms before (Figure 20) and after (Figure 29) the photocatalysis experiment, it is observed that Bi-based perovskite might not be stable in aqueous solution. All samples containing Ag content exhibited a very similar diffractogram, leading to conclude that despite a possible crystallinity structure degradation it might be related to the organic dye adsorbed in its surface. Some possible options of sample degradation are the formation of metallic Ag and/or Ag_2O, although all spectra are similar in terms of peak position and intensity, so it was not considered. There is a peak increase around $2\theta = 27^o$ while increasing Ag content. On the contrary, the two peak around 33° decreases with higher concentration of silver. As it seems, there is no correlation with Ag_2O or $Ag_{(s)}$ due to the incompatibility of the samples diffractogram with the patterns diffractograms.[160,161] However, this structural change, probably a decomposition of perovskite's structure might be related to some Ag byproduct, AgCl, for instance. Furthermore, Ag0.0 perovskite also exhibited a similar diffractogram with some different peak positions and intensities. Therefore, it is needed an even more deep and detailed analysis of these perovskites' stability.

6.2. Lanthanide-doped Perovskites: Photoluminescence

6.2.1. Synthesis and characterization of RE3+-doped perovskites

For the In-double perovskites, it was also calculated the tolerance factor (τ) to predict its structure stability.

$$\text{For } Cs_2AgInCl_6;\ \tau = \frac{1.81}{0.975} - 1\left(1 - \frac{\frac{1.78}{0.975}}{ln\frac{1.78}{0.975}}\right) \therefore \tau = 3.89$$

Therefore, In-based perovskite also presents a stable crystal structure according to equation 3. Bi/In-based perovskites do not require the calculation of the tolerance factor since both extremes are stable.

In-based perovskites present the same crystalline structure of Bi-based perovskites: they exhibit a cubic crystals system and *Fm3m* space group, as shown in Figure 20. Both structures show lattice parameters of 10.48 Å for A, B and C but with a cell volume of 1151.21 Å^3 for In-based perovskite.[162] These parameters are for $CsAgInCl_6$ perovskites, however, the addition of Bi increase the lattice and cell volume because Bi^{3+} (1.03 pm) is larger than In^{3+} (0.80 pm). Previous works showed end members distances as d(Ag-Cl) = 2.716 Å and d(In-Cl) = 2.525 Å for pIn sample. For the photoluminescence studies, four In-based perovskite samples were synthesized: pIn, pIn0.9, pAg0.6In, and pAg0.6In0.9.

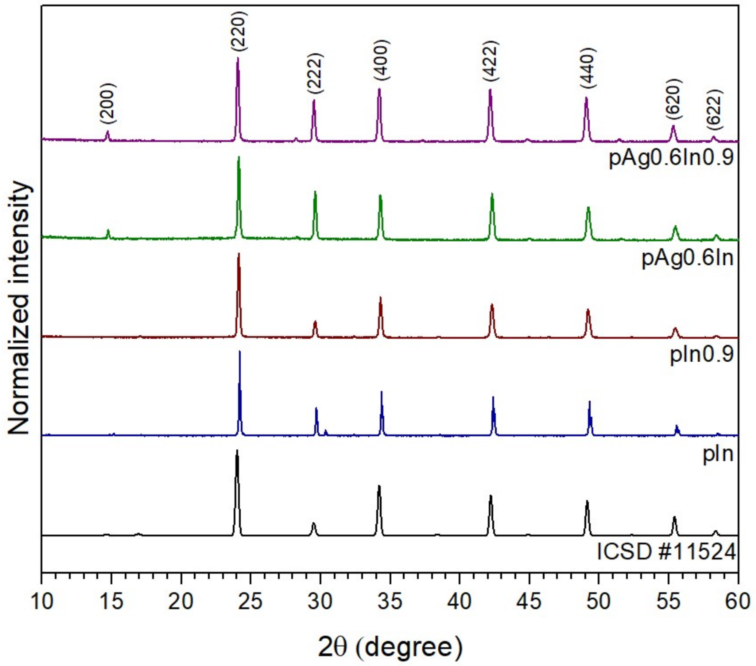

Figure 30. X-ray diffractograms of In-based perovskites.

Observing the diffractograms exhibited in Figure 30, it is possible to note that a cubic phase was achieved for all by comparing with the standard XRD pattern taken from ICSD data.[154] The samples presented the characteristic peaks (200), (220), (222), (400), (422), (440), (620) and (622) for In-based perovskites.[154] The synthesized perovskites presented similar correlation comparing with ICSD number 11524, especially pIn, pIn0.9. Nevertheless, pAg0.6In and pAg0.6In0.9 showed a more intense (200) and (222) peaks compared to the other ones, consequence of adding Na content in Ag site.[155]

Except for pIn sample, pIn0.9, pAg0.6In and pAg0.6In0.9 were used as host for Ln^{3+} incorporation as listed in Table 2. Figures 32 to 34 shown the Ln^{3+}-containing In-based perovskites diffractograms. pIn sample was not doped with lanthanide ions due to its parity-forbidden transition, characteristic which is a problem for energy transfer from the host to the dopant, and because its intrinsic luminescence is very low in comparison to the others.

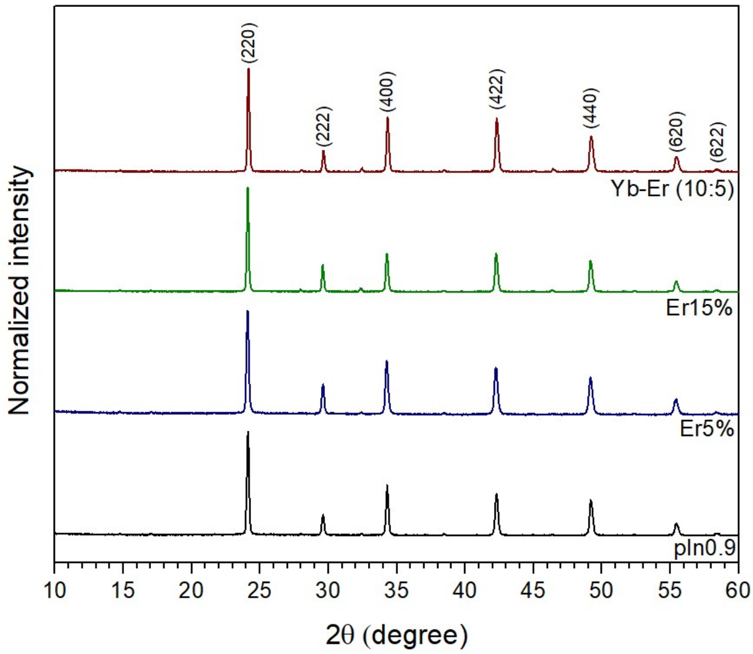

Figure 31. Diffractograms of pIn0.9, pIn0.9:Er5, pIn0.9:Er15, and pIn0.9:Yb-Er.

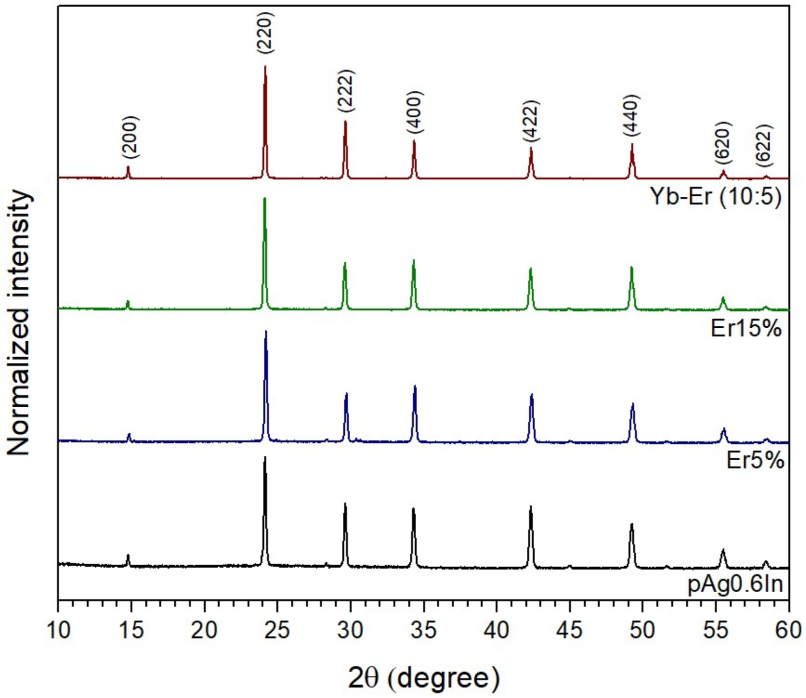

Figure 32. Diffractograms of pAg0.6In, pAg0.6In:Er5, pAg0.6In:Er15, and pAg0.6In:Yb-Er.

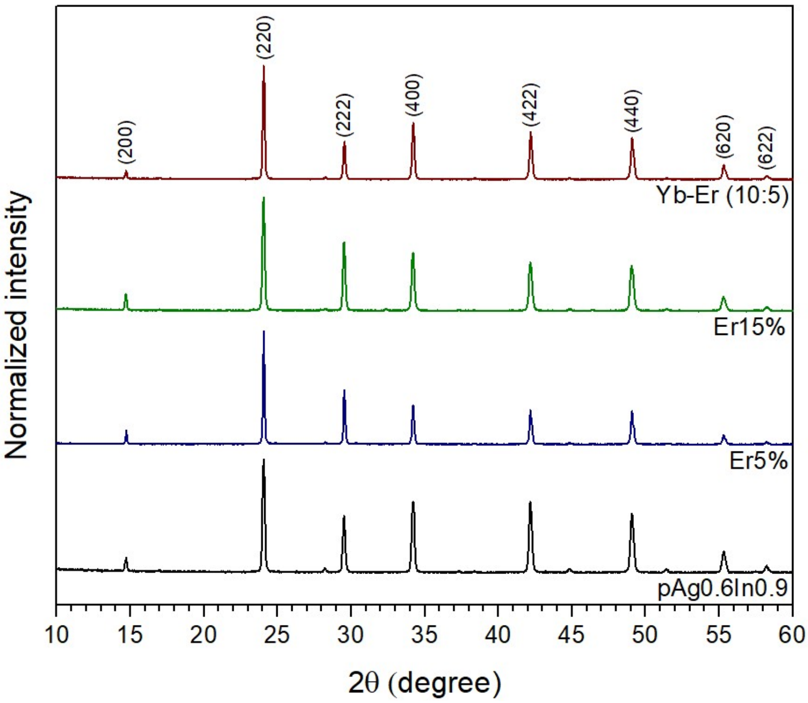

Figure 33. Diffractograms of pAg0.6In0.9, pAg0.6In0.9:Er5, pAg0.6In0.9:Er15, and pAg0.6In0.9:Yb-Er.

Ln^{3+}-containing In-based samples forms crystalline cubic phase. Despite all samples are very similar to their correspondent pattern, there are some differences among them. For instance, pIn0.9 sample show a clear difference between the intensity of (222) and (400) planes for each dopant concentration. This intensity correlation can be attributed to concentration and dopant chemical nature, like ionic radius. Doping In-based perovskite with Ln^{3+} it is expected that Yb^{3+} (0.89 Å) and Er^{3+} (0.87 Å) replaces In^{3+} (0.80 Å) in perovskite's lattice, leading to an expansion of the crystal lattice. This expansion was supposed to be noticed at the exhibited XRD noticing a slight shift to lower angles, yet as already mentioned the experimental conditions lead to some unreliable data, i.e., it is not valid to compare the peak position and/or peak intensity because it might me an error inlaid. However, there were no significant structural modifications when In-based perovskite were doped with Ln^{3+}, probably due to the similar ionic radii of RE^{3+} and In^{3+}. Undoped In-based perovskite crystallite size are also exhibited at supplementary materials.

The Raman spectra for all In-based perovskites are exhibited in Figure 34, and they presented up to five modes below 400 cm^{-1}.

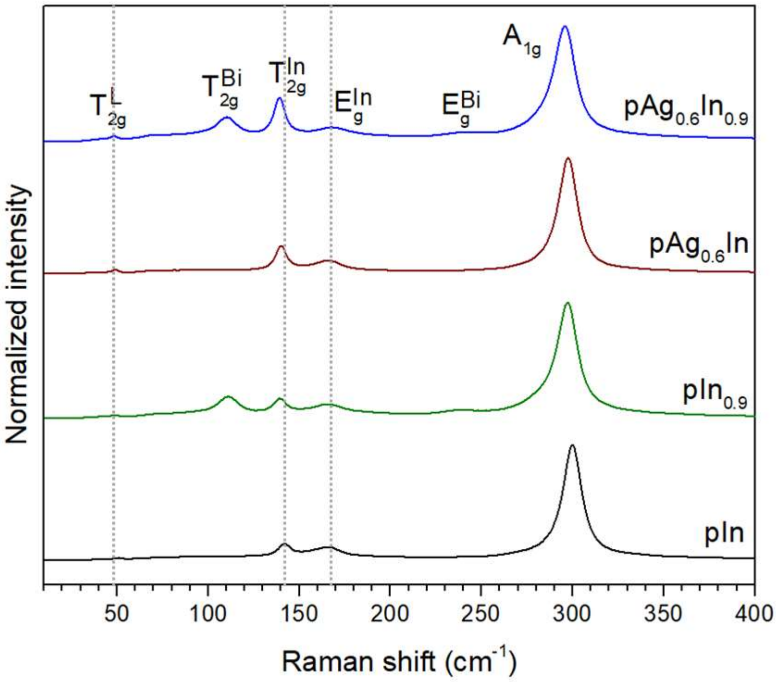

Figure 34. Raman spectra for In-based samples.

The vibrational modes for pAg0.6In0.9 sample are located at 48; 110; 139; 169; 239 and 296 cm^{-1} for T_{2g} (L), T_{2g} (Bi), T_{2g} (In), E_g (In), E_g (Bi) and A_{1g} vibrational modes, respectively. The values obtained are equivalent with the values present in the literature, however, with a slight shift since the values for each mode are from samples pIn and pAg1.0.[157,162] T_{2g}, E_g and A_{1g} vibrational modes arises from $AgCl_6$, $InCl_6$ and $BiCl_6$ octahedrons. When the composition has Bi, it is noticed the appearance of the vibrational modes T_{2g} (Bi) and E_g (Bi) located at 110 and 239 cm^{-1} assigned to Bi-Cl bonds. pIn and pAg0.6In samples present a similar Raman spectrum while pAg0.6In0.9 shows the most vibrational modes, owing to the contribution of each element. Raman spectroscopy was fundamental along with XRD analysis because, while XRD data showed the addition of Na^+ in the In-based perovskite lattice, Raman spectroscopy technique provided the acknowledgment of Bi in its structure. Not only, this technique showed that the samples with Bi exhibit a lower phonon energy due to the band assigned to Bi-Cl at lower wavenumbers. This lower phonon energy characteristic can impact In-based perovskite optical properties and will be discussed in detail latter.

In order to study the photoluminescence properties of Ln^{3+}-containing In-based perovskite samples, the diffuse reflectance, excitation and emission spectra for pIn0.9, pAg0.6In and pAg0.6In0.9 samples were performed and presented in Figure 35. Because pIn sample exhibits a parity-forbidden transition in which it disturbs its light emission process leading to an PLQY < 0.1%,[18] therefore just the other samples were analyzed.

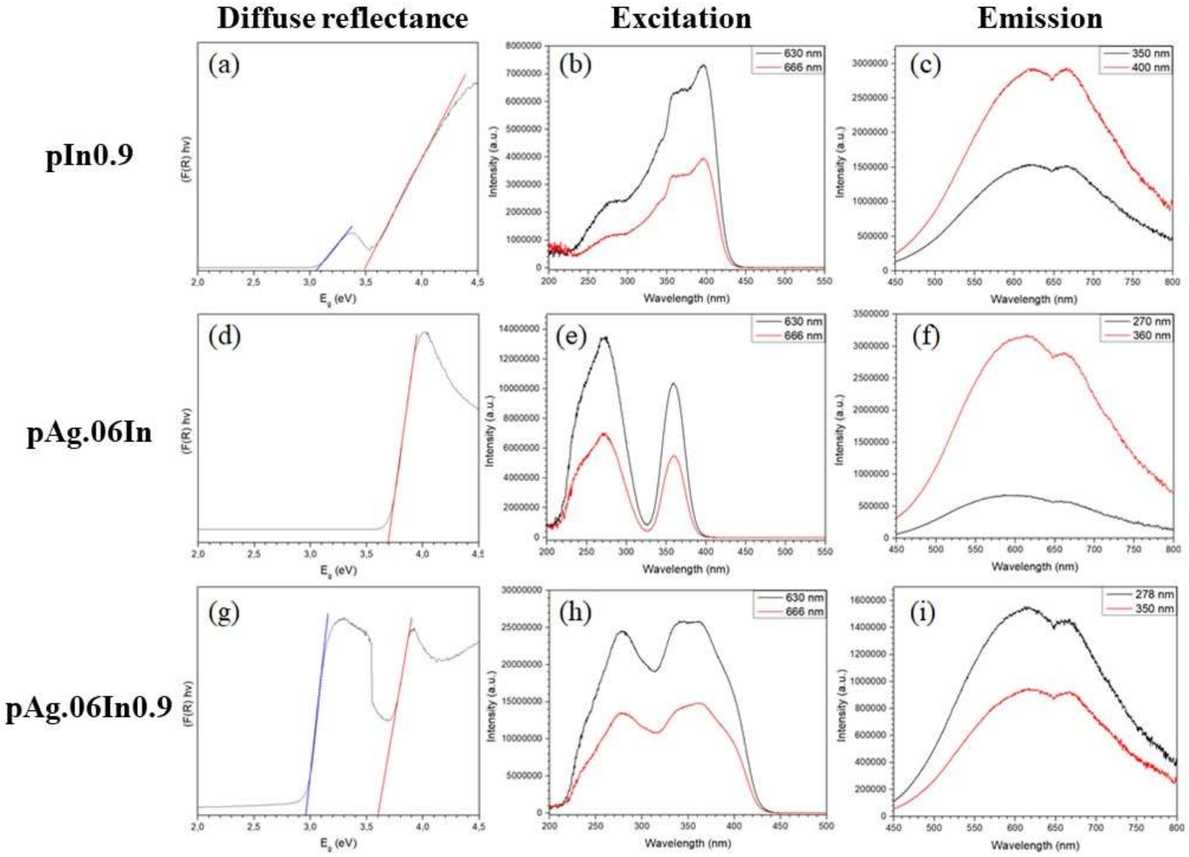

Figure 35. Diffuse reflectance (a), excitation (b), and emission spectra (c) for pIn0.9 sample; diffuse reflectance (d), excitation (e), and emission spectra (f) for pAg.06In perovskite; diffuse reflectance (g), excitation (h), and emission spectra (i) for pAg.06In0.9 sample.

As observed in Figure 35, the excitation spectra are different from each sample. For pIn0.9 and pAg0.6In sample, there are a great difference between the spectra in shape and band position. Although, for pAg0.6In0.9 sample, the contribution of Bi and Na in perovskite composition provided an excitation spectrum similarly exhibiting both pIn0.9 and pAg0.6In excitation spectra shapes. All the In-based perovskite matrix showed a high intensity excitation band when 630 nm emission is monitored. For excitation spectra, the most intense regions were 400 and 350 nm for pIn0.9, 270 and 360 nm for pAg0.6In, and 278 and 350 nm region for pAg0.6In0.9 sample. Observing the diffuse reflectance spectroscopy (DRS), pIn0.9 exhibited a bandgap energy (E_g) of 3.06 and 3.48 ±0.03 eV, pAg0.6In sample exhibited 3.69 ±0.03 eV, and pAg0.6In0.9 a E_g of 2.96 and 3.60 ±0.03 eV. All E_g values are in agreement with those presented in the literature.[21] These two values of E_g for pIn0.9 and pAg0.6In0.9 perovskites might be related to the energy gap of the material (higher eV), and the surface/ defect states (lower eV). The formation of these vacancies/defect states are associated with the addition of Bi^{3+} in perovskite lattice, since both perovskite samples containing Bi element showed the same behavior. In Figure 34, it is possible to observe that both samples which was added Bi exhibited lower phonon energies. Therefore, this lower E_g of 3.06 and 2.96 eV for pIn0.9 and pAg0.6In0.9, respectively, may be attributed to the formation of a STE.[21] For the emission spectra in Figure 35, all samples showed a similar spectrum with a broad emission from 450 to 700 nm full width at half maximum of 5.56 eV (223.15 nm) for pIn0.9, 5.75 eV (215.43 nm) for pAg0.6In and 5.75 eV (215.66 nm) for pAg0.6In0.0. Samples pIn0.9 and pAg0.6In0.9, in which indium was mixed with bismuth, showed a more intense and bright luminescence by naked eyes over the visible range compared to pAg0.6In. For the first two samples, pIn0.9 and pAg0.6In, the excitation at 400 and 350 nm, respectively, provided a more intense emission. Although, for pAg0.6In0.9 its luminescence was stronger when excited at 278 nm. Both excitation and emission spectra exhibited two bands, they are probably assigned to the band-edge absorption/emission, and the other one related to the surface/ defect states, i.e., STEs.[21] Moreover, converting the 350 and 400 nm band of pIn0.9, 270 and 360 nm of pAg0.6In, and 278 and 350 nm band of pAg0.6In0.9 sample into eV, it is reached values of 3.5 and 3.1 eV for pIn0.9, 4.6 and 3.4 eV for pAg0.6In, and 4.5 and 3.5 eV for pAg0.6In0.9 sample. The converted values are in total agreement with those presented by DRS measurement, therefore collaborating with the consistency of the previous discussion made.

The broad photoluminescence emission arises from self-trapped excitons (STEs) present in semiconductors. $Cs_2AgInCl_6$ (pIn), exhibits a parity-forbidden transition which disturbs its PLQY. Thus, to break this parity-forbidden transition, the symmetry of STE wavefunction had to be changed.[68] Since that STEs in pIn are originate from a strong Jahn-Teller distortion of the $AgCl_6$ octahedron, partially mixing Ag with an element with similar charge and radius, like alkali metals, but with different electronic configuration, it was possible to solve this problem. Alloying Na^+ into pIn solve the parity-forbidden transition situation without any phase segregation or any undesired crystal defect, due to Na+ similar charge and radius compared to Ag+.[68] Alloying Bi^{3+} into pIn composition also breaks parity-forbidden issue increasing its PLQY. The elements proportions of In-based perovskite composition were defined according to previous works presented in literature.[68,154] An illustration of perovskite light emission are presented in Figure 36.

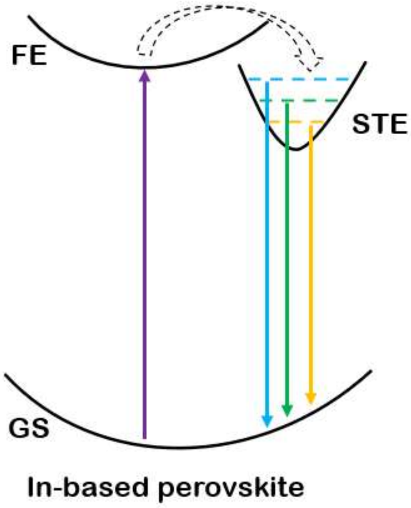

Figure 36. Scheme of light emission process in In-based double perovskite. Where FE is free exciton, STE is self-trapped exciton, and GS is the ground state.

The excitation and emission spectra of RE^{3+}-doped perovskite samples was performed to understand their photoluminescence properties. Therefore, to reach all the expected results the excitation spectra was measured monitoring 1540 nm since it is a characteristic emission of Er^{3+} transitions. Moreover, for the emission spectra it was observed the lanthanides characteristic emission at the NIR region by excitation of the matrix, and directly excitation of Ln^{3+}. The absorption and emission spectra of Yb^{3+}/Er^{3+} co-doped In-based perovskites are presented in Figure 37.

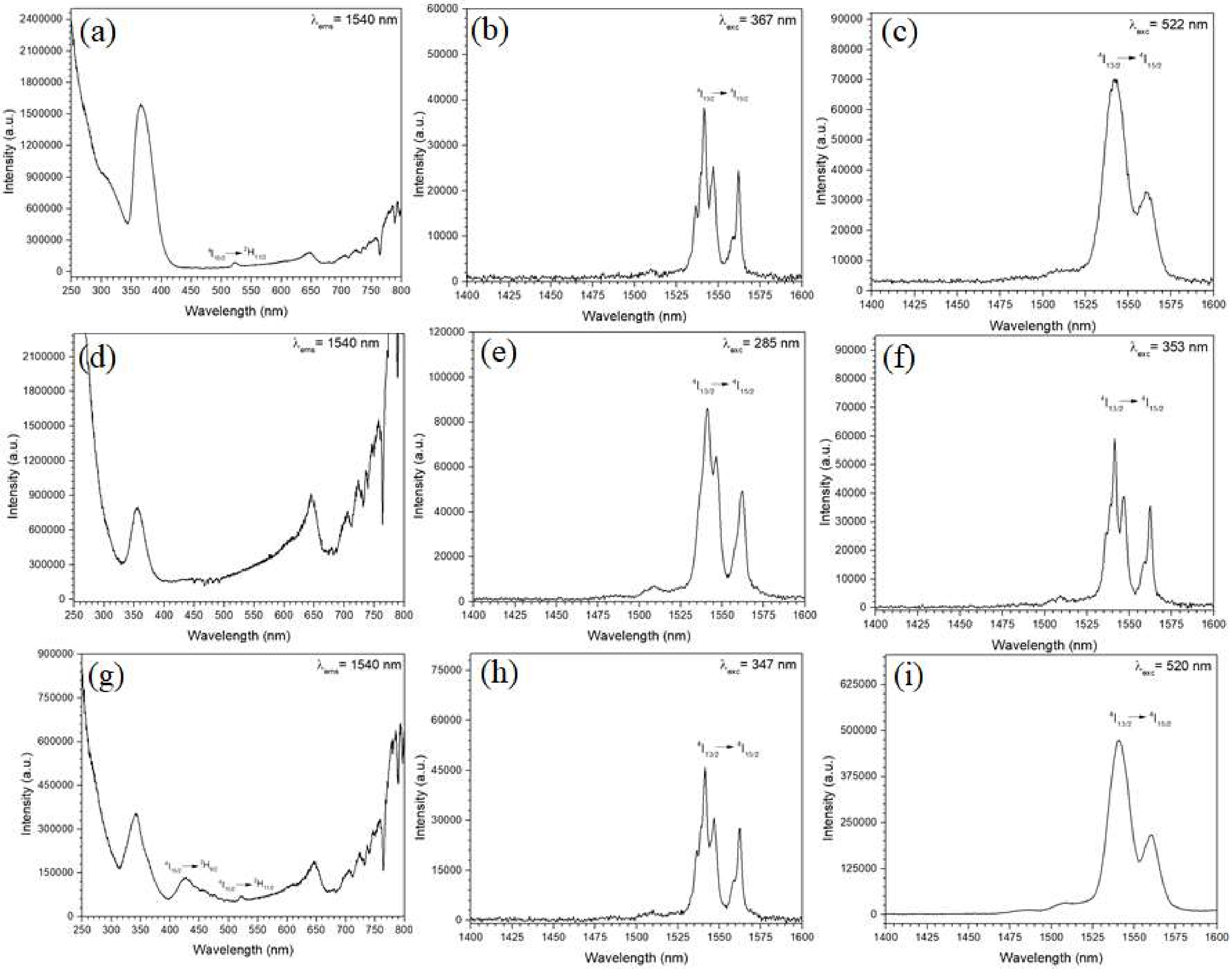

Figure 37. pIn0.9 excitation spectra at 1540 nm (a), and emission spectra at 367 (b) and 522 nm (c); pAg.06In excitation spectra at 1540 nm (d), and emission spectra at 285 (b) and 353 nm (c); pAg0.6In0.9 excitation spectra at 1540 nm (g), and emission spectra at 347 (b) and 520 nm (c).

Therefore, the excitation spectra monitoring 1540 nm assigned to the $^4I_{15/2}$→$^4I_{13/2}$ transition[163] was recorded for all three co-doped samples. Observing the emission spectra at the near infrared it was possible to state that all samples showed the $^4I_{13/2}$→$^4I_{15/2}$ transition descendant from Er^{3+}.[163] . From the emission spectra, it is noticed that either the excitation on the matrix or directly at the Er^{3+}, the characteristic NIR emission ($^4I_{15/2}$→$^4I_{13/2}$) of erbium occurs, suggesting an energy transfer of In-based perovskite matrix to Er^{3+}. Comparing the emission spectra when the excitation happens directly in theEr^{3+} with the host excitation, a difference in the spectra shapes is observed and a higher emission intensity is detected when Er^{3+} is directly excited. Despite In-based perovskite transfer energy transfer to the lanthanide ion, leading to the NIR emission, no emission is observed at the visible range. This might happen due to the strong broadband emission of In-based perovskite at the visible, and also due to radiative decay of perovskite's STE be faster (ns)[68] than erbium's lifetime (ms).[164] For the remaining Er^{3+} samples their absorption and emission spectra are presented in the supplementary material.

The up-conversion emission of the co-doped samples were obtained under excitation at 980 nm with a diode laser varying the excitation power from 200 to 1000 mW. Er and Yb-Er samples were analyzed, however herein only the co-doped samples are exhibited, the other figures are presented as supplementary material. Yb/Er co-doped In-based perovskite potency law for the three In matrix (listed in Table 2) are present in Figure 38.

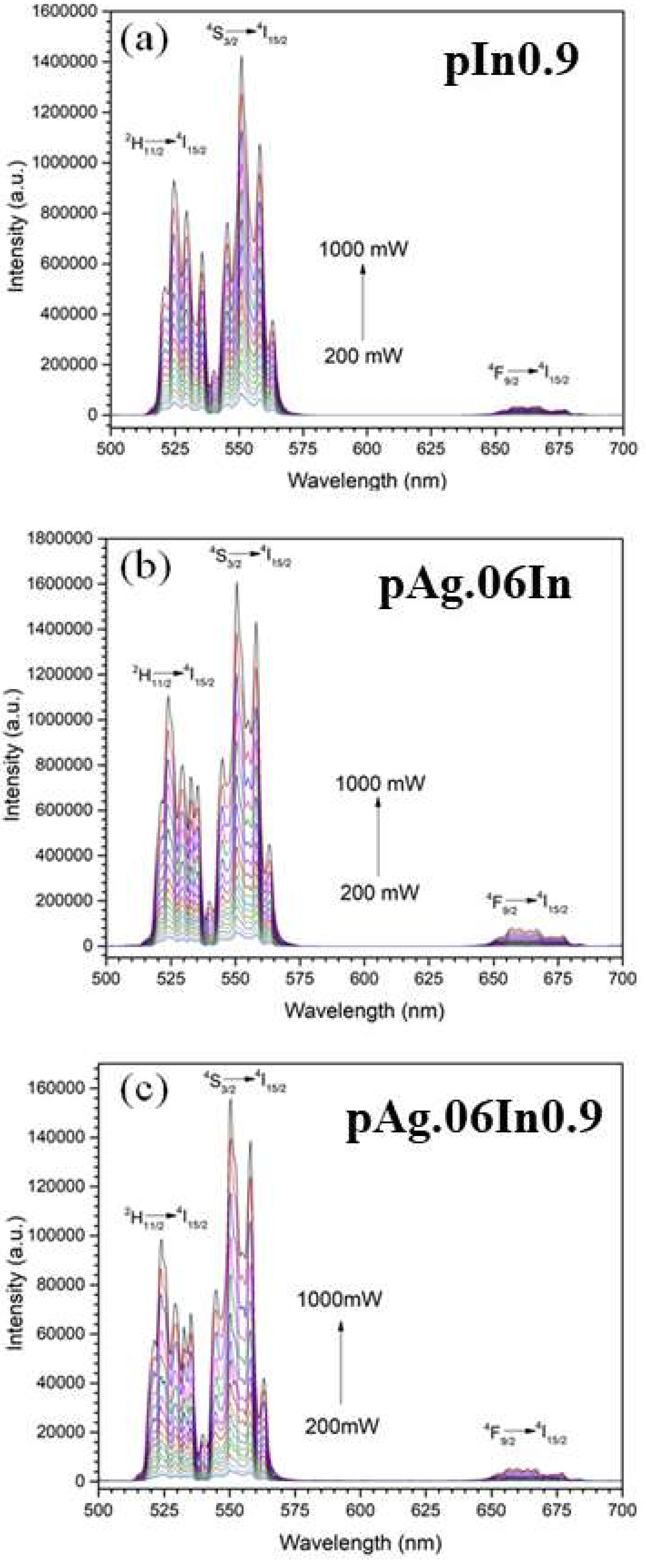
(a)
pIn0.9
$^4S_{3/2}\rightarrow{}^4I_{15/2}$
$^2H_{11/2}\rightarrow{}^4I_{15/2}$
$^4F_{9/2}\rightarrow{}^4I_{15/2}$
1000 mW
200 mW
Intensity (a.u.)
Wavelength (nm)
0
200000
400000
600000
800000
1000000
1200000
1400000
1600000
500
525
550
575
600
625
650
675
700
(b)
pAg.06In
$^4S_{3/2}\rightarrow{}^4I_{15/2}$
$^2H_{11/2}\rightarrow{}^4I_{15/2}$
$^4F_{9/2}\rightarrow{}^4I_{15/2}$
1000 mW
200 mW
Intensity (a.u.)
Wavelength (nm)
0
200000
400000
600000
800000
1000000
1200000
1400000
1600000
1800000
500
525
550
575
600
625
650
675
700
(c)
pAg.06In0.9
$^4S_{3/2}\rightarrow{}^4I_{15/2}$
$^2H_{11/2}\rightarrow{}^4I_{15/2}$
$^4F_{9/2}\rightarrow{}^4I_{15/2}$
1000mW
200mW
Intensity (a.u.)
Wavelength (nm)
0
20000
40000
60000
80000
100000
120000
140000
160000
500
525
550
575
600
625
650
675
700

Figure 38. Emission spectra of In-based perovskite co-doped with Yb^{3+}/Er^{3+} (10:5%) excited at 980 nm from 200 to 1000 mW. pIn0.9 (a), pAg0.6In (b) and pAg0.6In0.9 (c).

The presence of $^2H_{11/2}\rightarrow{}^4I_{15/2}$, $^4S_{3/2}\rightarrow{}^4I_{15/2}$, and $^4F_{9/2}\rightarrow{}^4I_{15/2}$ transitions i.e., erbium's green and red emission bands, indicated that the sample exhibited up-conversion emission under excitation at 980 nm, a process of cooperative energy transfer. A photon upconversion commonly occurs in three steps; stepwise photon absorption, energy transfer and photon emission.[165] Yb^{3+}/Er^{3+} upconversion process occurs when the Yb^{3+} transfers its energy to a close Er^{3+}, raising the electrons to higher excited states, characterizing it as an energy transfer upconversion (ETU).[166] Most likely, ETU is the process responsible for co-doped In-based upconversion, and ESA process also can contribute. ETU process is more efficient than ESA, ETU (10^{-3}) and ESA (10^{-5}), i.e., ETU is nearly two orders of magnitude more efficient than ESA process.[92,99] Not only, Er^{3+}-Er^{3+} upconversion can also occur simultaneously with Yb^{3+}-Er^{3+} upconversion, yet with a less probability of happening due to Er^{3+} smaller cross-section in comparison with Yb^{3+}. When $^2H_{11/2}$, $^4S_{3/2} \rightarrow {}^4I_{15/2}$ transition occurs, it results in green emissions going from 520 to 570 nm, respectively. Not only, when $^4F_{9/2} \rightarrow {}^4I_{15/2}$ takes place, red emission occurs ranging from 650 to 680 nm. The number of involved photons in the upconversion process for Yb^{3+}/Er^{3+}:pAg0.6In0.9 sample are shown in Figure 39.

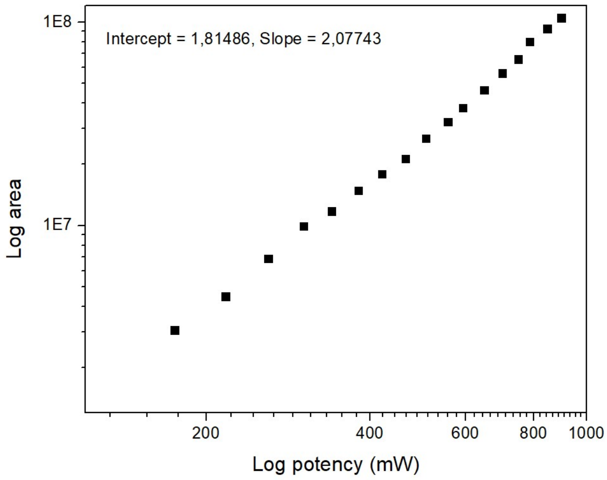

Figure 39. Graphic of potency vs area for Yb^{3+}/Er^{3+}:pAg0.6In0.9 and calculation of involved electrons in up-conversion process.

Thus, the excitation power in function of emission intensity was plotted for all samples and shown in Table 6. For the slope, a value of approximately 2.08 implying that two photons are involved in the energy transfers process, confirming that is an up-conversing process, since it consists in the absorption of two photons with low energy generating a higher emitted photon. All samples showed slopes with values near to two and they are presented in Table 5. The upconversion of Er^{3+} is presented in Figure 40.

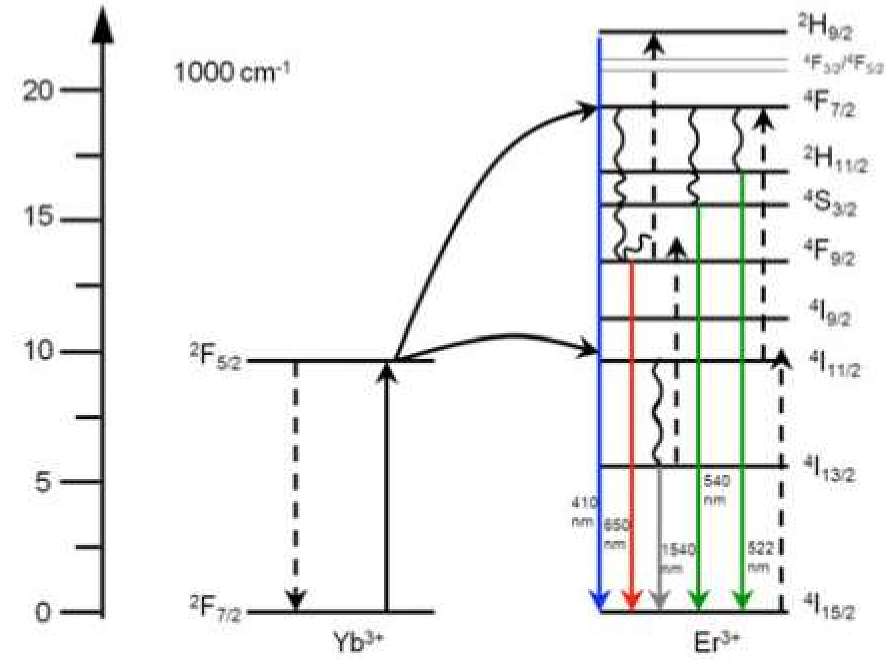

Figure 40. Erbium upconversion mechanism scheme.[167]

Table 5. Photons involved in up-conversion process for each In-based perovskite.

Samples	Slope
pIn0.9:Er5	2.05
pIn0.9:Er15	2.06
pAg0.6In:Er5	2.20
pAg0.6In:Er15	2.19
pAg0.6In0.9:Er5	2.00
pAg0.6In0.9:Er15	2.09
pIn0.9:Yb-Er	1.70
pAg0.6In:Yb-Er	1.97
pAg0.6In0.9:Yb-Er	2.07

Er and Yb-Er containing In-based perovskites were synthesized to explore erbium's characteristic emission by charge transfer process, aiming different applications for In-based perovskite, such as optical thermometry. Although, luminescent thermometry experiments were only performed for Yb/Er co-doped perovskites due to the ytterbium's larger absorption cross-section at 980 nm.

6.2.2. Ln^{3+}-doped In-based perovskite for optical thermometry

Figure 41 presents the temperature-dependent emission spectra of sample Yb^{3+}/Er^{3+}:pAg0.6In0.9 recorded varying the temperature from 173 to 473 K to evaluate its performance as a Boltzmann thermometer. The characteristic upconverting emission of Er^{3+} is observed in the green spectral region, with the emission bands corresponding to the $^2H_{11/2}\rightarrow{}^4I_{15/2}$ and $^4S_{3/2}\rightarrow{}^4I_{15/2}$ transitions peaking around 524 and 550 nm, respectively, the emission of the two thermally coupled levels $^2H_{11/2}$ (I_H) and $^4S_{3/2}$ (I_S) in different temperatures were measured. Since this is a ratiometric thermometer, the calculations were made using the integrated area of both erbium green emission.

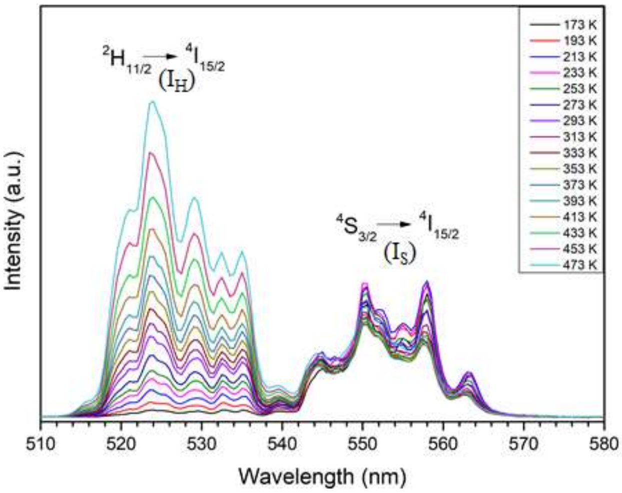

Figure 41. Ln^3+ co-doped-perovskite emission spectra in different temperatures (173 to 473 K), using a 980 nm laser with laser power density of 1000 mW.

The emission spectra presented in Figure 41 shows the temperature dependence of $^2H_{11/2}$, and $^4S_{3/2}$ transitions to the ground state $^4I_{15/2}$, in which the influence of temperature in the population of $^2H_{11/2}$ and $^4S_{3/2}$ levels is more noticeable looking at the 3D graphic. The population of the thermally coupled levels of Er^{3+} ($^2H_{11/2}$ and $^4S_{3/2}$) follows the Boltzmann distribution (Equation 15):

$$\Delta = \frac{I_H}{I_S} = B \exp\left(-\frac{\Delta E}{k_B T}\right) \quad \textbf{(15)}$$

where Δ is the thermometric parameter, also known as luminescence intensity ratio (LIR), which indicates the luminescence intensity ratio of the integrated area of the emission bands corresponding to the $^2H_{11/2} \rightarrow {}^4I_{15/2}$ (I_H), and $^4S_{3/2} \rightarrow {}^4I_{15/2}$ (I_S) transitions in this case. B is a pre-exponential factor related to the degeneracy of levels of Er^{3+}, ΔE is the energy gap between the two thermally coupled levels, k_B is the Boltzmann constant (0.695 cm^{-1} K^{-1}), and T refers to the thermodynamic temperature in Kelvin. It is worth pointing out that despite there are several works referring to Δ as fluorescence intensity ratio (FIR),[168] this is technically incorrect because the emission arising from the lanthanide ions is longer-lived than common fluorescence processes observed for organic dyes, therefore it should be referred to as luminescence. Nevertheless, it is possible to calculate the temperature from the upconverting emission spectra of sample Yb^{3+}/Er^{3+}:pAg0.6In0.9 using Equation 16 if the values of ΔE and B are known. A linear response can be obtained by applying the natural logarithm (*ln*) to Equation 15 (Equation 16):

$$\ln\Delta = \ln B - \frac{\Delta E}{k_B}\frac{1}{T} \quad (16)$$

In this sense, a plot of lnΔ *versus* T^{-1} (Boltzmann plot) allows for the determination of ΔE and B by looking at the slope (slope = $-\Delta E/k_B$) and the intercept (intercept = ln B) of the fitted curve, respectively. Suta *et al.* have recently shown that the optimum temperature range to use Er^{3+} as a Boltzmann thermometer is around room temperature.[112] For that reason, only the emission spectra of sample pAg0.6In0.9 in the temperature range between 293 and 343 K were used to determine ΔE and B. The values of I_H and I_S used for the calculation of Δ were obtained by integrating the emission spectra in the 515-540 nm and 540-570 nm range, respectively.

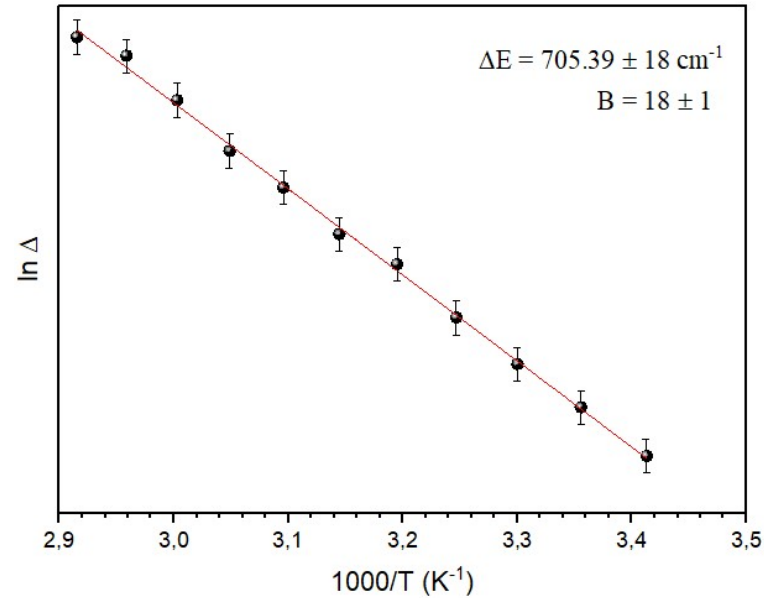

Figure 42. ln (Δ) versus T^{-1} of Yb^{3+}/Er^{3+}:pAg0.6In0.9 sample followed by the determination of ΔE and B parameters.

The calculated value for ΔE and B are 705 ± 18 cm^{-1} and 18 ± 1, respectively, in excellent agreement with those reported in the literature,[100,170,171] especially for ΔE whose theoretical value is approximately 700 cm^{-1}, this might vary just depending on the host.[112] Now, it is possible to predict the temperature by following equation 15. The final and last step is to calculate the thermometric performance of the proposed thermometer. The figures of merit used to measure the performance of a thermometer are the relative thermal sensitivity (S_r) and the uncertainty in temperature (δT), presented in equations 11 and 12, respectively. The bigger relative thermal sensitivity value the better, on the contrary, the smaller uncertainty in temperature the better. A graphic illustrating the maximum S_r and the minimum δT are shown in Figure 43 (a) and (b), respectively.

$$S_r = \frac{1}{\Delta}\left|\frac{\partial \Delta}{\partial T}\right| \quad \textbf{(11)}$$

$$\delta T = \frac{1}{S_r}\frac{\delta \Delta}{\Delta} \quad \textbf{(12)}$$

For Boltzmann thermometers, equation 12 assumes the form of equation 13,[112] indicating that the S_r of luminescent thermometers based on thermally coupled level is driven by ΔE.[112]

$$S_r = \frac{\Delta E}{k_B T^2} \quad \textbf{(13)}$$

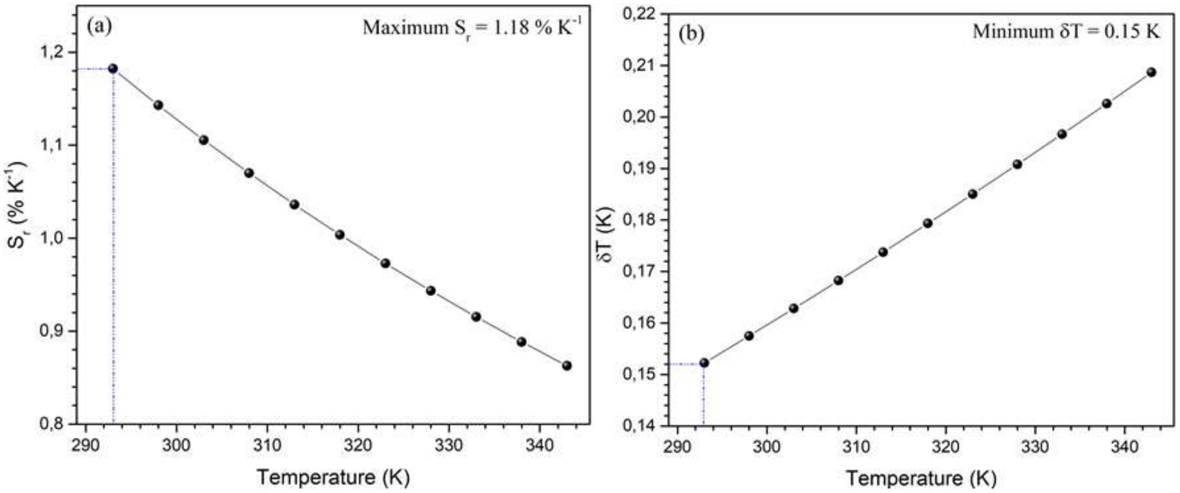

Figure 43. Comparison among calculated and measured temperature for Ln^{3+}-doped In-based perovskite.

Therefore, pAg0.6In09 co-doped with Yb^{3+}/Er^{3+} (10:5 %) exhibited a maximum S_r and a minimum δT value of 1.18 % K^{-1} and 0.15 K, respectively. The relative thermal sensitivity of the recent world record is 50 % K^{-1}, and an uncertainty in temperature record of 0.05 K.[108] These world record values for S_r and δT are assigned to Ag_2S nanoparticles,[108] however the obtained result are in good agreement with those recently presented in the literature for Er^{3+}-based thermometers.[172,173] The same procedure was used to evaluate the thermometric performance of the other obtained samples and the results of ΔE, B, S_r, and δT for all Yb^{3+}/Er^{3+} co-doped samples are summarized in Table 6. All thermometric analysis showed is from Yb^{3+}/Er^{3+} (10:5%) doped pAg0.6In0.9

Table 6. ΔE, B, S_r and δT value of all Yb^{3+}/Er^{3+}-co-doped In-based perovskites matrixes.

Sample	T_{max} (K)	ΔE (cm^{-1})	S_r (% K^{-1})	δT (K)	Reference
pIn0.9	293	706 ±52	1.18	0.15	This work
pAg0.6In	293	664 ±2	1.11	0.16	This work
pAg0.6In0.9	293	705 ±18	1.18	0.15	This work
Films of Yb^{3+}/Er^{3+}-codoped GeO_2-Ta_2O_5	300	688	1.1	0.7	[171]
Yb^{3+}/Er^{3+}:YAG	293	489	0.82	0.21	[169]
Yb^{3+}/Er^{3+}:Al_2O_3	495	868	0.51	0.3	[174]

It was observed that pIn0.9 and pAg0.6In0.9 presented an overall better performance since their S_r is higher and δT is lower than the ones obtained for the pAg0.6In sample. Despite that, they presented a close value compared to each other and, a S_r and δT value in accordance with those presented in the literature for luminescent thermometers based on Er^{3+}. In comparison with other works, all codoped In-based perovskite synthesized showed a better performance, highlighting these In-based perovskite a promising material for optical thermometry applications.

Finally, to understand and study the data reproducibility and reliability for the developed Boltzmann thermometers it was performed an analysis varying the temperature from 273 to 373 K 10 times (10 cycles). Figure 44 exhibits an example of reproducibility analysis for pAg0.6In0.9 sample.

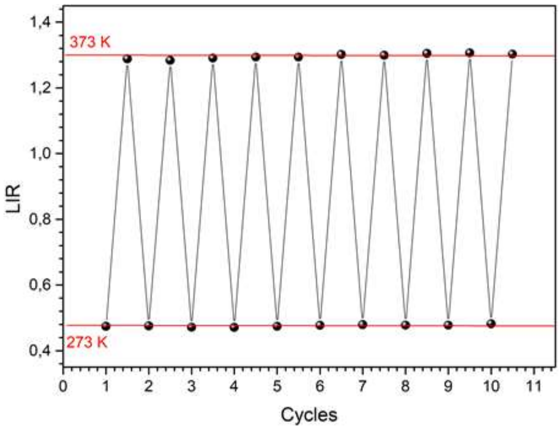

Figure 44. Reproducibility and reliability of Yb^{3+}/Er^{3+}:pAg0.6In0.9 sample as a luminescent thermometer.

Analyzing the result presented in Figure 44, it is noticeable the minimal variation of temperature between each cycle, implying in a thermometer with reproducible and reliable data.

7. Conclusion

All proposed samples were synthesized, and their formation was confirmed by XRD and Raman spectroscopy. X-ray diffraction showed that the samples exhibited high crystalline cubic phase with *Fm3m* space group. Raman spectroscopy could corroborate with the perovskites structural characterization by showing its characteristic vibrational modes also perfectly matching with the corresponding standard sample. Scanning electron microscopy (SEM) gave a general idea of perovskite morphology, size, and distribution when as a powder. The Bi-based perovskite used for photocatalysis purposes showed a promising photocatalytic activity for almost all samples, besides they proportioned the understanding the role and importance of Ag content in photocatalysis, Ag correlation in kinetics and on bandgap values. The Ag1.0 sample, exhibited the best kinetics while the Ag0.0 sample showed the worst kinetics. From Ag1.0 to Ag0.2, in other words, from the highest Ag sample concentration to the lowest Ag concentration, the kinetics decreases almost 2 times while from Ag1.0 to Ag0.0 decreased a bit more than 11 times. All samples containing Ag content were able to achieve complete degradation of crystal violet dye within 60 min, while Ag0.0 reached 95% of CV degradation in 90 min. Not only, Ag content exhibited a significant influence on perovskites bandgap. However, a deep investigation on perovskites structural stability after photocatalysis experiment is required. XRD for Bi-based perovskite samples after photocatalysis showed that perovskite might not be stable in aqueous solution and/or under light irradiation. The In-based perovskites doped with lanthanide exhibited Ln^{3+} characteristic emission in both NIR and visible range, one by direct radiative decay and other by up-conversion process, respectively. The characteristic transition of Er^{3+} and Yb^{3+} contributed to assure the doping of these samples. All samples demonstrated to present up-conversion energy transfer process by emitting at the green and red region with erbium's characteristic emission. Using the two thermally coupled levels of Er^{3+} ($^2H_{11/2}$ and $^4S_{3/2}$) it was possible to develop a new Ln^{3+}-based luminescent thermometer. The sample which displayed the best thermometric performance, Yb^{3+}/Er^{3+}:pAg0.6In0.9, exhibited a relative thermal sensitivity (S_r) of 1.18 % K^{-1}, and uncertainty in temperature (δT) of 0.15 K^{-1}. Both these values are in great agreement with those presented in recent works for Er^{3+}-based thermometers. Furthermore, all samples showed a great repeatability, reproducibility and reliable data.

This master's dissertation contributed for both photocatalysis and optical thermometry field. In photocatalysis, it was possible to evaluate the influence of halide (Cl^- and Br^-) and Ag content in perovskite photocatalytic performance. There are just a few works reporting Bi-based perovskite photocatalysis, being a new and significant contribution for this field. Into the optical thermometry field, it was reported the first Er^{3+}-based thermometer using In-based perovskite as host. There is also few works reporting Ln^{3+}-doped In-based perovskite in the literature, so this dissertation contributed to a new application for this type of material until now.

Ideas for future works

- Develop a perovskite-TiO_2 heterojunction system to enhance TiO_2 photocatalytic performance since TiO_2 have a poor light absorption in the visible region.

- Synthesis of $Cs_2AgIn_xBi_{1-x}Cl_6$ perovskites for photocatalytic experiments in order to evaluate the influence of the bandgap nature, e.g., compare the photocatalytic performance for direct and indirect bandgap.

- Synthesis of colloidal nanoparticles of In-based perovskites, scoping its incorporation into a polyurethane matrix. Despite the higher stability conferred by PU matrix, the aim of the perovskite/polyurethane composite is to achieve white light emission.

- Synthesis of colloidal nanoparticles of Ln^{3+}-doped In-based perovskites for luminescent thermometry purposes are an interesting option either.

References

1. Quan, L. N. *et al.* Perovskites for Next-Generation Optical Sources. *Chemical Reviews* vol. 119 7444–7477 (2019).

2. Saliba, M. *et al.* Cesium-containing triple cation perovskite solar cells: Improved stability, reproducibility and high efficiency. *Energy and Environmental Science* vol. 9 1989–1997 (2016).

3. Dave, K., Fang, M. H., Bao, Z., Fu, H. T. & Liu, R. S. Recent Developments in Lead-Free Double Perovskites: Structure, Doping, and Applications. *Chemistry - An Asian Journal* vol. 15 242–252 (2020).

4. Tan, Z.-K. *et al.* Bright light-emitting diodes based on organometal halide perovskite. *Nature Nanotechnology* vol. 9 687–692 (2014).

5. Palazon, F. *et al.* Polymer-Free Films of Inorganic Halide Perovskite Nanocrystals as UV-to-White Color-Conversion Layers in LEDs. *Chemistry of Materials* vol. 28 2902–2906 (2016).

6. Zhu, H. *et al.* Lead halide perovskite nanowire lasers with low lasing thresholds and high quality factors. *Nature Materials* vol. 14 636–642 (2015).

7. Xing, G. *et al.* Low-temperature solution-processed wavelength-tunable perovskites for lasing. *Nature Materials* vol. 13 476–480 (2014).

8. Bao, C. *et al.* High Performance and Stable All-Inorganic Metal Halide Perovskite-Based Photodetectors for Optical Communication Applications. *Advanced Materials* vol. 30 1–8 (2018).

9. Dong, R. *et al.* High-Gain and Low-Driving-Voltage Photodetectors Based on Organolead Triiodide Perovskites. *Advanced Materials* vol. 27 1912–1918 (2015).

10. Ou, M. *et al.* Amino-Assisted Anchoring of CsPbBr 3 Perovskite Quantum Dots on Porous g-C 3 N 4 for Enhanced Photocatalytic CO 2 Reduction. *Angewandte Chemie* vol. 130 13570–13574 (2018).

11. Yang, W. S. *et al.* Iodide management in formamidinium-lead-halide-based perovskite layers for efficient solar cells. *Science* vol. 356 1376–1379 (2017).

12. Albrecht, S. *et al.* Monolithic perovskite/silicon-heterojunction tandem solar cells processed at low temperature. *Energy & Environmental Science* vol. 9 81–88 (2016).

13. Igbari, F., Wang, Z. K. & Liao, L. S. Progress of Lead-Free Halide Double Perovskites. *Advanced Energy Materials* vol. 9 (2019).

14. Filip, M. R., Hillman, S., Haghighirad, A. A., Snaith, H. J. & Giustino, F. Band Gaps of the Lead-Free Halide Double Perovskites Cs2BiAgCl6 and Cs2BiAgBr6 from Theory and Experiment. *Journal of Physical Chemistry Letters* vol. 7 2579–2585 (2016).

15. Wang, T., Yue, D., Li, X. & Zhao, Y. Lead-free double perovskite Cs2AgBiBr6/RGO composite for efficient visible light photocatalytic H2 evolution. *Appl. Catal. B*

Environ. **268**, 118399 (2020).

16. Zhang, Z. *et al.* Stable and Highly Efficient Photocatalysis with Lead-Free Double-Perovskite of Cs 2 AgBiBr 6. *Angewandte Chemie International Edition* vol. 58 7263–7267 (2019).

17. Zhou, L., Xu, Y. F., Chen, B. X., Kuang, D. Bin & Su, C. Y. Synthesis and Photocatalytic Application of Stable Lead-Free Cs2AgBiBr6 Perovskite Nanocrystals. *Small* vol. 14 1–7 (2018).

18. Volonakis, G. *et al.* Cs2InAgCl6: A New Lead-Free Halide Double Perovskite with Direct Band Gap. *Journal of Physical Chemistry Letters* vol. 8 772–778 (2017).

19. Liu, Y. *et al.* Incorporating Rare-Earth Terbium(III) Ions into Cs 2 AgInCl 6 :Bi Nanocrystals toward Tunable Photoluminescence. *Angew. Chemie Int. Ed.* **59**, 11634–11640 (2020).

20. Li, S. *et al.* Self-Trapped Exciton to Dopant Energy Transfer in Rare Earth Doped Lead-Free Double Perovskite. *Advanced Optical Materials* vol. 7 1901098 (2019).

21. Lee, W., Hong, S. & Kim, S. Colloidal Synthesis of Lead-Free Silver–Indium Double-Perovskite Cs 2 AgInCl 6 Nanocrystals and Their Doping with Lanthanide Ions. *The Journal of Physical Chemistry C* vol. 123 2665–2672 (2019).

22. Brites, C. D. S., Millán, A. & Carlos, L. D. Lanthanides in Luminescent Thermometry. in *Handbook on the Physics and Chemistry of Rare Earths* (ed. Jean-Claude Bünzli, V. K. P.) 339–427 (Elsevier, 2016). doi:10.1016/bs.hpcre.2016.03.005.

23. Bhalla, A. S., Guo, R. & Roy, R. The perovskite structure - A review of its role in ceramic science and technology. *Materials Research Innovations* vol. 4 3–26 (2000).

24. Assirey, E. A. R. Perovskite synthesis, properties and their related biochemical and industrial application. *Saudi Pharmaceutical Journal* vol. 27 817–829 (2019).

25. Knittle, E. & Jeanloz, R. Synthesis and equation of state of (Mg,Fe)SiO3 perovskite to over 100 gigapascals. *Science* vol. 235 668–670 (1987).

26. Cheng, Z. & Lin, J. Layered organic-inorganic hybrid perovskites: Structure, optical properties, film preparation, patterning and templating engineering. *CrystEngComm* vol. 12 2646–2662 (2010).

27. Hoefler, S. F., Trimmel, G. & Rath, T. Progress on lead-free metal halide perovskites for photovoltaic applications: a review. *Monatshefte für Chemie - Chemical Monthly* vol. 148 795–826 (2017).

28. Goldschmidt, V. M. Die Gesetze der Krystallochemie. *Naturwissenschaften* **14**, 477–485 (1926).

29. Bartel, C. J. *et al.* New tolerance factor to predict the stability of perovskite oxides and halides. *Science Advances* vol. 5 1–10 (2019).

30. Li, C. *et al.* Formability of ABX 3 (X = F, Cl, Br, I) halide perovskites. *Acta Crystallographica Section B: Structural Science* vol. 64 702–707 (2008).

31. Li, W. *et al.* Chemically diverse and multifunctional hybrid organic-inorganic perovskites. *Nature Reviews Materials* vol. 2 (2017).

32. Kim, Y. G. *et al.* Atomically thin two-dimensional materials as hole extraction layers in organolead halide perovskite photovoltaic cells. *Journal of Power Sources* vol. 319 1–8 (2016).

33. Park, N. G. Perovskite solar cells: An emerging photovoltaic technology. *Materials Today* vol. 18 65–72 (2015).

34. Veldhuis, S. A. *et al.* Perovskite Materials for Light-Emitting Diodes and Lasers. *Advanced Materials* vol. 28 6804–6834 (2016).

35. Le, Q. Van, Kim, J. B., Kim, S. Y., Lee, B. & Lee, D. R. Structural Investigation of Cesium Lead Halide Perovskites for High-Efficiency Quantum Dot Light-Emitting Diodes. *Journal of Physical Chemistry Letters* vol. 8 4140–4147 (2017).

36. Ahmadi, M., Wu, T. & Hu, B. A Review on Organic–Inorganic Halide Perovskite Photodetectors: Device Engineering and Fundamental Physics. *Advanced Materials* vol. 29 1605242 (2017).

37. Le, Q. Van, Hong, K., Jang, H. W. & Kim, S. Y. Halide Perovskite Quantum Dots for Light-Emitting Diodes: Properties, Synthesis, Applications, and Outlooks. *Advanced Electronic Materials* vol. 4 1–28 (2018).

38. Huang, H. *et al.* Colloidal lead halide perovskite nanocrystals: synthesis, optical properties and applications. *NPG Asia Materials* vol. 8 e328–e328 (2016).

39. Protesescu, L. *et al.* Nanocrystals of Cesium Lead Halide Perovskites (CsPbX3, X = Cl, Br, and I): Novel Optoelectronic Materials Showing Bright Emission with Wide Color Gamut. *Nano Letters* vol. 15 3692–3696 (2015).

40. Song, Z., Zhao, J. & Liu, Q. Luminescent perovskites: Recent advances in theory and experiments. *Inorganic Chemistry Frontiers* vol. 6 2969–3011 (2019).

41. Borriello, I., Cantele, G. & Ninno, D. Ab initio investigation of hybrid organic-inorganic perovskites based on tin halides. *Physical Review B - Condensed Matter and Materials Physics* vol. 77 1–9 (2008).

42. Filippetti, A. & Mattoni, A. Hybrid perovskites for photovoltaics: Insights from first principles. *Physical Review B - Condensed Matter and Materials Physics* vol. 89 1–8 (2014).

43. Bergman, Leah McHale, J. L. *Handbook of Luminescent Semiconductor Materials*. (CRC Press, 2016). doi:10.1201/b11201.

44. Mizoguchi, H., Eng, H. W. & Woodward, P. M. Probing the Electronic Structures of Ternary Perovskite and Pyrochlore Oxides Containing Sn4+ or Sb5+. *Inorganic Chemistry* vol. 43 1667–1680 (2004).

45. D'Innocenzo, V. *et al.* Tuning the light emission properties by band gap engineering in hybrid lead halide perovskite. *Journal of the American Chemical Society* vol. 136 17730–17733 (2014).

46. Kong, Y., Song, Z., Wang, S., Xia, Z. & Liu, Q. The Inductive Effect in Nitridosilicates and Oxysilicates and Its Effects on 5d Energy Levels of Ce3+. *Inorganic Chemistry* vol. 57 2320–2331 (2018).

47. Babayigit, A., Ethirajan, A., Muller, M. & Conings, B. Toxicity of organometal halide perovskite solar cells. *Nature Materials* vol. 15 247–251 (2016).

48. Babayigit, A. *et al.* Assessing the toxicity of Pb- and Sn-based perovskite solar cells in model organism Danio rerio. *Scientific Reports* vol. 6 18721 (2016).

49. Hauptman, M., Bruccoleri, R. & Woolf, A. D. An Update on Childhood Lead Poisoning. *Clinical Pediatric Emergency Medicine* vol. 18 181–192 (2017).

50. Hu, H., Dong, B. & Zhang, W. Low-toxic metal halide perovskites: Opportunities and future challenges. *Journal of Materials Chemistry A* vol. 5 11436–11449 (2017).

51. Conings, B. *et al.* Intrinsic Thermal Instability of Methylammonium Lead Trihalide Perovskite. *Advanced Energy Materials* vol. 5 1500477 (2015).

52. Stoumpos, C. C., Malliakas, C. D. & Kanatzidis, M. G. Semiconducting Tin and Lead Iodide Perovskites with Organic Cations: Phase Transitions, High Mobilities, and Near-Infrared Photoluminescent Properties. *Inorganic Chemistry* vol. 52 9019–9038 (2013).

53. Mitzi, D. B. Organic−Inorganic Perovskites Containing Trivalent Metal Halide Layers: The Templating Influence of the Organic Cation Layer. *Inorganic Chemistry* vol. 39 6107–6113 (2000).

54. McClure, E. T., Ball, M. R., Windl, W. & Woodward, P. M. Cs2AgBiX6 (X = Br, Cl): New Visible Light Absorbing, Lead-Free Halide Perovskite Semiconductors. *Chemistry of Materials* vol. 28 1348–1354 (2016).

55. Shum, K. *et al.* Synthesis and characterization of CsSnI3 thin films. *Applied Physics Letters* vol. 96 2010–2013 (2010).

56. Chung, I. *et al.* CsSnI 3: Semiconductor or metal? High electrical conductivity and strong near-infrared photoluminescence from a single material. High hole mobility and phase-transitions. *Journal of the American Chemical Society* vol. 134 8579–8587 (2012).

57. Chen, Z. *et al.* Photoluminescence study of polycrystalline CsSnI3 thin films: Determination of exciton binding energy. *Journal of Luminescence* vol. 132 345–349 (2012).

58. Volonakis, G. *et al.* Lead-Free Halide Double Perovskites via Heterovalent Substitution of Noble Metals. *Journal of Physical Chemistry Letters* vol. 7 1254–1259 (2016).

59. Vasala, S. & Karppinen, M. A2B′B″O6 perovskites: A review. *Progress in Solid State Chemistry* vol. 43 1–36 (2015).

60. Filip, M. R., Hillman, S., Haghighirad, A. A., Snaith, H. J. & Giustino, F. Band Gaps of the Lead-Free Halide Double Perovskites Cs 2 BiAgCl 6 and Cs 2 BiAgBr 6 from

Theory and Experiment. *The Journal of Physical Chemistry Letters* vol. 7 2579–2585 (2016).

61. Saparov, B. & Mitzi, D. B. Organic-Inorganic Perovskites: Structural Versatility for Functional Materials Design. *Chemical Reviews* vol. 116 4558–4596 (2016).

62. Shannon, R. D. Revised effective ionic radii and systematic studies of interatomic distances in halides and chalcogenides. *Acta Crystallographica Section A* vol. 32 751–767 (1976).

63. Allen, L. C. Electronegativity Is the Average One-Electron Energy of the Valence-Shell Electrons in Ground-State Free Atoms. *Journal of the American Chemical Society* vol. 111 9003–9014 (1989).

64. Slavney, A. H., Hu, T., Lindenberg, A. M. & Karunadasa, H. I. A Bismuth-Halide Double Perovskite with Long Carrier Recombination Lifetime for Photovoltaic Applications. *Journal of the American Chemical Society* vol. 138 2138–2141 (2016).

65. Baccaro, A. & Gutz, I. FOTOELETROCATÁLISE EM SEMICONDUTORES: DOS PRINCÍPIOS BÁSICOS ATÉ SUA CONFORMAÇÃO À NANOESCALA. *Química Nova* vol. 41 326–339 (2017).

66. Yang, B. *et al.* Lead-Free Direct Band Gap Double-Perovskite Nanocrystals with Bright Dual-Color Emission. *Journal of the American Chemical Society* vol. 140 17001–17006 (2018).

67. Liu, Y., Nag, A., Manna, L. & Xia, Z. Lead-Free Double Perovskite Cs2AgInCl6. *Angewandte Chemie - International Edition* (2020) doi:10.1002/anie.202011833.

68. Luo, J. *et al.* Efficient and stable emission of warm-white light from lead-free halide double perovskites. *Nature* vol. 563 541–545 (2018).

69. Reddy, P. A. K. *et al.* Recent advances in photocatalytic treatment of pollutants in aqueous media. *Environment International* vol. 91 94–103 (2016).

70. Chen, C., Ma, W. & Zhao, J. Semiconductor-mediated photodegradation of pollutants under visible-light irradiation. *Chemical Society Reviews* vol. 39 4206–4219 (2010).

71. Byrne, C., Subramanian, G. & Pillai, S. C. Recent advances in photocatalysis for environmental applications. *Journal of Environmental Chemical Engineering* vol. 6 3531–3555 (2018).

72. Ohtani, B. Photocatalysis A to Z-What we know and what we do not know in a scientific sense. *Journal of Photochemistry and Photobiology C: Photochemistry Reviews* vol. 11 157–178 (2010).

73. Ohtani, B. Revisiting the fundamental physical chemistry in heterogeneous photocatalysis: Its thermodynamics and kinetics. *Physical Chemistry Chemical Physics* vol. 16 1788–1797 (2014).

74. Pelaez, M. *et al.* A review on the visible light active titanium dioxide photocatalysts for environmental applications. *Applied Catalysis B: Environmental* vol. 125 331–349 (2012).

75. Hamilton, J. W. J. *et al.* Evaluating the mechanism of visible light activity for N,F-TiO2 using photoelectrochemistry. *Journal of Physical Chemistry C* vol. 118 12206–12215 (2014).

76. De Sousa Filho, P. C., Lima, J. F. & Serra, O. A. From lighting to photoprotection: Fundamentals and applications of rare earth materials. *Journal of the Brazilian Chemical Society* vol. 26 2471–2495 (2015).

77. IUPAC. Compendium of Chemical Terminology. in *Compendium of Chemical Terminology, 2nd ed. (the 'Gold Book'). Compiled by A. D. McNaught and A. Wilkinson. Blackwell Scientific Publications, Oxford (1997). Online version (2019-) created by S. J. Chalk.* (IUPAC). doi:10.1351/goldbook.L03641.

78. Murthy, K. V. R. & Virk, H. S. Luminescence phenomena: An introduction. *Defect and Diffusion Forum* vol. 347 1–34 (2014).

79. Valeur, B. & Berberan-Santos, M. N. A Brief History of Fluorescence and Phosphorescence before the Emergence of Quantum Theory. *Journal of Chemical Education* vol. 88 731–738 (2011).

80. Feldmann, C., Jüstel, T., Ronda, C. R. & Schmidt, P. J. Inorganic luminescent materials: 100 Years of research and application. *Advanced Functional Materials* vol. 13 511–516 (2003).

81. Virk, H. S. History of Luminescence from Ancient to Modern Times. *Defect and Diffusion Forum* vol. 361 1–13 (2015).

82. Jain, A., Sengar, P. & Hirata, G. A. Rare-earth-doped Y 3 Al 5 O 12 (YAG) nanophosphors: synthesis, surface functionalization, and applications in thermoluminescence dosimetry and nanomedicine. *Journal of Physics D: Applied Physics* vol. 51 303002 (2018).

83. Šípoš, R. & Šima, J. Jablonski diagram revisited. *Revista Cubana de Fisica* vol. 37 125–130 (2020).

84. Atkins, P.w. - De Paula, J. *Físico-química - Vol. 1*. (Editora LTC, 2008).

85. Khalid, A. & Kontis, K. Thermographic Phosphors for High Temperature Measurements: Principles, Current State of the Art and Recent Applications. *Sensors* vol. 8 5673–5744 (2008).

86. Allison, S. W. & Gillies, G. T. Remote thermometry with thermographic phosphors: Instrumentation and applications. *Review of Scientific Instruments* vol. 68 2615–2650 (1997).

87. Sousa Filho, P. C. de & Serra, O. A. RARE EARTHS IN BRAZIL: HISTORICAL ASPECTS, PRODUCTION, AND PERSPECTIVES. *Química Nova* vol. 37 1–4 (2014).

88. Sousa Filho, P. C. de. Estudos sobre síntese, propriedades estruturais e espectroscópicas de oxossais de terras raras para aplicações como luminóforos de ultravioleta de vácuo. (Universidade de São Paulo, 2013). doi:10.11606/T.59.2013.tde-

25072013-095144.

89. Martins, T. S. & Isolani, P. C. Terras raras: Aplicações industriais e biológicas. *Quimica Nova* vol. 28 111–117 (2005).

90. Malta, O. L. & Carlos, L. D. Intensities of 4f-4f transitions in glass materials. *Química Nova* vol. 26 889–895 (2003).

91. Goodwin, D. W. Spectra and Energy Levels of Rare Earth Ions in Crystals. *Physics Bulletin* vol. 20 525–525 (1969).

92. Auzel, F. Upconversion and Anti-Stokes Processes with f and d Ions in Solids. *Chemical Reviews* vol. 104 139–174 (2004).

93. Lian, H. *et al.* Rare earth ions doped phosphors for improving efficiencies of solar cells. *Energy* vol. 57 270–283 (2013).

94. Zhang, Q. Y. & Huang, X. Y. Recent progress in quantum cutting phosphors. *Progress in Materials Science* vol. 55 353–427 (2010).

95. Trupke, T., Green, M. A. & Würfel, P. Improving solar cell efficiencies by down-conversion of high-energy photons. *Journal of Applied Physics* vol. 92 1668–1674 (2002).

96. Wang, F. & Liu, X. Recent advances in the chemistry of lanthanide-doped upconversion nanocrystals. *Chemical Society Reviews* vol. 38 976 (2009).

97. Auzel, F. Compteur quantique par transfert d'energie entre deux ions de terres rares dans un tungstate mixte et dans un verre. *Comptes rendus de l'Académie des Sciences* vol. 262 1016–1019 (1966).

98. Ovsyankin, V. V. ; Feofilov, P. P. Mechanism of Summation of Electronic Excitations in Activated Crystals. *Journal of Experimental and Theoretical Physics Letters* vol. 3 322 (1966).

99. Auzel, F. Upconversion processes in coupled ion systems. *Journal of Luminescence* vol. 45 341–345 (1990).

100. Balabhadra, S., Debasu, M. L., Brites, C. D. S., Ferreira, R. A. S. & Carlos, L. D. Upconverting Nanoparticles Working As Primary Thermometers In Different Media. *The Journal of Physical Chemistry C* vol. 121 13962–13968 (2017).

101. Wang, W. *et al.* Growth, spectroscopic properties and up-conversion of Yb, Pr co-doped CaF2 crystals. *J. Lumin.* **233**, 117931 (2021).

102. Cao, B. *et al.* Wide-range and highly-sensitive optical thermometers based on the temperature-dependent energy transfer from Er to Nd in Er/Yb/Nd codoped NaYF4 upconversion nanocrystals. *Chem. Eng. J.* **385**, 123906 (2020).

103. Liu, N., Qin, W., Qin, G., Jiang, T. & Zhao, D. Highly plasmon-enhanced upconversion emissions from Au@β-NaYF4:Yb,Tm hybrid nanostructures. *Chem. Commun.* **47**, 7671 (2011).

104. Scheps, R. Upconversion laser processes. *Progress in Quantum Electronics* vol. 20 271–358 (1996).

105. Li, D., Yu, S.-H. & Jiang, H.-L. From UV to Near-Infrared Light-Responsive Metal-Organic Framework Composites: Plasmon and Upconversion Enhanced Photocatalysis. *Advanced Materials* vol. 30 1707377 (2018).

106. Sun, L., Wei, R., Feng, J. & Zhang, H. Tailored lanthanide-doped upconversion nanoparticles and their promising bioapplication prospects. *Coordination Chemistry Reviews* vol. 364 10–32 (2018).

107. Chen, C., Li, C. & Shi, Z. Current Advances in Lanthanide-Doped Upconversion Nanostructures for Detection and Bioapplication. *Advanced Science* vol. 3 1600029 (2016).

108. Maturi, F. E. *et al.* Going Above and Beyond: A Tenfold Gain in the Performance of Luminescence Thermometers Joining Multiparametric Sensing and Multiple Regression. *Laser and Photonics Reviews* vol. 15 1–10 (2021).

109. Brites, C. D. S., Balabhadra, S. & Carlos, L. D. Lanthanide-Based Thermometers: At the Cutting-Edge of Luminescence Thermometry. *Advanced Optical Materials* vol. 7 1–30 (2019).

110. Brites, C. D. S. *et al.* Thermometry at the nanoscale. *Nanoscale* vol. 4 4799–4829 (2012).

111. MARTIN, G. A Definition of Temperature. *Nature* vol. 73 390–390 (1906).

112. Suta, M. & Meijerink, A. A Theoretical Framework for Ratiometric Single Ion Luminescent Thermometers—Thermodynamic and Kinetic Guidelines for Optimized Performance. *Advanced Theory and Simulations* vol. 3 1–32 (2020).

113. Childs, P. R. N., Greenwood, J. R. & Long, C. A. Review of temperature measurement. *Review of Scientific Instruments* vol. 71 2959–2978 (2000).

114. Wolfbeis, O. S. Sensor Paints. *Advanced Materials* vol. 20 3759–3763 (2008).

115. McCabe, K. M. & Hernandez, M. Molecular Thermometry. *Pediatric Research* vol. 67 469–475 (2010).

116. Jaque, D. *et al.* Nanoparticles for photothermal therapies. *Nanoscale* vol. 6 9494–9530 (2014).

117. Bünzli, J.-C. G. Lanthanide Luminescence: From a Mystery to Rationalization, Understanding, and Applications. in *Handbook on the Physics and Chemistry of Rare Earths* 141–176 (Elsevier, 2016). doi:10.1016/bs.hpcre.2016.08.003.

118. Uchiyama, S., Gota, C., Tsuji, T. & Inada, N. Intracellular temperature measurements with fluorescent polymeric thermometers. *Chemical Communications* vol. 53 10976–10992 (2017).

119. Jaque, D. & Vetrone, F. Luminescence nanothermometry. *Nanoscale* vol. 4 4301 (2012).

120. Kim, S. H. *et al.* Micro-Raman thermometry for measuring the temperature distribution inside the microchannel of a polymerase chain reaction chip. *Journal of Micromechanics and Microengineering* vol. 16 526–530 (2006).

121. Sodnik, Z. & Tiziani, H. J. Nondestructive Evaluation of Solids by Photothermal Interferometry on Nonreflective Surfaces. in *Photoacoustic and Photothermal Phenomena* 400–403 (1988). doi:10.1007/978-3-540-48181-2_105.

122. Teyssieux, D., Thiery, L. & Cretin, B. Near-infrared thermography using a charge-coupled device camera: Application to microsystems. *Review of Scientific Instruments* vol. 78 034902 (2007).

123. Christofferson, J. & Shakouri, A. Thermoreflectance based thermal microscope. *Review of Scientific Instruments* vol. 76 024903 (2005).

124. Marciniak, L., Bednarkiewicz, A. & Elzbieciak, K. NIR–NIR photon avalanche based luminescent thermometry with Nd 3+ doped nanoparticles. *Journal of Materials Chemistry C* vol. 6 7568–7575 (2018).

125. Martins, J. C. *et al.* Primary Luminescent Nanothermometers for Temperature Measurements Reliability Assessment. *Advanced Photonics Research* vol. 2 2000169 (2021).

126. Wang, X., Wolfbeis, O. S. & Meier, R. J. Luminescent probes and sensors for temperature. *Chemical Society Reviews* vol. 42 7834 (2013).

127. PAVIOLO, C., CLAYTON, A. H. A., MCARTHUR, S. L. & STODDART, P. R. Temperature measurement in the microscopic regime: a comparison between fluorescence lifetime- and intensity-based methods. *Journal of Microscopy* vol. 250 179–188 (2013).

128. Donner, J. S., Thompson, S. A., Kreuzer, M. P., Baffou, G. & Quidant, R. Mapping Intracellular Temperature Using Green Fluorescent Protein. *Nano Letters* vol. 12 2107–2111 (2012).

129. Okabe, K. *et al.* Intracellular temperature mapping with a fluorescent polymeric thermometer and fluorescence lifetime imaging microscopy. *Nature Communications* vol. 3 705 (2012).

130. Back, M., Trave, E., Ueda, J. & Tanabe, S. Ratiometric Optical Thermometer Based on Dual Near-Infrared Emission in Cr 3+ -Doped Bismuth-Based Gallate Host. *Chemistry of Materials* vol. 28 8347–8356 (2016).

131. Kalytchuk, S., Zhovtiuk, O., Kershaw, S. V., Zbořil, R. & Rogach, A. L. Temperature-Dependent Exciton and Trap-Related Photoluminescence of CdTe Quantum Dots Embedded in a NaCl Matrix: Implication in Thermometry. *Small* vol. 12 466–476 (2016).

132. Miyagawa, T. *et al.* Glue-Free Stacked Luminescent Nanosheets Enable High-Resolution Ratiometric Temperature Mapping in Living Small Animals. *ACS Applied Materials & Interfaces* vol. 8 33377–33385 (2016).

133. Yu, S., Tu, D., Lian, W., Xu, J. & Chen, X. Lanthanide-doped near-infrared II luminescent nanoprobes for bioapplications. *Science China Materials* vol. 62 1071–1086 (2019).

134. Shen, Y. *et al.* Perspectives for Ag 2 S NIR-II nanoparticles in biomedicine: from imaging to multifunctionality. *Nanoscale* vol. 11 19251–19264 (2019).

135. Rocha, J., Brites, C. D. S. & Carlos, L. D. Lanthanide Organic Framework Luminescent Thermometers. *Chemistry - A European Journal* vol. 22 14782–14795 (2016).

136. Brites, C. D. S. *et al.* Ratiometric highly sensitive luminescent nanothermometers working in the room temperature range. Applications to heat propagation in nanofluids. *Nanoscale* vol. 5 7572 (2013).

137. Uchiyama, S., Prasanna de Silva, A. & Iwai, K. Luminescent Molecular Thermometers. *Journal of Chemical Education* vol. 83 720 (2006).

138. Cerón, E. N. *et al.* Hybrid Nanostructures for High-Sensitivity Luminescence Nanothermometry in the Second Biological Window. *Advanced Materials* vol. 27 4781–4787 (2015).

139. Marciniak, Ł. *et al.* Near infrared absorbing near infrared emitting highly-sensitive luminescent nanothermometer based on Nd 3+ to Yb 3+ energy transfer. *Physical Chemistry Chemical Physics* vol. 17 24315–24321 (2015).

140. Liang, Z., Qin, F., Zheng, Y., Zhang, Z. & Cao, W. Noncontact thermometry based on downconversion luminescence from Eu 3+ doped LiNbO 3 single crystal. *Sensors and Actuators A: Physical* vol. 238 215–219 (2016).

141. Savchuk, O. A. *et al.* Er:Yb:NaY 2 F 5 O up-converting nanoparticles for sub-tissue fluorescence lifetime thermal sensing. *Nanoscale* vol. 6 9727 (2014).

142. Brites, C. D. S. *et al.* Widening the Temperature Range of Luminescent Thermometers through the Intra- and Interconfigurational Transitions of Pr 3+. *Advanced Optical Materials* vol. 6 1701318 (2018).

143. Kolesnikov, I. E. *et al.* YVO4:Nd3+ nanophosphors as NIR-to-NIR thermal sensors in wide temperature range. *Scientific Reports* vol. 7 18002 (2017).

144. Geitenbeek, R. G., de Wijn, H. W. & Meijerink, A. Non-Boltzmann Luminescence in NaYF4:Eu3+: Implications for Luminescence Thermometry. *Physical Review Applied* vol. 10 064006 (2018).

145. Swieten, T. P. *et al.* A Ho 3+ -Based Luminescent Thermometer for Sensitive Sensing over a Wide Temperature Range. *Advanced Optical Materials* vol. 9 2001518 (2021).

146. Dong, N.-N. *et al.* NIR-to-NIR Two-Photon Excited CaF 2 :Tm 3+ ,Yb 3+ Nanoparticles: Multifunctional Nanoprobes for Highly Penetrating Fluorescence Bio-Imaging. *ACS Nano* vol. 5 8665–8671 (2011).

147. Pickel, A. D. *et al.* Apparent self-heating of individual upconverting nanoparticle thermometers. *Nature Communications* vol. 9 4907 (2018).

148. Rühl, P. *et al.* Notes on thermometric artefacts by Er3+ luminescence band interference. *Journal of Luminescence* vol. 232 117860 (2021).

149. Ryu, J. *et al.* Facile Synthesis of Ultrasmall and Hexagonal NaGdF 4 : Yb 3+ , Er 3+ Nanoparticles with Magnetic and Upconversion Imaging Properties. *The Journal of Physical Chemistry C* vol. 114 21077–21082 (2010).

150. Roh, J., Yu, H. & Jang, J. Hexagonal β-NaYF 4 :Yb 3+ , Er 3+ Nanoprism-Incorporated Upconverting Layer in Perovskite Solar Cells for Near-Infrared Sunlight Harvesting. *ACS Applied Materials & Interfaces* vol. 8 19847–19852 (2016).

151. Kumar Chini, M. *et al.* Lead-free, stable mixed halide double perovskites Cs2AgBiBr6 and Cs2AgBiBr6−xClx – A detailed theoretical and experimental study. *Chemical Physics* vol. 529 (2020).

152. Zhang, G. *et al.* Facile solution synthesis of Bi 3+ /Yb 3+ ions co-doped Cs 2 Na 0.6 Ag 0.4 InCl 6 double perovskites with near-infrared emission. *Dalton Transactions* vol. 49 15231–15237 (2020).

153. Arfin, H., Kaur, J., Sheikh, T., Chakraborty, S. & Nag, A. Bi3+-Er3+ and Bi3+-Yb3+ Codoped Cs2AgInCl6 Double Perovskite Near-Infrared Emitters. *Angewandte Chemie - International Edition* vol. 59 11307–11311 (2020).

154. Gray, M. B., Majher, J. D., Strom, T. A. & Woodward, P. M. Broadband White Emission in Cs2AgIn1- xBixCl6 Phosphors. *Inorganic Chemistry* vol. 58 13403–13410 (2019).

155. Morrs, L. R. & Robinson, W. R. Crystal structure of Cs 2 NaBiCl 6. *Acta Crystallographica Section B* vol. 28 653–654 (1972).

156. Jiang, J. *et al.* Transformation between the Dark and Bright Self-Trapped Excitons in Lead-Free Double-Perovskite Cs 2 NaBiCl 6 under Pressure. *The Journal of Physical Chemistry Letters* vol. 12 7285–7292 (2021).

157. Zhang, L. *et al.* Tuning Emission and Electron-Phonon Coupling in Lead-Free Halide Double Perovskite Cs2AgBiCl6 under Pressure. *ACS Energy Letters* vol. 4 2975–2982 (2019).

158. https://www.hamamatsu.com/us/en/product/type/L9588/index.html. Accessed in 19/01/2022.

159. Makuła, P., Pacia, M. & Macyk, W. How To Correctly Determine the Band Gap Energy of Modified Semiconductor Photocatalysts Based on UV-Vis Spectra. *Journal of Physical Chemistry Letters* vol. 9 6814–6817 (2018).

160. S, S., K, A., Dzubinska, A., Reiffers, M. & R, N. Systematic investigations on the magnetic properties of moderate heavy Fermion CeAg0.68Si1.32 alloy. *Physica B: Condensed Matter* vol. 575 411679 (2019).

161. Norby, P., Dinnebier, R. & Fitch, A. N. Decomposition of Silver Carbonate; the Crystal Structure of Two High-Temperature Modifications of Ag 2 CO 3. *Inorganic Chemistry* vol. 41 3628–3637 (2002).

162. Siddique, H. *et al.* Anomalous Octahedron Distortion of Bi-Alloyed Cs2AgInCl6Crystal via XRD, Raman, Huang-Rhys Factor, and Photoluminescence. *Journal of Physical Chemistry Letters* vol. 11 9572–9578 (2020).

163. Miniscalco, W. J. Erbium-doped glasses for fiber amplifiers at 1500 nm. *Journal of Lightwave Technology* vol. 9 234–250 (1991).

164. Polman, A. Erbium as a probe of everything? *Physica B: Condensed Matter* vol. 300 78–90 (2001).

165. Liu, X., Yan, C. H. & Capobianco, J. A. Photon upconversion nanomaterials. *Chemical Society Reviews* vol. 44 1299–1301 (2015).

166. Wang, X., Yan, X. & Kan, C. Controlled synthesis and optical characterization of multifunctional ordered Y2O3 : Er3+ porous pyramid arrays. *Journal of Materials Chemistry* vol. 21 4251 (2011).

167. van Sark, W. G., de Wild, J., Rath, J. K., Meijerink, A. & Schropp, R. E. Upconversion in solar cells. *Nanoscale Research Letters* vol. 8 81 (2013).

168. Manzani, D., Petruci, J. F. da S., Nigoghossian, K., Cardoso, A. A. & Ribeiro, S. J. L. A portable luminescent thermometer based on green up-conversion emission of Er3+/Yb3+ co-doped tellurite glass. *Sci. Rep.* **7**, 41596 (2017).

169. Pugina, R. S. *et al.* Silk fibroin-Yb3+/Er3+:YAG composite films and their thermometric applications based on up-conversion luminescence. *Polymer (Guildf).* **241**, 124541 (2022).

170. Singh, A. K., Singh, S. K., Gupta, B. K., Prakash, R. & Rai, S. B. Probing a highly efficient dual mode: down–upconversion luminescence and temperature sensing performance of rare-earth oxide phosphors. *Dalt. Trans.* **42**, 1065–1072 (2013).

171. Caixeta, F. J. *et al.* High-Quantum-Yield Upconverting Er 3+ /Yb 3+ -Organic–Inorganic Hybrid Dual Coatings for Real-Time Temperature Sensing and Photothermal Conversion. *J. Phys. Chem. C* **124**, 19892–19903 (2020).

172. Borges, F. H. *et al.* Primary thermometers based on sol–gel upconverting Er3+/Yb3+ co-doped yttrium tantalates with high upconversion quantum yield and emission color tunability. *Journal of Sol-Gel Science and Technology* (2021) doi:10.1007/s10971-021-05673-0.

173. Dos Santos, L. F. *et al.* In vitro assays and nanothermometry studies of infrared-to-visible upconversion of nanocrystalline Er3+,Yb3+ co-doped Y2O3 nanoparticles for theranostic applications. *Physica B: Condensed Matter* vol. 624 413447 (2022).

174. Dong, B. *et al.* Optical thermometry through infrared excited green upconversion emissions in Er3+–Yb3+ codoped Al2O3. *Appl. Phys. Lett.* **90**, 181117 (2007).

Supplementary materials

Photocatalysis

Table S1. Crystallite size for Bi-based perovskite samples varying Ag/Na content utilizing three different peaks as references, (220), (400) and (422).

	Crystallite size (nm)			
Sample	**220**	**400**	**422**	**Arithmetic mean**
Ag1.0	65.47	51.36	44.26	53.70
Ag0.8	62.77	51.55	44.80	53.04
Ag0.6	36.64	25.87	22.50	28.34
Ag0.5	31.13	24.29	19.06	24.82
Ag0.4	43.97	39.85	25.40	36.41
Ag0.2	52.13	52.22	43.62	49.33
Ag0.0	65.54	68.71	48.51	60.92

The most intense peaks such as (220), (400) and (422) were used to calculate the crystallite size utilizing the Debey-Scherrer equation:

$$D_{hkl} = K\lambda/\beta\cos\theta \qquad \textbf{(S1)}$$

Where D is the crystallite diameter, hkl is the Miller indices of a certain plane, K is the numeric factor regarding crystallite shape factor, λ is the wavelength of the x-ray source utilized, in that case was used Cu source (1,518 Å), β is the full-width at half-maximum of a certain X-ray diffraction peak and θ is the Bragg angle. It is noticed that the crystallite size of Bi-based samples is different from each other, following no size logic just being possible to observe that samples located at the extremes, like Ag1.0; Ag0.8 and Ag0.0 possess the bigger crystallite size. Crystallite median size for these samples variated from 24.82 nm to 60.92 nm, with the "middle mixed" samples exhibiting the lowest crystallite size values. This crystallite size following no logic may be a consequence of XRD equipment deconfiguration.

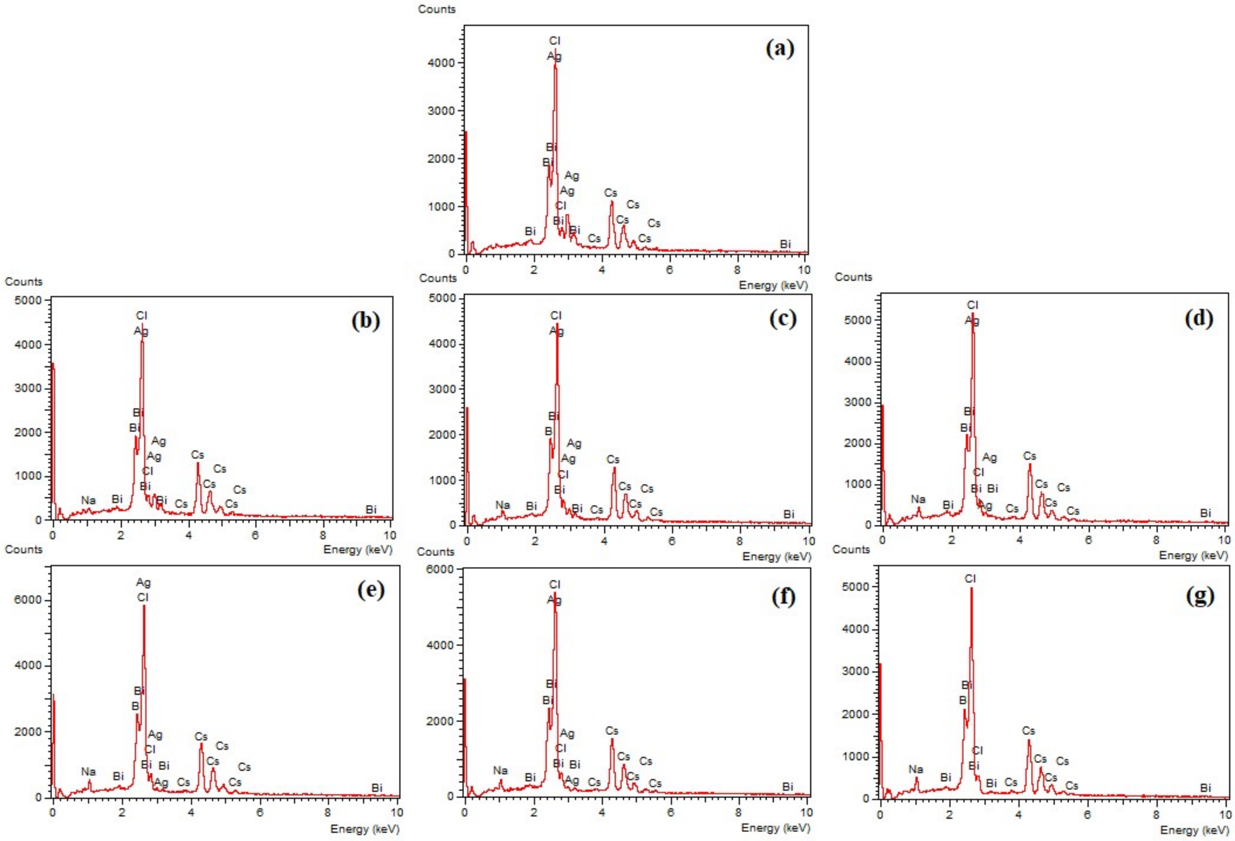

Figure S1. Energy dispersive X-ray spectroscopy (EDS) for Ag1.0 (a); Ag0.8 (b); Ag0.6 (c); Ag0.5 (d); Ag0.4 (e); Ag0.2 (f); and Ag0.0 (g) sample

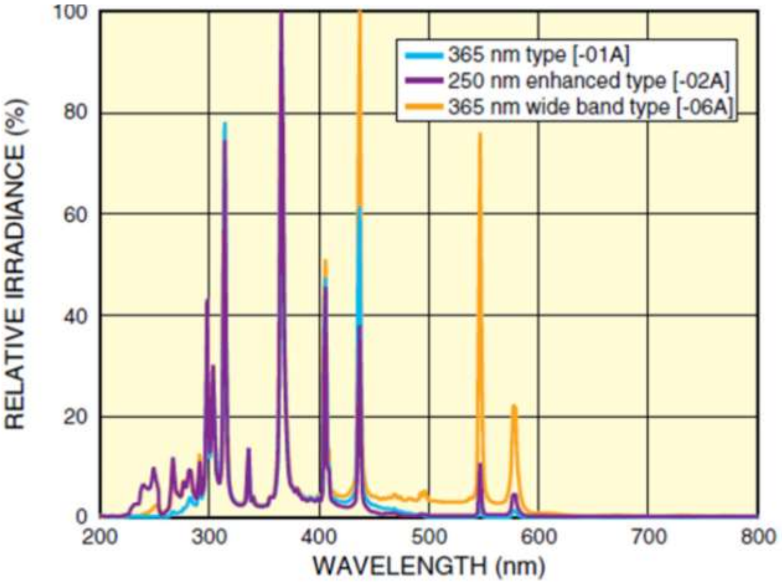

Figure S2. Light emission spectra of the used Xe arc lamp from 200 to 800 nm.[155]

Ln^{3+}-doped perovskites: Photoluminescence

Table S2. Crystallite size in nanometers for In-based perovskites utilizing the peaks (220), (400), and (422).

	Crystallite size (nm)			
Sample	**220**	**400**	**422**	**Arithmetic mean**
pIn	**80.14**	**111.45**	**93.52**	**95.04**
pIn0.9	**43.17**	**40.54**	**33.80**	**39.17**
pAg0.6In	**45.60**	**39.12**	**34.50**	**39.74**
pAg0.6In0.9	**40.84**	**37.73**	**36.06**	**38.21**

Crystallite size for In-based perovskite samples were calculated using equation S1.

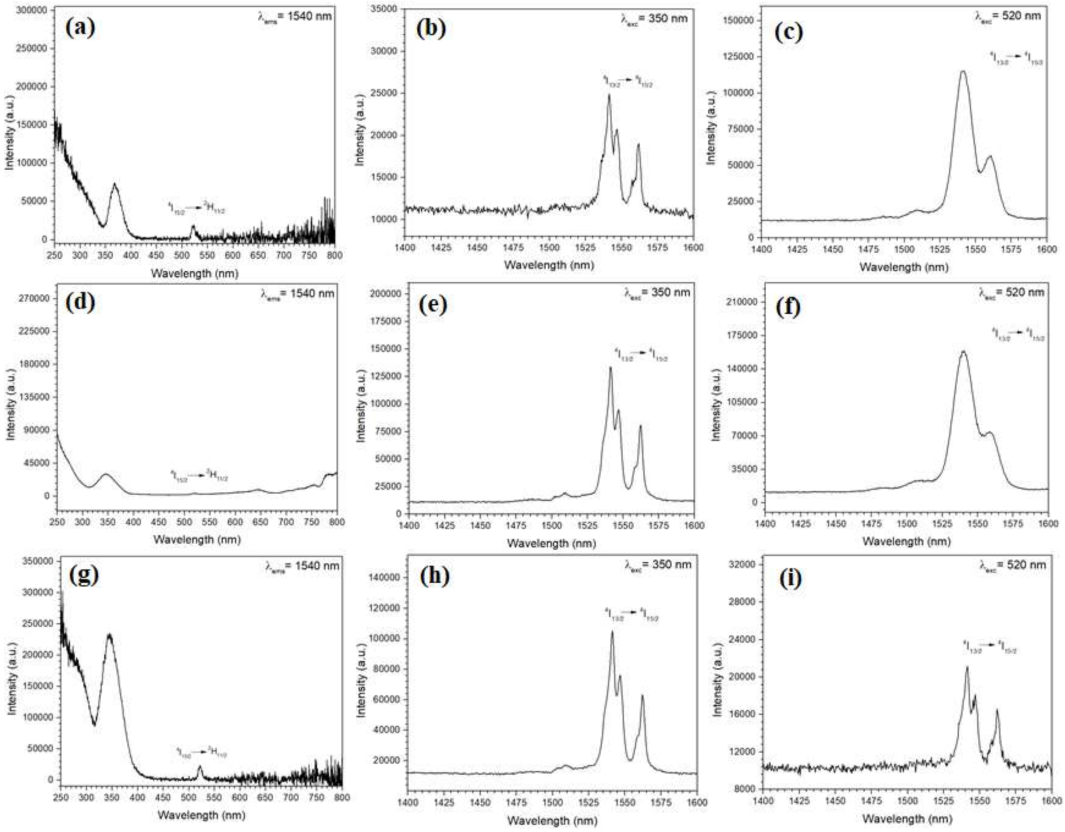

Figure S3. Emission and Excitation spectra for Er^{3+} samples 5%. pIn0.9 excitation spectra at 1540 nm (a), and emission spectra at 350 (b) and 520 nm (c); pAg.06In excitation spectra at 1540 nm (d), and emission spectra at 350 (b) and 520 nm (c); pAg0.6In0.9 excitation spectra at 1540 nm (g), and emission spectra at 350 (b) and 520 nm (c).

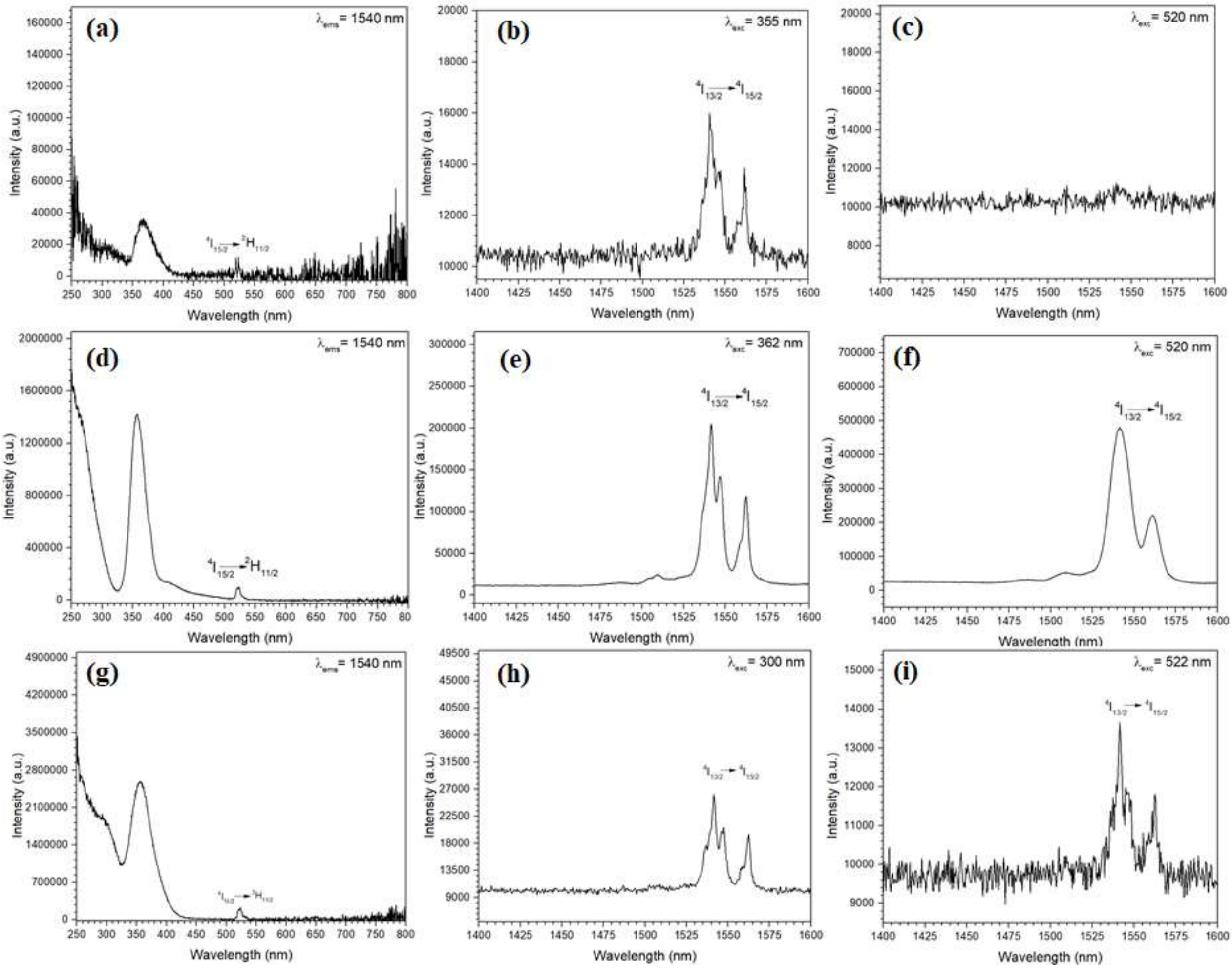

Figure S4. Emission and Excitation spectra for Er^{3+} samples 15%. pIn0.9 excitation spectra at 1540 nm (a), and emission spectra at 355 (b) and 520 nm (c); pAg.06In excitation spectra at 1540 nm (d), and emission spectra at 362 (b) and 520 nm (c); pAg0.6In0.9 excitation spectra at 1540 nm (g), and emission spectra at 300 (b) and 522 nm (c).

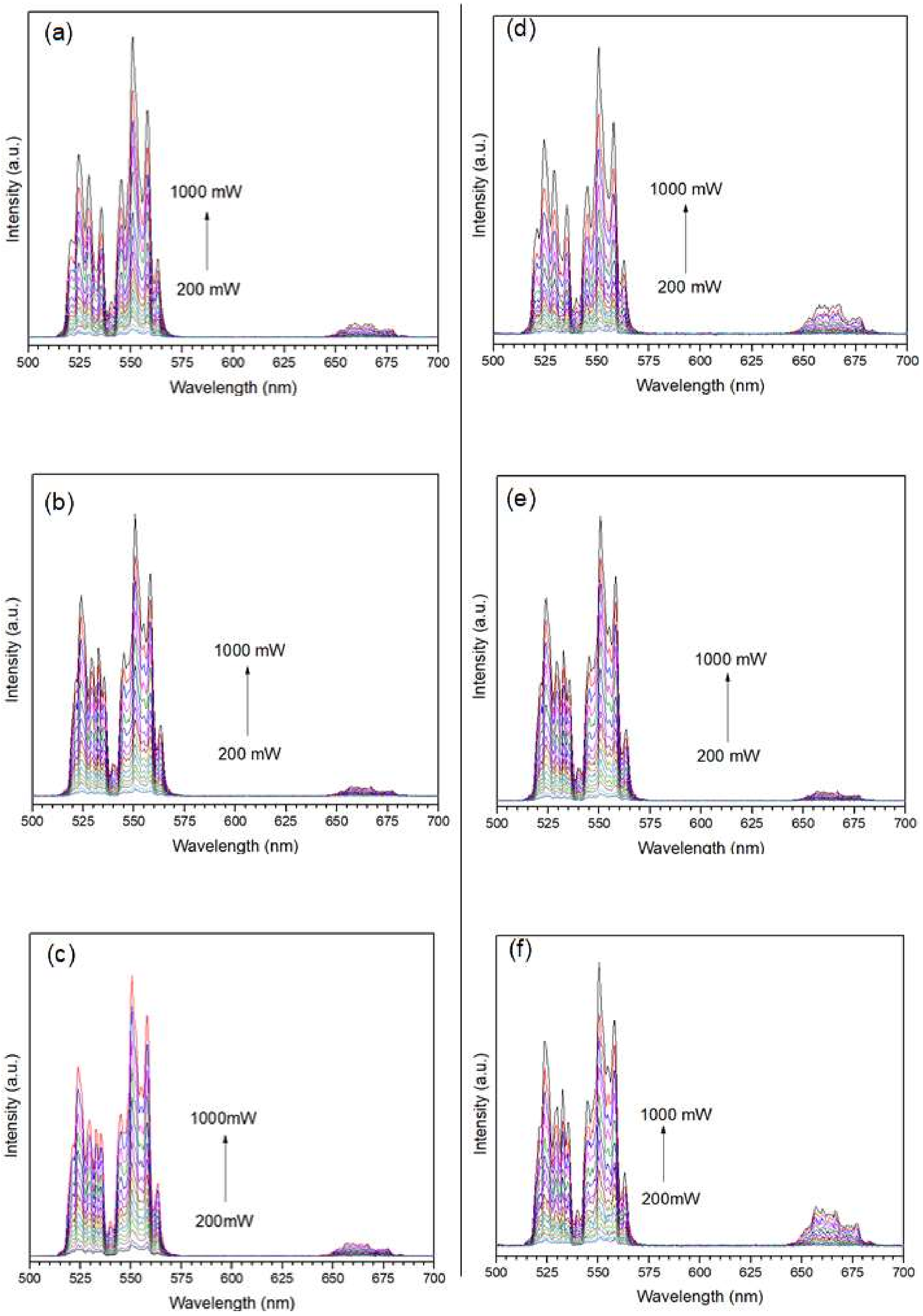

Figure S5. Emission of In-based perovskite doped with 5 and 15 % of Er using a 980 nm laser going from 1000 mW to 200 mw. Er^{3+} (5%) doped pIn0.9 (a), pAg0.6In (b) and pAg0.6In0.9 (c). Er^{3+} (15%) doped pIn0.9 (d), pAg0.6In (e) and pAg0.6In0.9 (f).